Quantum Acoustics with Multimode Surface Acoustic Wave Cavities

by

Lucas R. Sletten

B.A., St. Olaf College, 2015

M.S., University of Colorado, 2018

A thesis submitted to the

Faculty of the Graduate School of the

University of Colorado in partial fulfillment

of the requirements for the degree of

Doctor of Philosophy

Department of Physics

2021

Committee Members:

Konrad W. Lehnert, Chair

John Teufel

James Thompson

Murray Holland

Zoya Popovic

Sletten, Lucas R. (Ph.D., Physics)

Quantum Acoustics with Multimode Surface Acoustic Wave Cavities

Thesis directed by Prof. Konrad W. Lehnert

Control over the quantum state of macroscopic mechanical oscillators promises advances in the understanding of fundamental physics as well as the development of new quantum technologies. Surface acoustic waves are an attractive mechanical system in a quantum context as they can be designed to interact with many popular quantum platforms, including superconducting qubits. Moreover, surface acoustic waves are already a mature commercial technology widely used in classical signal processing where the slow speed of sound (km/s) means structures with long delays and therefore fine frequency features can be engineered in chip-scale geometries.

In this thesis, I will describe how quantum acoustics with surface acoustic waves coupled to superconducting qubits can leverage these long delays to build cavities with high densities of resonant modes and qubit-phonon interactions precisely tailored in the frequency domain to suit experimental demands. I first demonstrate resonant interaction between a transmon qubit and a multi-mode surface acoustic wave resonator where the qubit-resonator coupling strength exceeds not only the decay rates of the qubit and resonator but also the spacing between resonant modes of the cavity. As a natural extension of this result, I describe how intentional shaping of the qubit-cavity coupler in real space leads to a desirable frequency-dependent interaction strength. This hybrid system can achieve interaction strengths large enough for the single-phonon Stark shift to exceed the relevant dissipation rates, leading to the resolution of phonon number states in the qubit spectrum. I will conclude by evaluating the prospects for improved qubit and acoustic performance that would enable a host of experiments, in particular showing that the dominant acoustic loss mechanism, phonon diffraction, can be eliminated by implementing focusing acoustic cavities.

Acknowledgements

The work contained in my thesis was not performed in a vacuum. I have been truly fortunate to have had help from many amazing people. Their broad expertise, thoughtful guidance, and ready assistance made my research possible and my time in Boulder so enjoyable.

First, thanks are in order for my committee members John Teufel, James Thompson, Murray Holland, and Zoya Popivic, for giving me their valuable time and invaluable feedback, and also for agreeing to another multi-hour Zoom meeting. I sincerely hope my defense is the last one they have to do remotely. I would like to thank Zoya in particular, as she taught me and a substantial contingent of Lehnert lab members the fundamentals of microwave engineering that underlies so much of the work in this thesis.

This thesis involved a significant amount of microfabrication, and so I would like to thank the Keck lab staff, Dave Alchenburger and Mark Carter, and the more extensive BMF staff, for their patience and expertise. Travis Autrey deserves special thanks for helping me develop my process and learn the tools in the BMF cleanroom and for the fruitful discussions about focusing SAW cavities.

I also want to thank everyone in the Lehnert group. The lab dynamic was always friendly and collaborative, filled with lively conversations about technical difficulties, exciting results, and the occasional JILA cup adventure. I need to thank Adam Reed for his training during my first year, showing me first-hand how to measure quantum systems, run a dilution refrigerator, and how to be a successful graduate student. I owe a special thanks to Brad Moores, who was right by my side through the core of my PhD and whose work and ideas pervade this thesis. I also must thank

Jeremie Viennot for his contagious and effective mix of keen skepticism, scientific enthusiasm, and high tolerance for questions. Lastly, I want to thank Brendon Rose for helping push me across the finish line and who, along with Alec Emser and Pablo Aramburu-Sanchez, have brought fresh ideas and energy to the project that will without a doubt take them to many exciting places.

Of course, I owe a great deal to Konrad. He has been an excellent advisor, providing countless insights and priceless guidance. In particular, he has a practiced knack for transcribing his deep knowledge base into concise models, which he so clearly enjoys sharing (and re-sharing), and that will forever shape my view of the world.

Finally, my family deserves the biggest thanks of all. Ellyn is simply the best, and I wouldn't have been able to make it here without her support, particularly in this last year when the world changed so drastically. My parents and brother and sister are wonderful people who have shaped me into who I am and supported my psychological well-being through their continual love and encouragement.

I am sure this list is incomplete and inadequate, but to everyone who has helped me along the way: thank you so much!

Contents

Chapter

Tables

Table

Figures

Figure

Chapter 1

Introduction

Modern science, having mastered the strange rules of quantum mechanics that govern our world, has endeavored to engineer increasingly complicated quantum systems to achieve specific tasks [1]. The impressive early successes of these efforts combined with the transformative potential of quantum technologies, particularly in efficient processing of information, has begun to generate substantial scientific and even commercial interest. A diverse array of physical platforms is under development, from individual trapped atoms to superconducting electrical circuits. Each platform possesses unique advantages and produces their own lessons, each strengthening the wider enterprise. In this thesis, I will describe research into the quantum behavior of mechanical oscillators in the form of surface acoustic waves (SAWs). I will describe my work developing SAW systems in a quantum context, with a focus on what applications these mechanical systems could find in developing quantum technologies as well as what general lessons can be learned from this particular platform.

Long before the development of quantum mechanics, mechanical oscillators were at the forefront of revolutionary technologies and scientific understanding. These systems can be described with simple models, designed to meet a wide range of specifications, and measured with great precision. For example, pendulum clocks revolutionized the keeping of time, and their widespread adoption in the mid-1700's brought about the high degree of human coordination required to begin the Industrial Revolution [2]. Foucalt, a French scientist in the mid-1800's, used a simple extension of these pendulum clocks to prove Earth's rotation in a concise and widely disseminated exper-

iment. Torsional oscillators, where the gravitation restoring force is replaced with the generally weaker force provided by the twisting of a wire, can be used as incredibly sensitive sensitive force sensors. By measuring the attractive force between two known masses, this type of oscillator was used to make the first measurements of Newton's gravitational constant [3], as well as the most precise measurement to date [4], two experiments spanning over 200 years and 4 orders of magnitude in precision.

In the last century, the ascent of microelectronics led to a new class of commercial applications for mechanical systems. Several transduction strategies exist to integrate mechanical components with electronics. Through such integration, motion can be precisely driven and recorded. The most direct method of transduction is using the piezoelectric effect, where the stress in a material is directly coupled to its electric polarization, but a range of other methods exist each specialized for various applications. The scope and prevalence of technologies based on electro-mechanical systems is hard to overstate, with applications ranging from the microphones and speakers present in all cell phones to sonar and medical ultrasound technology that produce images of objects using reflections of high frequency (> 1 kHz) acoustic waves. Acoustic excitations in piezoelectric materials themselves are widely used in commercial technologies. Waves in the bulk of piezoelectric materials can be confined to form mechanical oscillators whose resonant frequency can be measured with great precision. The most popular modern timepieces, used widely in wrist watches and computers, operate by counting the oscillations of a quartz tuning fork. Similar quartz resonators are used to make micro-balances that are sensitive enough to detect a single additional layer of metal adhered to its surface [5].

Elastic materials support a special type of wave that is strongly confined to the surface. These waves, known either as known as Rayleigh waves [6] or more generally as surface acoustic waves, interact strongly with the surface topography, and, on a piezoelectric material, the details of the conversion between acoustic waves and electrical signals depend directly on the geometry of the transducer, an effect discussed further in Ch. 2. Moreover, the slow speed of sound (km/s) compared to light means acoustic wavelengths are short compared to typical devices (mm) even at

RF frequencies. Thus, devices built using piezoelectric Rayleigh waves can realize a wide range in behavior by leveraging modern lithographic techniques to generate complicated transducer geometries and surface topographies with great detail and precision. Crucially, devices can be designed with length scales spanning sub-wavelength to hundreds of wavelengths long at RF frequencies, resulting in fine control over the realized frequency response. SAW devices are a mature commercial technology, used widely as oscillators, sensors, and filters, but particularly in applications where large delays and specific dispersion responses are required, such as pulse compression filters in radar and band-pass filters in telecommunications [7]. As discussed later in this chapter, these same attributes make SAWs attractive candidates for use in future quantum technologies.

The fundamental excitations of mechanical systems, termed phonons, were known to behave according to quantum mechanics since the early 1900's. The measurements of heat capacity of solids at low temperatures, shown to follow a T^3 temperature dependence, were well explained by Debye [8]. In his model, mechanical excitations in the solid are described by a collection of independent quantum harmonic oscillators, each representing a normal mode of the solid with frequency ω, with a high frequency cut-off corresponding to when the wavelength is twice the atomic lattice spacing. As a material approaches zero temperature, more modes are cooled to their quantum ground state, as their energy per excitation exceeds the available thermal energy $k_B T$, and no longer contribute to the materials specific heat, thus providing evidence that mechanical excitations are indeed quantized.

Continued use of mechanical systems at the forefront of scientific discovery created deeper interest in the quantum behavior of motion, particularly into the interaction between motion and light. The now successful efforts by LIGO to measure gravitational waves using a Michelson interferometer first drew attention to the quantum behavior of motion and its potential technological relevance [9]. While LIGO is predominantly an optical measurement, its sensitivity depends directly on the motion of the mirrors that form the optical interferometer. To detect the strain generated by a passing gravitational wave from an interstellar signal of interest, which is of order 10^{-23}, the mirrors must be separated by a large distance (km), but also held exceptionally still and

then measured with incredible precision (am).

Reaching these unprecedented levels of precision required to observe gravitational waves raised concerns about the role of quantum effects. In the 1980's, researchers concluded that quantum mechanics does place a limit on the ability to measure the position of a mechanical oscillator using coherent laser light [10, 11]. Increasing the power in the light field increases the resolution of the measurement, but the increased flux of photons also acts as a stochastic drive on the oscillator through radiation pressure, an effect termed "measurement backaction." Eventually, increasing the power leads to an increased position uncertainty as the radiation pressure drives position fluctuations of the mirrors that exceed the measurement resolution. LIGO employs enormous powers (100 kW) to achieve the necessary strain resolution, and at these powers measurement backaction, an effect of the quantum nature of mechanical motion, constitutes a significant limit on LIGO's sensitivity [12]. Already, the experiment has incorporated a non-classical light source where the quantum fluctuations are redistributed in phase space, called squeezed light, with a demonstrable increase in sensitivity [13].

The interest in the quantum behavior of macroscopic mechanical systems, first investigated in the context of gravitational waves, has since garnered broad scientific interest. The quantized collective excitations of mechanical systems have a range of properties that makes them attractive for fundamental science and advancing quantum technologies. For one, how quantum decoherence of mechanical oscillators might result from gravitational interactions, a question at the intersection of the famously incompatible theories of general relativity and quantum mechanics, could be investigated by preparing a massive phononic system in a sensitive quantum state and monitoring its decay [14]. Mechanical systems experience many forces besides gravity, and their performance as general sensors could be improved using quantum enhanced metrology [15]. The wide range of quantum platforms that can interact with motion makes mechanical systems promising intermediary elements in quantum transduction schemes [16, 17, 18]. And, as mechanical energy cannot radiate into free space, vibrational modes can be engineered to have high quality factors [19, 20], making them attractive for storing and processing information [21, 22]. Additionally, potential

quantum technologies built around phonons would benefit from the simple fact that sound travels significantly slower than light. The slowness of sound is widely used by surface acoustic wave devices to construct delay lines and other filtering devices. Long delays can be used to create multi-mode acoustic resonators [23] that hold potential for processing quantum information but in a small fraction of the space required using electromagnetic excitations [24]. These multi-mode resonators have potential for serving as registries in a quantum random access memory [25, 26, 27], a promising architecture for quantum information processing and a main motivating goal in this thesis.

In the last decades, experimental efforts have made great strides towards control of mechanical oscillators at the quantum level. One of the first obstacles towards quantum control is the large thermal occupancy of mechanical oscillators at accessible temperatures. Mechanical oscillators typically have resonant frequencies below 100 MHz, so even dilution refrigerators with base temperatures of 20 mK correspond to a significant number of thermal excitations. However, through radiation pressure interactions with either microwave or optical fields linearized around around a strong pump, phonons can be swapped with higher frequency photons. This swapping interaction results in a mechanical occupancy near that of the electromagnetic resonator, which corresponds to an effective temperature well below the thermal environment. Cooling to the quantum ground state, where less than one thermal phonon is present on average, was achieved for a range of mechanical oscillators in the last decade [28, 29, 30]. Beyond cooling, experiments were able to prepare mechanical squeezed states [31, 32] as well as entangle the state of the mechanical resonator with propagating photons [33, 34] and other stationary oscillators [35]. Impressively, LIGO has recently reported that they can cool the motion of a 10 kg mirror from room temperature to an average occupancy of 10.8 phonons, corresponding to an effective temperature of 77 nK [36].

Despite successes in cooling and controlling mechanical motion, schemes built on linearized radiation pressure interactions have struggled to create non-classical states of motion. The linear nature of the effective interaction means input Gaussian states must transform to output states that are also Gaussian. Some success has been achieved by either using a non-classical input state

[22] or by deploying a non-linear measurement, such as photon counting [34, 37]. A more general approach is to replace the electrical or optical cavity with an non-linear element.

For example, the fundamentally non-linear internal electronic states of atomic ions confined in an electromagnetic trap can be coupled to their harmonic motion [38]. The interaction between harmonic motion and the non-linear, atomic degree of freedom is realized using precisely tuned pulses of laser light. These trapped ion systems successfully generated an array of non-classical states of the ions motion, including number states, squeezed states, and so-called Schrodinger cat states [39, 40]. More recently, superpositions of vastly different Fock states have been created [41]. These superposition states are of great interest to quantum metrology as they reach the maximum sensitivity for a given number of excitations. While potentially useful as force sensors, ion motion is quite distinct from the acoustic technology widely employed in classical information processing.

Another powerful example of quantum control using direct coupling to a non-linear element can be drawn from the the maturing field of circuit quantum electrodynamics (cQED) [42, 43, 44]. In cQED, microwave frequency electromagnetic cavities interact strongly with superconducting qubits, quantum systems formed by the collective electronic excitations of microwave circuits with a non-linearity provided by Josephson junctions. The state of the qubit can be determined through its interaction with the electromagnetic cavity [45]. Conversely, using the qubit for control and readout, nearly arbitrary quantum states can be created and measured in the inherently linear electromagnetic cavities [46, 47, 48, 49]. The long lifetimes and large Hilbert space of these electromagnetic resonators has generated significant interest in their usefulness as quantum registers [50, 51, 52, 53].

The value of cQED in efforts to control the quantum state of a mechanical oscillator extends beyond being a useful example. In contrast to the internal states of atomic qubits, the non-linearities in superconducting qubits can be coupled directly to common types of mechanical excitations through a variety of methods, many with direct analogies to how microelectronics are integrated with mechanical systems in commercial settings. In a seminal work, a thin film bulk acoustic wave resonator was coupled to a superconducting phase qubit through piezoelectricity such that the two

system exchanged excitations in about 4 ns when tuned on resonance [54]. Dilution refrigerator temperatures were sufficient to cool the high frequency mechanical mode, with a resonance just below 6 GHz, to its quantum ground state. By swapping excitations with the phase qubit, ground state cooling of the motion could be directly verified. Moreover, a single excitation in the phase qubit could be swapped into the mechanical oscillator, placing the macroscopic oscillator in a single phonon number state. Although limited by poor coherence times of below 10 ns, this impressive result was the first demonstrations of basic quantum control of a macroscopic mechanical oscillator.

Building on this result, piezoelectric Rayleigh waves are a particularly rich system to consider in a quantum context. To a significant degree, surface acoustic waves are a slow analog of light in two dimensions. This analogy makes many physical models developed for trapped atoms in optical cavities or superconducting qubits coupled to microwave light readily applicable to the acoustic case. However, departures from this analogy lead to many potential unique applications for SAWs. For one, SAWs are able to transduce information between various platforms of quantum information processing technologies [55, 56, 57, 58]. Additionally, the interaction between surface acoustic waves and superconducting qubits can be modelled on commercial SAW transducers, and the many-wavelength extent of these coupling elements differs greatly from the standard dipole coupling in circuit and cavity QED. This spatially extended interaction gives fine frequency-domain control over the qubit-phonon interaction [59]. Furthermore, acoustic resonators take up a small fraction of the volume of their electromagnetic counterparts, allowing them to reach deeper into multi-mode regimes while occupying less fridge space. Reflectors for SAWs are narrow-band, and thus these devices naturally have simultaneous access to both cavity and waveguide QED physics [60, 61, 62]. Finally, initial work has already demonstrated that propagating SAW phonons can be successfully coupled to a superconducting transmon qubit [63].

The work in this thesis investigates the prospects for surface acoustic waves as a platform for future quantum technologies, focusing in particular on the potential of multi-mode acoustic cavities in processing information in a hardware efficient manner [26]. I present results demonstrating strong coupling between a superconducting qubit and a multi-mode SAW resonator, highlighting the high

density of modes available in acoustic platforms [64]. Then, I show that by tailoring the qubit-phonon interaction, the Stark shift of individual phonons can be resolved in the spectrum of a superconducting qubit [65]. This ability to count phonons demonstrates their quantum nature and is a key milestone towards simultaneous quantum control over an array of surface acoustic wave resonances [46]. Furthermore, the strategy described is extendable to massively multimode cavities with high densities of strongly coupled resonant modes. I conclude with a proposed experiment to entangle multiple modes of a SAW cavity through joint, projective measurement. Progress towards several improvements are described that would make this experiment possible, including the demonstration of coherent, focusing SAW resonators.

Concurrent with the research performed with this thesis, the field of quantum acoustics grew rapidly. High overtones of a bulk acoustic wave (BAW) resonator were strongly coupled to a transmon qubit [66], and multi-phonon Fock states were created and measured through resonant exchange with the qubit [67]. These BAW resonators can also be interfaced with optical light [68], suggesting a path to microwave to optical conversion. For SAWs, an initial demonstration of dispersive interactions between a superconducting qubit and a radio-frequency resonator [69] was quickly followed by demonstrations of quantum control of SAW excitations [70]. Further work simulated distant entanglement of two superconducting qubits using the long travel time of SAW wave packets [71], as well as a phononic quantum erasure where two-phonon interference disappears when their which-path information is measured [72]. A one dimensional beam was coupled strongly to a superconducting qubit using a piezoelectric thin film, and the qubit spectrum showed the discrete quantized excitations of the beam [73]. While not exactly quantum acoustics, incorporating superconducting non-linearities into a radiation-pressure type devices described earlier enabled number-sensitive electro-mechanics [74] and the preparation of sub-Poissonian states of motion [75].

The structure of the thesis is as follows: an introduction to surface acoustic wave resonators is given in Ch. 2, followed by their quantum description and an introduction to superconducting qubits in Ch. 3. Experimental results demonstrating strong, multi-mode coupling are presented

in Ch. 4 and phonon number splitting are given in Ch. 5. Finally, work towards improved device performance by moving to lower frequencies and implementing focusing cavities is summarized in Ch. 6 before conclusions and an outlook are presented in Ch. 7.

Chapter 2

Surface Acoustic Wave Resonators

Surface acoustic waves (SAWs) are a type of elastic wave that is confined to the surface of a material. These waves come in many varieties, the simplest and the type used in this thesis are named after Lord Rayleigh who discovered their existence in 1885 [6]. Surface acoustic waves became technologically relevant in the mid 1960's with the invention of the interdigitated transducer (IDT) [76], a structure capable of efficiently converting signals between the electronic and acoustic domain through the piezoelectric effect. Importantly, this transducer is formed from a patterned thin metallic film and as such is compatible with modern lithographic techniques, enabling the production of SAW devices at scale. Such devices have become widely used for filtering; the filter performance is determined by the transducer geometry, which can be controlled with high precision [7]. Crucial to their commercial success is the slow speed of sound that can be used to generate long delays in a compact geometry. These long delays can also be used to create multi-mode cavities with potential uses in quantum information processing, as the density of resonant modes is proportional to the cavity round trip time. The following chapter introduces the Rayleigh wave solution, describes the components required to construct SAW cavities and the techniques to design their performance, and concludes with presenting a useful model for describing multi-mode resonators.

2.1 Elastic Waves in a Solid

An analytical description of Rayleigh waves is important to understanding the devices discussed in this thesis and the nature of their limitations. First, I will derive Rayleigh wave solutions in an isotropic medium, as this derivation shows the underlying physics and produces the general wave behavior without introducing the full complexity of piezoelectric, anisotropic media. The following derivation is drawn from [7].

2.1.1 Stress and Strain

Acoustic waves in a solid are described by two vector quantities: stress and strain. Strain characterizes the internal displacement **u** of constituent 'particles' of from their equilibrium position,

$$S_{ij}(x_1, x_2, x_3) = \frac{1}{2}\left(\frac{\partial u_i}{\partial dx_j} + \frac{\partial u_j}{\partial dx_i}\right). \tag{2.1}$$

Stress T_{ij}, on the other hand, characterizes the internal forces in a material. The force in the ith direction per unit area on a plane with normal **n** is,

$$f_i = \sum_j T_{ij} n_j. \tag{2.2}$$

For sufficiently small amplitudes, stress and strain are related by the stiffness tensor, c_{ijkl},

$$T_{ij} = \sum_k \sum_l c_{ijkl} S_{kl}. \tag{2.3}$$

This relationship is Hooke's law generalized to a three dimensional solid. While this relationship is simple, the generalization comes with a significant amount of added complexity: even incorporating symmetry and thermodynamic constraints, there are 21 independent elements in this stiffness tensor. Particular material symmetries can further reduce the number of elements. For example, cubic crystals are described by 3 independent elements, while isotropic materials are described by just 2 [7].

The dynamics of the system are determined by considering Newton's second law. In a material with density ρ, an infinitesimal cube of length δ has mass $\rho\delta^3$. In the presence of non-zero stress,

the cube will experience a net force proportional to the area per side and the change in stress across the cube. Newton's second law then gives the equation of motion,

$$\rho \frac{\partial^2 u_i}{\partial t^2} = \sum_j \frac{\partial T_{ij}}{\partial x_j}. \tag{2.4}$$

Combined with 2.1, this equation relates acceleration to curvature and is a familiar wave equation, albeit in a complicated three dimensional space.

2.1.2 Transverse and Shear Waves

In a general isotropic medium, symmetry simplifies the stiffness tensor c_{ijkl} to only two independent constants. The stiffness tensor takes the form,

$$c_{ijkl} = \lambda \delta_{ij} \delta_{kl} + \mu(\delta_{ik}\delta_{jl} + \delta_{il}\delta_{jk}), \tag{2.5}$$

where μ and λ are known as Lamé constants and δ_{ij} is the Kronecker delta. This simplified stiffness tensor yields stresses,

$$T_{ij} = \lambda \delta_{ij} \Delta + 2\mu S_{ij}, \tag{2.6}$$

where $\Delta = \sum_i \frac{\partial u_i}{\partial x_i}$. The equation of motion is,

$$\rho \frac{\partial^2 u_j}{\partial t^2} = (\lambda + \mu) \frac{\partial \Delta}{\partial x_j} + \mu \nabla^2 u_j. \tag{2.7}$$

This equation supports two types of waves in an infinite medium. To see this, consider a plane wave solution with frequency ω and wavevector $\mathbf{k}$,

$$\mathbf{u} = \mathbf{u_0} \exp[\mathbf{j}(\omega \mathbf{t} - \mathbf{k} \cdot \mathbf{x})], \tag{2.8}$$

where $\mathbf{u_0}$ is a constant amplitude vector. Substituting this wave into equation 2.7 gives,

$$\omega^2 \rho \mathbf{u_0} = (\lambda + \mu)(\mathbf{k} \cdot \mathbf{u_0})\mathbf{k} + \mu |\mathbf{k}|^{\mathbf{2}} \mathbf{u_0}. \tag{2.9}$$

There are three vector quantities in this equation, and two of them point along $\mathbf{u_0}$. To have non-trivial solutions, there are two possibilities: either $\mathbf{k} \cdot \mathbf{u_0}$ is zero and thus $\mathbf{k}$ is perpendicular to $\mathbf{u_0}$, or that $\mathbf{k}$ is parallel to $\mathbf{u_0}$ and all the terms have the same direction.

In the first case, when $\mathbf{k}\cdot\mathbf{u_0} = \mathbf{0}$, the waves are transverse or shear waves. From equation 2.7, these shear waves have wavevector $\mathbf{k_t}$ given by,

$$|\mathbf{k_t}|^\mathbf{2} = \omega^\mathbf{2}\rho/\mu, \tag{2.10}$$

and are dispersionless with velocity $V_t = \sqrt{\mu/\rho}$.

In the second case, with the wave-vector $\mathbf{k}$ parallel to the displacement $\mathbf{u_0}$, the waves are longitudinal in character. Similarly to the transverse case, equation 2.7 means that these longitudinal waves have wavevector $\mathbf{k_l}$ given by,

$$|\mathbf{k_l}|^\mathbf{2} = \omega^\mathbf{2}\rho/(\lambda + \mathbf{2}\mu), \tag{2.11}$$

and velocity $V_l = \sqrt{(\lambda + 2\mu)/\rho}$. Note that since the Lamé constants μ and λ are always positive, longitudinal waves always have a faster speed of sound than transverse waves.

2.1.3 Rayleigh Waves

To find Rayleigh waves solutions, a surface must be considered. Without loss of generality, assume the isotropic medium occupies only the space below the plane at $x_3 = 0$ with vacuum for all $x_3 > 0$. Here, I will derive a Rayleigh wave propagating in the x_1 direction with no variation in the x_2 direction, satisfying both the equation of motion [Eq. 2.7] as well as the boundary condition that there are not any forces on the free surface at $x_3 = 0$.

The heart of the surface wave solution found by Rayleigh is to add together a longitudinal and a shear wave. By symmetry of the isotropic material, these two partial waves must have displacements only in the plane spanned by the direction of propagation and the surface normal, known as the sagittal plane, so their wavevectors have just two components: one in the direction of propagation x_1 and the other into the surface x_3. The two waves must have the same wavevector β in the direction of propagation x_1. This fixes the x_3 components of the wavevectors to be,

$$T^2 = \omega^2/V_t^2 - \beta^2, \quad L^2 = \omega^2/V_l^2 - \beta^2, \tag{2.12}$$

where T is the x_3 component of the transverse wavevector and L is the x_3 component of the longitudinal wavevector. For the waves to be confined to the surface, they must be evanescent in the $-x_3$ direction, and so both L and T must be positive and imaginary.

The unit vector of the waves displacement for both shear and longitudinal cases can be determined by using that longitudinal waves have $\mathbf{u_l}$ is parallel to $\mathbf{k}$, while for transverse waves they are perpendicular. Thus,

$$\mathbf{u_l} = (1, 0, L/\beta)A \exp[-j(\beta x_1 + L x_3)], \tag{2.13}$$

$$\mathbf{u_t} = (1, 0, -\beta/T)B \exp[-j(\beta x_1 + T x_3)], \tag{2.14}$$

where A and B are constants. These solutions are no longer strictly plane waves, but are still valid solutions satisfying the equations of motion and are bounded in the given half-space.

The remaining constants and wavevectors can be determined by applying the boundary conditions. The free surface condition, i.e. $T_{13} = T_{23} = T_{33} = 0$, can be applied to equation 2.6 and the partial wave solutions above to give a pair of linear relations between the values of A and B. For there to be a non-trivial solution, the determinant of the relations must be zero,

$$(T^2 - \beta)^2 + 4\beta^2 L = 0. \tag{2.15}$$

This equation then gives the relationship between the Rayleigh velocity V_R and the transverse and longitudinal phase velocities,

$$(2 - V_R^2/V_t^2)^2 = 4\sqrt{(1 - V_R^2/V_t^2)(1 - V_R^2/V_l^2)}. \tag{2.16}$$

This equation has only one solution, thereby determining V_R. The Rayleigh velocity is near but slightly below the transverse velocity, with the ratio V_R/V_t set by the ratio V_l/V_t.

Once V_R is known, the displacements can be found for the full Rayleigh wave,

$$u_1 = [\gamma \exp(a\beta x_3) - \exp(b\beta x_3)] \exp[j(\omega t - \beta x_1)], \tag{2.17}$$

$$u_3 = j[\gamma a \exp(a\beta x_3) - b^{-1} \exp(b\beta x_3)] \exp[j(\omega t - \beta x_1)], \tag{2.18}$$

where $a = -jL/\beta, b = -jT/\beta$ and $\gamma = (2 - V_R^2/V_t^2)/(2ab)$ are all positive and real. The displacements for the Rayeleigh solution on fused quartz ($V_l = 5968$ m/s, $V_t = 3764$ m/s, $V_R = 3409$ m/s) are shown in 2.1. The relative phase between u_1 and u_3 means that the motion of each particle is elliptical. The decay into the substrate has two terms; a slow term from the shear partial wave, which has a velocity closer to that of the Rayleigh wave, and a fast term from the longitudinal partial wave. Interestingly, the two decaying terms have opposing sign, and this can result in a change of sign of the displacement in the bulk compared to the surface.

Rayleigh waves can essentially be treated as one dimensional phenomena as they are invariant in the x_2 direction and strongly confined in the x_3 direction. The majority of this thesis uses a quasi-1D description, despite the reality that any device will have a finite extent in the transverse direction. Phenomena outside this assumption almost always require only a 2D description. For example, the diffraction of acoustic waves requires considering SAWs only in the plane of the surface, while scattering of waves from surface perturbations into the bulk of the material requires considering only waves in the sagittal plane.

2.1.4 Incorporating Anisotropy and Piezoelectricity

Surface acoustic waves are more relevant to technology when the medium is piezoelectric. The coupling of stress and electric field mean that acoustic waves can be transduced to electromagnetic ones, enabling a wide range of commercial and quantum applications. However, piezoelectricity requires a breaking of inversion symmetry, and considering this anisotropy greatly complicates the analysis.

In a piezoelectric material, the internal stresses are not only due to strain but also electric field. In the regime where this effect can be approximated as linear, the stress becomes,

$$T_{ij} = \sum_k \sum_l c^E_{ijkl} S_{kl} - \sum_k e_{kij} E_k, \tag{2.19}$$

where E_k is the electric field, e_{kij} is the piezoelectric tensor, and the superscript E on the stiffness tensor indicates the electric field is assumed to be constant. This modified equation for stress leads

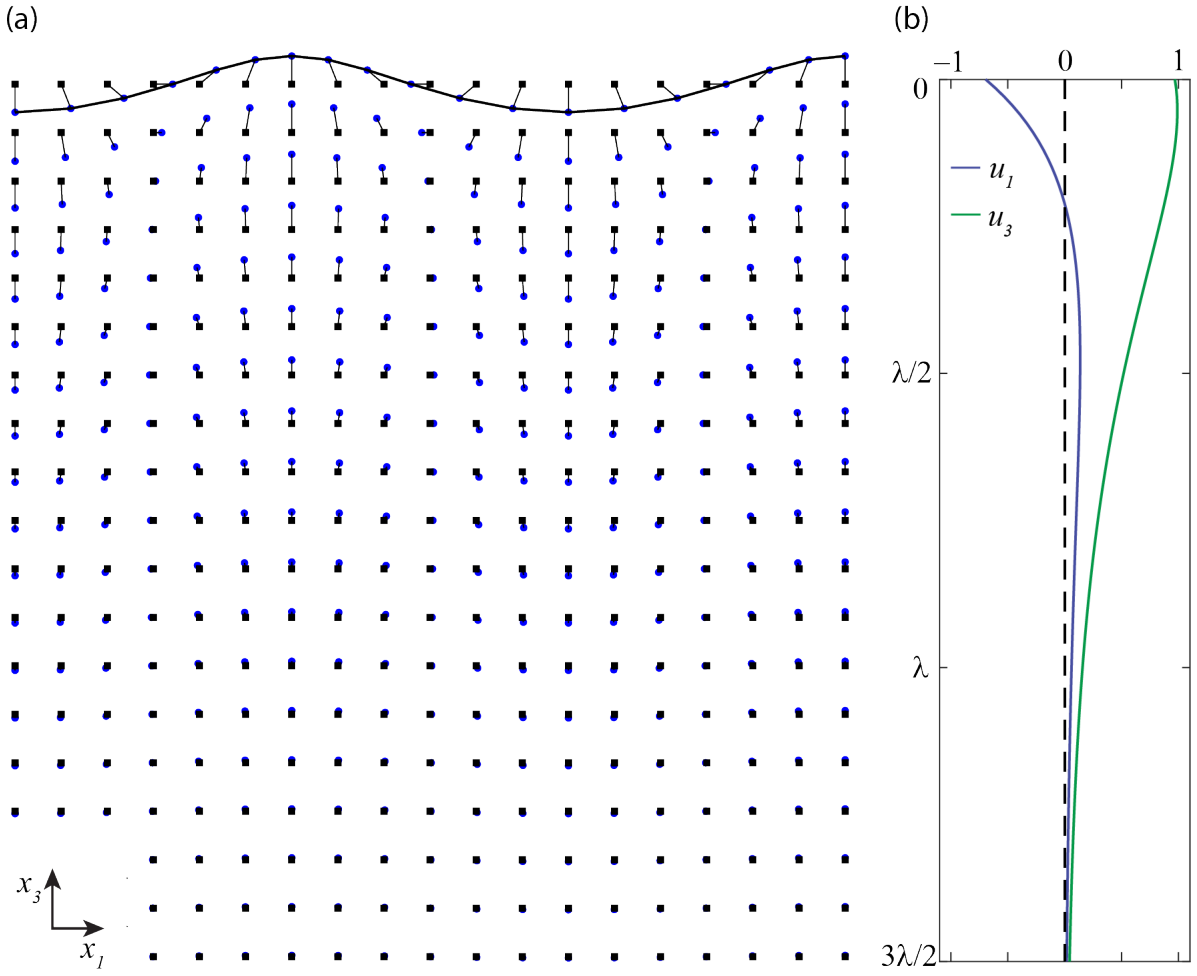

Figure 2.1: The strain of a Rayleigh wave in the sagittal plane on fused quartz, shown as a grid in (a) and a vertical line cut in (b). Particles move in ellipses as the u_1 and u_3 displacements are out of phase, and the grade of the ellipse is different on the surface compared to the bulk as the sign of u_1 changes. The magnitude of the strain decays quickly into the bulk, with most of the mechanical energy stored within λ of the surface.

to a more complicated equation of motion,

$$\rho \frac{\partial^2 u_i}{\partial t^2} = \sum_j \sum_k \left(e_{kij} \frac{\partial^2 \Phi}{\partial x_j \partial x_k} + \sum_l c^E_{ijkl} \frac{\partial^2 u_k}{\partial x_j \partial x_l} \right), \tag{2.20}$$

where Φ is the electric potential, and it is assumed that the electric fields vary slowly enough in time to be governed by electrostatics. This assumption is valid as sound travels much more slowly than electromagnetic excitations.

This equation of motion combined with the assumption that the material is an insulator

with $\nabla \cdot \mathbf{D} = 0$ gives four equations for u_i and Φ. These equations generally have four distinct solutions. One of these solutions is electrostatic in nature, essentially reducing to Laplace's equation. The other three solutions are of more interest, as each is a dispersionless acoustic wave with some general characteristics reminiscent of the isotropic case. In most cases, one solution closely resembles a longitudinal wave with displacement nearly parallel to its wavevector, while the other two resemble shear waves with two different polarizations and phase velocities. Additionally, the underlying anisotropy means the waves have phase velocities that depend on propagation direction. This angular dependence leads to many important effects, including modified diffraction and beam steering where the fronts of constant phase are not perpendicular to the flow of energy.

Similar to the isotropic case, surface waves can be constructed from these solutions by adding them together. However, the added complexity precludes analytical results in most cases, instead requiring computational methods. The reduced symmetry permits surface waves to have displacements in all three directions, despite having no variation out of the sagittal plane. Here, we are concerned with the class of solutions with displacements only in the sagittal plane, which are called piezoelectric Rayleigh waves and typically occur on surfaces and directions involving high degrees of symmetry. These waves share many properties of Rayleigh waves on an isotropic material, including the characteristic penetration depth of about one wavelength. Modified diffraction and beam steering arising from crystal anisotropy are considered more in Ch. 6.

One key difference from the isotropic, non-piezoelectric case is that for a piezoelectric Rayleigh wave the electrostatic boundary condition must be specified in addition to the mechanical one. There are two cases to consider: when the surface is free and when it is has a thin metallic layer present. In the free-surface case, it is assumed there are no free charges and there will in general be a non-zero potential in the vacuum above the surface. In the metallized case, the electric field parallel to the surface is shorted out by a thin conductor whose mechanical properties are assumed to be negligible. Crucially, this metallized boundary condition results in velocity v_m that is slower than the free-surface velocity v_f. The normalized difference $K^2 = (v_f - v_m)/(2v_f)$ is a direct measure of how strongly the wave interacts with electrical disturbances at the surface and will be

used heavily later in the work. The factor of two is included by convention.

2.2 SAW resonators

Surface acoustic waves are by nature propagating fields. To use these acoustic fields to store and process quantum information, they must be confined to form resonant modes. The resonators we use here are analogous to optical Fabry-Perot cavities where a pair of mirrored surfaces reflect and confine light. However, any localized element that strongly reflects SAWs also scatters energy out of the cavity, typically into shear bulk modes. To circumvent this unwanted scattering, SAW reflectors are formed by a periodic array of weak perturbations, such as metal strips or etched grooves, that are highly reflective only in aggregate.

2.2.1 Bragg Grating

Periodic arrays of surface perturbations, known as distributed Bragg gratings, are capable of efficiently reflecting incoming waves but require a more complicated description than localized reflectors. The periodicity inherent in the grating results in a dispersive behavior that both limits the bandwidth over which the grating is reflective and alters the phase of scattered waves.

A Bragg grating is defined by its periodicity p, complex reflectivity per element r_s, and number of elements N_m. These parameters combine to determine the gratings reflection coefficient Γ. To begin, I will first consider waves propagating in an infinite grating. These waves travel either right or left, and are uncoupled in the space between the grating elements. Consider the wave amplitudes at half-way between elements n and $n-1$ as shown in Fig. 2.2(a). Reflection from the mirror element couples the leftward travelling waves b to the rightward travelling waves c. The relationship between these four waves is given by two linear equations,

$$b_{n-1} = (r_s c_{n-1} + t_s b_n)\exp(-jkp), \tag{2.21}$$

$$c_n = (r_s b_n + t_s c_{n-1})\exp(-jkp). \tag{2.22}$$

where t_s is the transmission through the elements. The waves on the left can be expressed in terms

of those on the right by first re-arranging the first equation for b_n and substituting this into the second equation,

$$b_n = -\frac{r_s}{t_s} c_{n-1} + \frac{1}{t_s} b_{n-1} \exp(jkp) \tag{2.23}$$

$$c_n = \frac{1}{t_s} c_{n-1} \exp(-jkp) + \frac{r_s}{t_s} b_{n-1}, \tag{2.24}$$

where power conversation is assumed ($t_s = \sqrt{1 - |r_s|^2}$). Solutions in the grating will have the form $c_n = c_{n-1} \exp(-j\gamma p)$. Plugging this into the above equations relates γ to k and the grating parameters,

$$\cos(\gamma p) = \frac{\cos(kp)}{t_s}. \tag{2.25}$$

When t_s is close to unity, meaning each element is weakly reflective, this equation generally has a real solution for γ that is approximately k. However, when kp is near a multiple of π, then $\cos(kp)/t_s$ is larger than one and γ must have an imaginary part even for t_s close to one. The real and imaginary part of γ as a function of k_f are shown in Fig. 2.2(b). A non-zero imaginary component to the wave-vector implies that waves decay exponentially in the grating, and energy conservation then implies that waves incident on the grating with frequencies inside this stop band must be completely reflected.

We are concerned primarily with the first stop-band of the grating. This band has center frequency $f_0 = v_s/(2p)$ with a width Δ_m given by the range in k where $\mathrm{Im}(\gamma)$ is non-zero,

$$\frac{\Delta_m}{f_0} = \frac{2}{\pi} \sin^{-1}(|r_s|). \tag{2.26}$$

All incident waves in this band are perfectly reflected, so that $|\Gamma| = 1$. However, the phase of Γ changes with frequency, shifting by π over the mirror bandwidth. This reflected phase, θ_m, is given by the relation,

$$\theta_m = \theta_r + \tan^{-1}\left(-\frac{k - k_0}{\alpha}\right), \tag{2.27}$$

where $\theta_r = \pm\pi/2$ is the phase of single element reflections, k is the wave vector outside the grating, $k_0 = \pi/p$ is the Bragg wave-vector, and $\alpha = \sqrt{|r_s|^2/p^2 - (k - k_0)^2}$ is the imaginary part of the wave vector inside the grating. The phase shift is approximately linear near the center of the

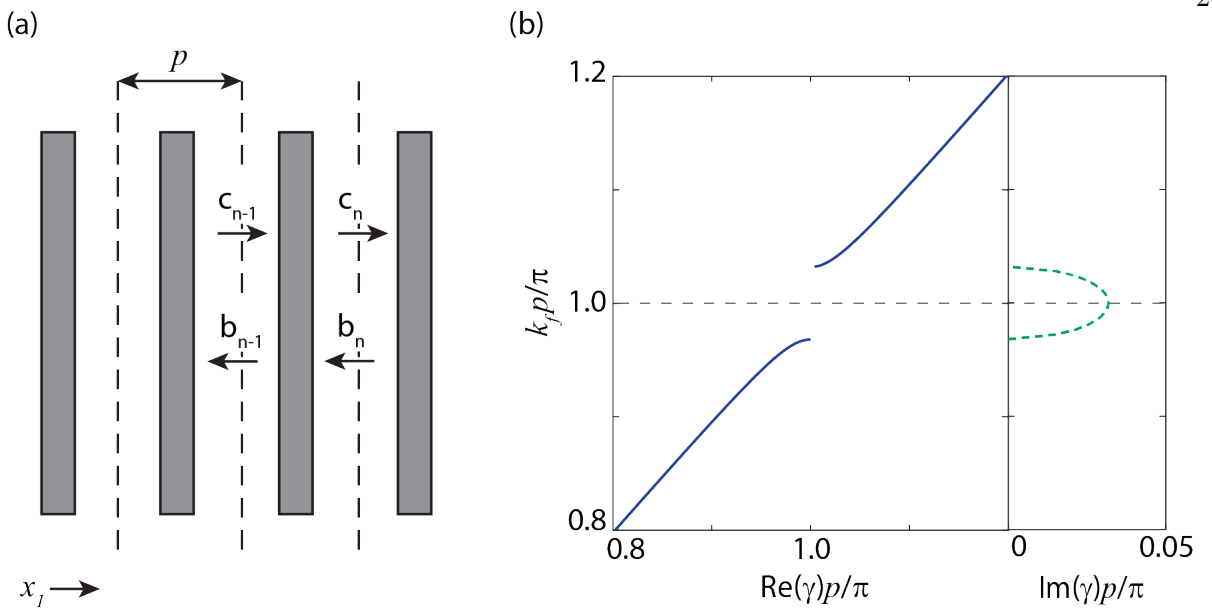

Figure 2.2: (a) A simple model of a mirror, considering fields travelling left and right as well as exiting and entering a given mirror element, can be used to determine the disperision of a SAW in a Bragg mirror. (b) The mirror propagation constant γ in an infinite grating can be found by relating these four fields to each other and looking for a periodic solution. This propagation constant acquires an imaginary part for a range in k space around π/p determined by the reflectivity per mirror element.

band, resulting in a delay $\tau_m = -d\theta_m/d\omega = (4f_0|r_s|)^{-1}$. Therefore, at the center of the stop-band, the Bragg grating functions as a perfect, localized reflector positioned at $L_p = v_s\tau_m = p/(2|r_s|)$ inside the reflector. However, the dispersion in the mirrors means that the penetration length L_p is frequency dependent and increases dramatically near the mirror band edge.

Finite gratings have reflections coefficients of magnitude below one as there is non-zero transmission through the mirror stack. At the center of the stop-band, the total reflection is given by,

$$|\Gamma| = \tanh(N_m|r_s|). \tag{2.28}$$

Therefore, the array reflects incoming waves effectively when $N_m|r_s| \gg 1$. Waves with wave-vectors near the edge of the stop-band penetrate further into the mirror, and those waves with an imaginary part that is small compared $1/N_m$ will be partially transmitted through the mirror. The reflected magnitude and phase from several finite Bragg gratings are depicted in Fig. 2.3.

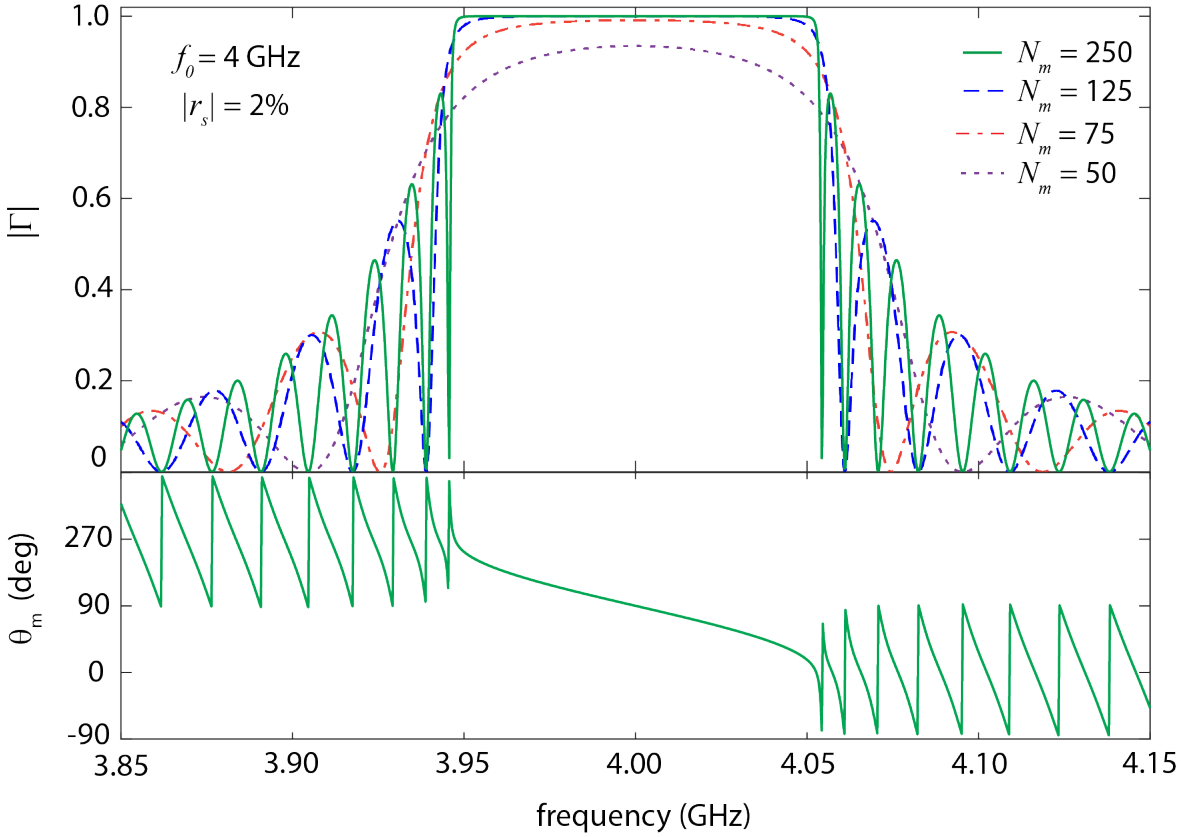

Figure 2.3: The reflection coefficient of a finite Bragg grating near its center frequency approaches unity when the number of elements is sufficiently large. Additional elements increase the magnitude of the reflection coefficient near the edges of the mirror stop-band. The phase of the reflection coefficient changes by π over the mirror bandwidth with an approximately constant delay τ_m near the center of the stop-band.

Bragg gratings for SAWs are most often implemented either with shallow grooves etched into the surface or metal strips deposited on top. To avoid significant scattering to bulk modes, r_s is typically between $1-3\%$, resulting in bandwidths that are $\sim 1\%$ of f_0 and penetration lengths of $\sim 35p$. The magnitude and sign of the reflectivity depend on the exact parameters of the element. The performance of various grating types have been studied on common materials to develop phenomenological models [7, 77]. Several strategies have been pursued to suppress conversion to bulk waves, including so called "hiccup" cavities where the mirrors and periodic structure used

for transduction discussed in Sec. 2.2.4 are directly adjacent to each other, offset only by a small phase shift (or "hiccup") to reduce the geometric discontinuity at the mirrors, [78] as well having a grating everywhere with a smoothly tapered periodicity [79] to create the cavity.

2.2.1.1 Numerical Modelling

The analysis above assumes power conservation and works well for simple geometries. The mirror behavior including loss, which usually results from scattering of surface waves into unconfined bulk modes, or more complicated geometries involving multiple periodicities must be determined numerically. Here, I describe a matrix formulation from Ref. [80] designed for cascading many circuit components together and can handle arbitrary geometries of several hundred elements easily. While this model is concerned with voltages and currents of microwave circuits, it applies readily to the mechanical displacement and pressure in a surface acoustic wave and is perhaps more intuitive than the P-matrix formalism commonly used in SAW analysis [7].

The voltages and currents at the input and output of an arbitrary two-port network can be related with a 4-element matrix, inventively called the $ABCD$ matrix. The relationships are given by,

$$\begin{bmatrix} V_1 \\ I_1 \end{bmatrix} = \begin{bmatrix} A_1 & B_1 \\ C_1 & D_1 \end{bmatrix} \begin{bmatrix} V_2 \\ I_2 \end{bmatrix}. \tag{2.29}$$

These $ABCD$ matrices are useful because they can be easily cascaded. If another arbitrary two port-network is in series with the first, then the matrix corresponding to both elements in series is simply the product of the two matrices. The behavior of any series of two-port networks with matrices M_i can be described by a matrix $M_t = \prod_i M_i$. This final matrix includes any complicated series of internal reflections and can be turned into final scattering parameters using simple formulas [Eq. 2.31]. Calculating the response of complicated combinations of two-port networks then becomes determining the individual $ABCD$ matrices and multiplying them together, a computationally easy task.

For calculating the reflection from a Bragg mirror, there are 2 matrices to consider: propa-

gation in free space and propagation in the mirror element. The $ABCD$ matrix for propagation over length l_i in a medium with velocity v_i and impedance Z_i is,

$$M_i = \begin{bmatrix} \cos(\omega l_i/v_i) & j\sin(\omega_i/v_i) * Z_i \\ j\sin(\omega l_i/v_i)/Z_i & \cos(\omega l_i/v_i) \end{bmatrix}, \tag{2.30}$$

where ω is the frequency of the wave. Losses can be included by adding an imaginary component to the propagation term $\omega l_i/v_i$. In this model, reflections are generated from an impedance mismatch at the interface between the region of free space with impedance Z_f and the mirror element with impedance Z_m. Typically, the acoustic impedances in the two regions are difficult to measure. However, the measured mirror bandwidth for a uniform grating can be used to infer the reflectivity per element, which then constrains the impedances to match $|r_s| = (Z_m - Z_f)/(Z_m + Z_f)$.

Once the component matrices are multiplied together, the final $ABCD$ matrix M_t determines the reflection coefficient of the entire stack Γ,

$$\Gamma = \frac{A_t + B_t/Z_f - C_t Z_f - D_t}{A_t + B_t/Z_f + C_t Z_f + D_t}. \tag{2.31}$$

The model prediction for Γ is only sensitive to the relative difference between impedances, and so the only inputs needed are the reflectivity per element and center of the mirror bandwidth.

This technique is most useful when describing non-uniform gratings. Such a structure holds promise in engineering a mirror with a built-in frequency-dependent delay. This extra dispersion leads to resonant cavities with non-uniform mode spacings which could be used for building an acoustic quantum random access memory [26]. The simplest implementation of this is a two-tone mirror, with a short segment at the mirror stack with a shifted center frequency from the rest. The short segment adds a frequency dependent delay, while the rest of the stack provides the majority of the confinement.

2.2.2 Fabry-Perot Cavities

An acoustic resonator analogous to optical Fabry-Perot cavities can be formed by placing two Bragg mirrors on axis with each other separated by length L. A wave propagating on axis inside

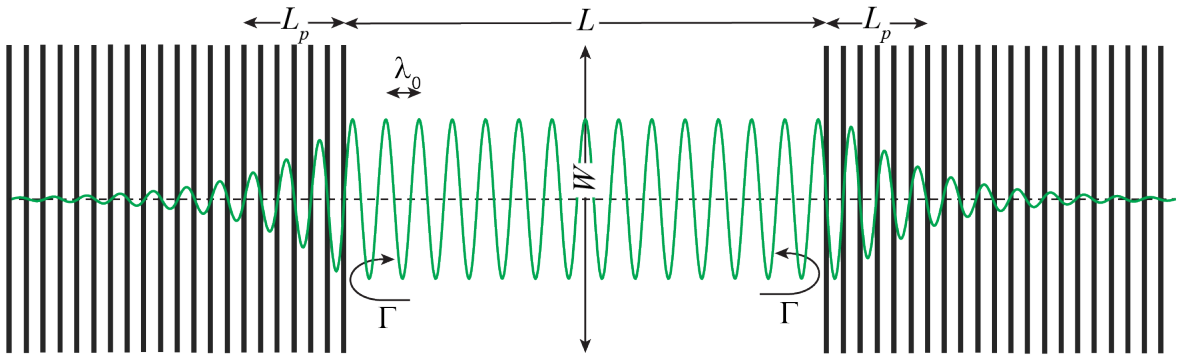

Figure 2.4: Two Bragg gratings can form a Fabry-Perot type resonator. The penetration of waves into the distributed mirrors results in an effective cavity length $L_e = L + 2L_p$.

the cavity with frequency inside the mirror stop-band will be confined between the two mirrors, as shown in Fig. 2.4. Resonance occurs when the frequency of the wave is such that it acquires a phase of 2π in a round trip.

To find the resonant condition, one must consider two sources of phase. The dominant phase is acquired when the wave traverses the separation between the two mirrors, where it picks up a phase $\theta_L = \omega L/v_p$ where v_p is the phase velocity of the wave. The wave also acquires a phase θ_m when it is reflected off the Bragg grating, given by Eq. 2.27. Near the center of the mirror stop-band, the mirror phase increases as approximately $\tau_m\omega$ resulting in an effective cavity length $L_e \approx L + 2\lambda_0/(4|r_s|)$. This approximately constant cavity length leads to an even spacing between resonant modes of $w_s \approx 2\pi v_s/(2L_e)$. However, dispersion in the mirrors leads to a faster accumulation of phase with frequency and consequently reduced mode spacing near the edge of the mirror bandwidth.

Once the resonant frequencies ω_m of the cavity are determined, the standing wave of the

acoustic modes can be defined explicitly. The surface potential $\phi_m(x)$ for mode m is piecewise,

$$\phi_m(x) \propto \begin{cases} \exp[2\sigma x]\sin(k_0 x - \theta_m) & x \leq 0 \\ \sin(k_m x - \theta_m) & 0 \leq x \leq L \\ (-1)^m \exp[2\sigma(L-x)]\sin(k_0(L-x) - \theta_m) & L \leq x \end{cases} \tag{2.32}$$

where $\sigma = \sqrt{|r_s|^2/p^2 - (k-k_0)^2}$ is the decay constant inside the mirrors, $k_m = \omega_m/v_s$ is the wavevector in free space, and $k_0 = \pi/p$ is the Bragg wavevector. The symmetry of the cavity about its center at $x = L/2$ implies that resonant modes have either either nodes or anti-nodes at the cavity center. While the mirror phase spatially shifts the modes relative to each other near the mirror, the resonant modes near the center of the mirror band are only shifted by a small phase, resulting in the anti-nodes of most modes occurring close together near the mirror. The standing waves near the mirror are discussed further in Ch. 6.

Commercial applications usually use SAW resonators that only support a single resonance within the mirror bandwidth. These cavities are short, with $\omega_s < 2\omega_0|r_s|/\pi$. In this limit, the length must be chosen carefully so that a resonant mode occurs at the center of the mirror band [7, 70]. This thesis is more concerned with multi-mode cavities where the free spectral range is smaller than the mirror bandwidth, $\omega_s < 2\omega_0|r_s|/\pi$. These cavities support many modes, regardless of the exact cavity length.

2.2.3 Cavity Lifetime

The time it takes for a phonon confined to a cavity to decay is a key metric for evaluating its performance. The energy in an undriven cavity decays exponentially with characteristic decay time τ. Resonators are often measured using spectroscopy, and their Lorentzian linewidth κ are related to this decay time τ as $\kappa = 1/\tau$ where κ is in units of angular frequency. To calculate the linewidth measured in standard frequency units most commonly used in the lab, the lifetime must be multiplied by 2π. Cavity spectroscopy is discussed further in Sec. 2.3.1. The overall loss rate κ is composed of several independent channels κ_i that all remove phonons with some rate, and

$\kappa = \sum_i \kappa_i$. In multi-mode cavities, it is useful to classify these losses into two types: loss that occurs every oscillation and loss that only occurs every round-trip. Two dimensionless figures of merit are used to quantify these processes: the characteristic number of oscillation periods defines the quality factor $Q = \omega_0/\kappa$, and the number of round trips defines its finesse $\mathcal{F} = \omega_s/\kappa$. This distinction is useful when extrapolating to different cavity geometries: if the dominant process occurs once per round trip and therefore limits finesse, then making the cavity longer will improve the quality factor, while a cavity with a dominant Q-limiting process has the same linewidth regardless of cavity length. In optical cavities, scattering from mirrors is almost always dominant as light travelling in vacuum is practically dissipationless, and therefore finesse is the important, geometry-independent figure of merit.

There are several well known loss mechanisms of surface acoustic wave cavities. Any features on the surface of the material make the Rayleigh solutions imperfect and result in scattering to other acoustic modes, such as bulk modes or unconfined surface waves. This scattering occurs primarily at mirror elements or other patterning of the surface such as any metallic electrodes, but also at any defects the waves encounter. For common interfaces, like Al electrodes or grooves on quartz, phenomenological parameters exist to give approximate values for this scattering [55]. As mentioned at the end of section 2.2.1, several strategies exist for suppressing bulk scattering, however none eliminate the trade-off between mirror bandwidth and mirror finesse. Unsurprisingly, unwanted blemishes on the surface should be avoided, and high quality material and surfaces are of paramount importance. However, even on an unpatterned and unblemished surface, finite viscosity of the material leads to damping of acoustic waves, a property often characterized as material Q that is strongly dependent on temperature [23].

Another loss mechanism is transmission through the Bragg mirror. At the center of the stop-band, several hundred elements with $r_s \sim 1\%$ is sufficient to render this source of loss negligible. However, modes near the band-edge can still have significant leakage through the mirror. Even in an infinite but slightly lossy grating, modes near the band edge can be lossier due to increased time spent propagating inside the mirrors. These losses can be modelled effectively using $ABCD$

matrices.

A dominant source of dissipation in the cavities considered in this thesis is diffraction losses resulting from the finite transverse extent of the cavity combined with the use of parralel reflectors. The width of the mirrors W leads to a diffraction limited Q_d given by

$$Q_d = \frac{5\pi}{|1+\gamma|}\left(\frac{\lambda_0}{W}\right)^2 \tag{2.33}$$

where γ describes the modified diffraction on the surface due to material anisotropy [81], discussed further in Sec. 6.3.2. Interestingly, careful choice of materials can make $\gamma \approx -1$, leading to SAWs that do not diffract to first order. As other considerations frequently limit the cavity aperture W, deploying a minimally diffracting material is an active area of research [82]. On GaAs, the substrate used in Ch. 4 and Ch. 5, $\gamma = -0.537$, while on ST-X quartz, which is used in Ch. 6, $\gamma = 0.378$ [81].

Another effect of the cavities finite transverse extent is the existence of modes with nodes in the transverse direction. In typical plane-parallel geometries, these transverse modes are only weakly confined by the reflectors and are generally low finesse [83] with frequencies that can be approximated by considering the acoustic cavity as a rectangular waveguide. Several strategies have been used to suppressed transverse modes by changing the geometry of the transducers that are described in the following subsection. [84, 85, 86, 87, 88].

2.2.4 Interdigitated Transducers

Transduction between electrical and acoustic signals, crucial to measuring the cavities introduced in the previous section and generally to SAW technologies, is performed by a structure called an interdigitated transducer (IDT). The behavior of these transducers is of fundamental importance in designing devices, and so an effective analysis for understanding their design and behavior is necessary.

Generally, interdigitated transducers are an array of electrodes on a piezoelectric half-space. Typically, they are periodic and contain just two electrodes with many interleaved fingers, resembling two hands meshed together. A voltage applied between the electrodes generates strain in the

substrate and therefore launches a travelling surface wave. Conversely, a travelling SAW carries with it some spatially varying voltage. As a wave traverses the IDT, this voltage is imposed across the IDT electrodes. These structures are usually many wavelengths long to couple preferentially to waves on the surface with minimal excitation of bulk waves.

2.2.4.1 SAW Green's Function Approach

An analytical description of IDTs, drawn from [7], is based on Green's functions. Here, we focus on the electric potential $\phi(x,\omega)$ of a SAW, but all the dynamical quantities are related and could be used with the same effect. Surface waves are sourced by surface charge density $\sigma(x,\omega)$ on the electrodes of the IDT. This charge density in principle has two components: an electrostatic component $\sigma_e(x)$ from the applied voltage on the electrodes and a piezoelectric component $\sigma_a(x,\omega)$ generated by SAWs. Here, I take the quasi-static approximation where the surface charges can be calculated ignoring acoustic excitations and are therefore governed by electrostatics, a safe assumption on materials with weak piezoelectricity such as GaAs and quartz. The surface potential of the acoustic wave is given by,

$$\phi_a(x,\omega) = G_S(x,\omega) * \sigma_e(x), \tag{2.34}$$

where $*$ indicates convolution with respect to x. The acoustic Green's function is,

$$G_S(x,\omega) = j\frac{K^2}{2\epsilon_\infty}\exp(-jk_f|x|), \tag{2.35}$$

where K^2 is a common metric for the piezoelectric coupling strength to a given piezoelectric wave defined earlier, $\epsilon_\infty = \epsilon_0 + \sqrt{\epsilon_{11}\epsilon_{33} - (\epsilon_{13})^2}$ is an effective dielectric constant, and $k_f = \omega/v_f$. If a region is considered to one side of all the source electrodes, the absolute value of x in the Green's function can be replaced by x, and the acoustic potential is given by,

$$\phi_a(x,\omega) = j\frac{K^2}{2\epsilon_\infty}\overline{\sigma}_e(k_f)\exp(jk_f x). \tag{2.36}$$

where $\overline{\sigma}_e(k)$ is the Fourier transform of $\sigma_e(x)$. The acoustic potential is proportional to the Fourier transform of the charge density, which is defined by the geometry of the IDT. This means that the

spatial profile of the IDT translates directly into the frequency profile of the transduction. The speed of sound provides the scaling, which at a few km/s implies that MHz frequency resolution can be achieved on the mm scale.

2.2.4.2 IDT Admittance

The current response to an applied voltage V_t determines an IDTs performance as a transducer. The ratio of this current to the applied voltage is known as the admittance, and it is useful to separate this admittance into three separate components,

$$Y_t(\omega) = G_a(\omega) + jB_a(\omega) + j\omega C_t, \tag{2.37}$$

where $G_a(\omega)$ and $B_a(\omega)$ are the real and imaginary parts of the admittance resulting from interaction with SAWs, while $j\omega C_T$ is the electrostatic part of the admittance from the capacative nature of the IDT. This capacative part can be found directly by determining the current flow from the electrostatic charge density $\sigma_e(x) = V\rho_e(x)$,

$$I_e = j\omega V\left(W\int_x \rho_e(x)dx\right) = j\omega V C_t. \tag{2.38}$$

The acoustic part can be found in a similar fashion. To determine the acoustic part of the current, the applied voltage is replaced with the acoustic potential resulting from the drive, so that the acoustic current in a given electrode is $I_{an} = \rho_{en}(x)\phi_a(x,\omega)$. Then,

$$I_a = -j\omega W\int_{-\infty}^{\infty}\sum_n \hat{P}_n\rho_{en}(x)\phi_a(x,\omega)dx \tag{2.39}$$

$$= -j\omega W\int_{-\infty}^{\infty}\rho_e(x)\phi_a(x,\omega)dx. \tag{2.40}$$

The acoustic potential is given by Eq. 2.36 but it is valid only in regions to one side of all electrodes. Using this restricted solution is sufficient to calculate the acoustic conductance,

$$G_a(\omega) = \omega W\frac{K^2}{2\epsilon_\infty}|\overline{\rho}_e(k_f)|^2 \tag{2.41}$$

where $\overline{\rho}_e(k) = \overline{\sigma}_e(k)/V_t$. The solution to ϕ_a over all space is tedious to derive because of the absolute value of x in the Green's function but this solution is required to determine the acoustic

susceptance. The conductance and susceptance are the real and imaginary parts of an analytic function as guaranteed by causality, so they can be related by Kramers-Kronig relations [89]. This then gives the gives the acoustic susceptance,

$$B_a(\omega) = -\omega W \frac{K^2}{2\pi\epsilon_\infty}\left[|\overline{\rho}_e(k_f)|^2 * k_f^{-1}\right] \tag{2.42}$$

where $*$ represents convolution with respect to k_f.

2.2.4.3 Common IDT Geometries

Typical IDT geometries permit the charge distributions $\rho_e(x)$ to be accurately approximated with simple expressions. The primary assumption that leads to convenient calculations is that the electrodes are periodic and edge effects are negligible, so that each element in the array has the same charge distribution. The charge distribution can then expressed as a combination of an element factor $\rho_f(x)$ describing the charge on individual electrodes and an array factor $F(x)$ to account for the electrode repetition and connectivity. The total charge density $\rho_e(x)$ is the convolution $\rho_f(x) * F(x)$, and thus the Fourier transform $\overline{\rho}_e(x)$ is the product of the transforms, $\overline{\rho}_e(k) = \overline{\rho}_f(k)\overline{F}(k)$.

The array factor $F(x)$ is given by a sum of delta functions at each electrode location,

$$F(x) = \sum_n \hat{P}_n \delta(x - x_n), \tag{2.43}$$

where x_n are the positions of the electrodes and $\hat{P}_n = 1$ if the electrode is connected to the driven electrode and is zero if connected to the grounded one. Later, it is convenient to define the a frequency-dependent factor that is normalized,

$$A(k) = \overline{F}(k)/N_p. \tag{2.44}$$

For an IDT with electrodes of alternating polarity of pitch p with N_p periods,

$$\overline{F}(k) = \frac{\sin(N_p k p)}{\sin(kp)} \approx \frac{N_p \sin(X)}{X}, \tag{2.45}$$

where $X = \pi N_p(\omega - \omega_0)/\omega_0$ and the approximation is accurate for frequencies near f_0.

IDTs with alternating polarity between electrodes, known as single-finger IDTs, often suffer from high reflectivity at the same frequency they efficiently launch sound. Each metal strip in the transducer perturbs the waves passing underneath, resulting in a weak reflection. For single-finger IDTs, each element is spaced by a half-wavelength at its center frequency, so that these small reflections add coherently; the IDT then behaves as a Bragg grating with a center frequency matching the frequency where it effectively transduces sound. Using thin metal and only a small number of finger periods can diminish the IDTs reflectivity. Reflections can be suppressed further if the metal electrodes are recessed into the surface, thereby reducing the geometric discontinuity [84, 88] but requiring a more complicated fabrication process. Alternatively, the IDT geometry can be modified so that the electrodes have polarity that alternates in pairs (i.e. 0,0,1,1,...). This doubling up of electrodes results in a mechanical Bragg frequency that is twice the frequency where the IDT launches efficiently SAWs. This geometry, known as a split-electrode IDT, is a powerful tool for suppressing reflections from the IDT electrodes, but comes at the cost of a capacitor with half the pitch, increasing both the capacitance for a given transducer and the demands on lithography. These two common types of IDTs are depicted in Fig. 2.5. The array factor for the split finger IDT is unchanged near its center frequency.

The Fourier transform element of the factor for an infinite array of electrodes, while closed-form, is still somewhat complicated. This factor is given by,

$$\overline{p}_f(\beta) = \epsilon_\infty \frac{2\sin \pi s}{P_{-s}(-\cos\Delta)} P_m cos(\Delta) \quad \text{for } m \leq \frac{\beta p}{2\pi} \leq m+1, \tag{2.46}$$

where $\Delta = \pi a/p$, a is the metallization ratio, P_{-s} is a Legendre function and P_m is a Legendre polynomial, m is the Bruillion zone of interest (equivalently, the harmonic), and $s = \beta p/(2\pi - m)$, so that $0 \leq s \leq 1$. The metallization ratio a, which greatly effects the elemental charge density, is the fraction of the pitch occupied by an electrode. While the array factor is usually more important in determining the frequency response of the IDTs, it is important to consider the elemental charge density, as for standard geometries there are certain harmonics that are allowed by the array factor but the elemental charge density is near zero. In particular, single-finger IDTs with $a = 0.5$ do not

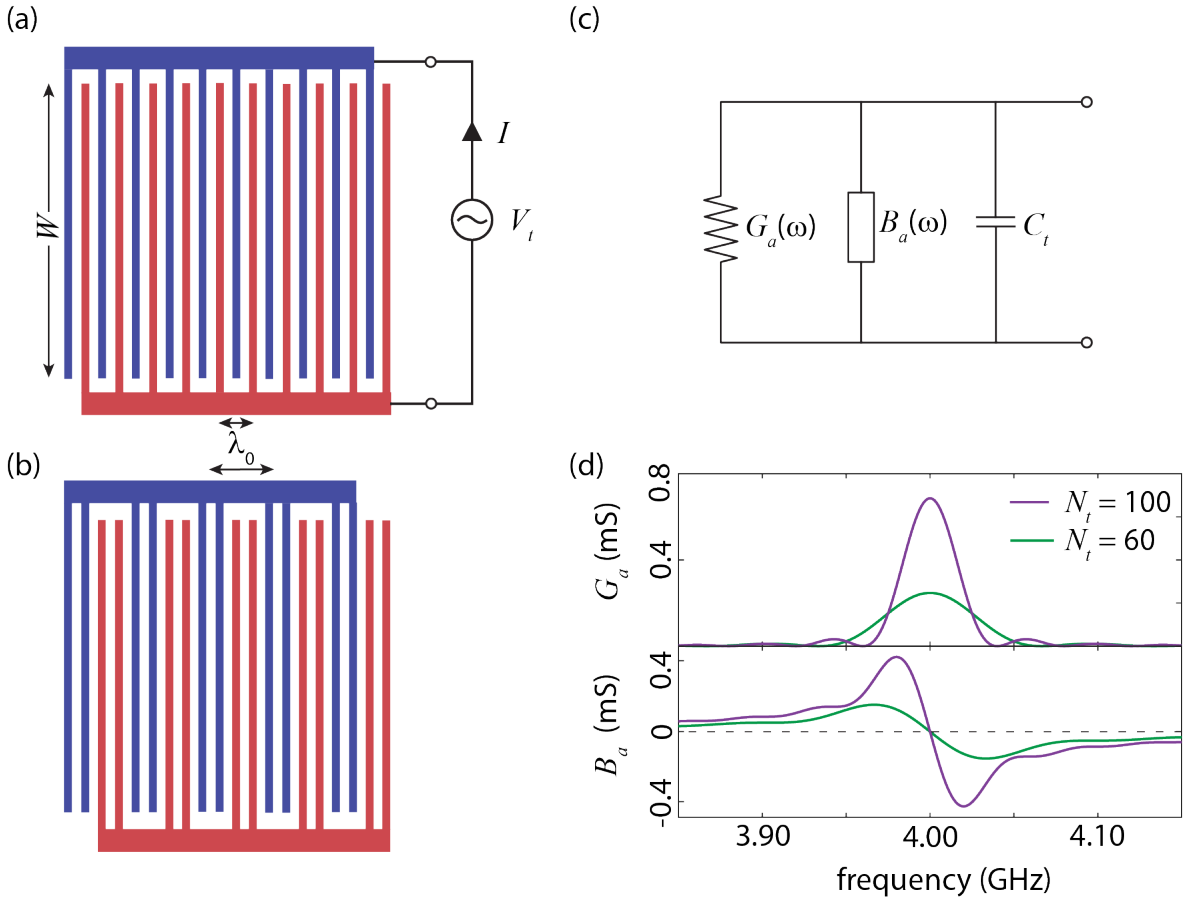

Figure 2.5: Typical IDT geometries are either (a) single-finger or (b) split-electrode. (c) These IDTs are well-modeled by a frequency-independent capacitance in parallel with an acoustic conductance G_a and susceptance B_a. (c) The calculated admittance and conductance (in milli-Siemens) are shown for an IDT with either $N_t = 100$ or $N_t = 60$ periods on GaAs with a 4 GHz center frequency and W=25 µm.

launch at the third harmonic.

For most applications, the array factor will be the dominant source of the frequency dependence of the IDT. For a single-electrode IDT with N periods of electrodes of pitch p, at frequencies near $\omega_c = 2\pi v_s/(2p)$,

$$G_a(\omega) = G_{a0}\left(\frac{\sin X}{X}\right)^2, \tag{2.47}$$

and, by Hilbert transform,

$$B_a(\omega) = G_{a0}\frac{\sin(2X) - 2X}{2X^2}. \tag{2.48}$$

The prefactor G_{a0} comes from the elemental charge distribution evaluated near ω_c. For both single and split finger IDTs, this term is given by,

$$G_{a0} \approx 1.3\omega_c C_s W K^2 N_P^2. \tag{2.49}$$

The acoustic susceptance and conductance for a typical transducer on GaAs are shown in Fig. 2.5. The term C_s is the capacitance per unit finger length and is related to ϵ_∞. For a split-electrode IDT, the capacitance is given by,

$$C_t = \sqrt{2} N_p W C_s. \tag{2.50}$$

For a single-finger IDT, the capacitance is $\sqrt{2}$ smaller.

A common use of IDTs is to make a delay line by launching sound from one transducer and receiving it at the other. The slow speed of sound means the delay can be several microseconds long on a mm sized chip. However, SAW delay lines are often quite lossy. On most materials, the IDT launches sound in both directions with equal amplitude, resulting in half the signal being lost at launch and by reciprocity the same at reception. On a weak piezoelectric material and at high frequencies, it is difficult to make the IDT impedance close to 50 Ω that is the typical characteristic impedance of microwave transmission lines, resulting in large reflections at the IDT. With enough finger periods, the conductance can be made close to 1/50 Siemens, but the associated capacitance begins to short out the launch.

2.3 Externally Coupled Cavities

The properties of acoustic structures, such as Fabry-Perot type cavities, can be probed using purely electrical techniques by using an IDT to convert an electromagnetic probe tone to an acoustic wave, which then interacts with the structure of interest before being converted back to electricity and measured.

For measuring Fabry-Perot type SAW resonators, two general geometries are possible. In the first geometry, the mirrors are made to be semi-transparent and an IDT is positioned on each side of the cavity. Transmission from one IDT to the other will increase when the driving frequency

matches an acoustic resonance, where energy builds up inside the cavity. This style of measurement is analogous to how optical cavities are probed, but poses two challenging tasks in the acoustic domain: the IDT must efficiently transduce SAWs into free space, and the mirrors must have just the right reflectivity to let enough energy through to facilitate measurement without significantly increasing the cavity loss rate. Alternatively, an IDT could be placed inside the cavity, as shown in Fig. 2.6. In this geometry, the IDT launches sound directly into the cavity. On resonance, the drive rings up the cavity, and the relative amplitude of the signal leaking back out the IDT increases, resulting in a change in reflection on resonance discussed more thoroughly in Sec. 2.52. In this thesis, I will focus primarily on the second geometry with the IDT inside the cavity. This design benefits from resonant enhancement of the IDT launch efficiency and no constraints on the reflectivity of the mirrors.

The behavior of the IDT changes significantly when placed inside a resonator. The SAWs that are launched do not simply propagate away, but are confined by the mirrors. The interaction of the IDT with these confined waves confined can be modelled using the strategies like $ABCD$ matrices. However, a simpler and more intuitive approach is to assume the cavity supports high-Q resonant modes and consider how the IDT interacts with these discrete resonances.

An IDT connected to a transmission line and placed inside the cavity behaves in many ways like an additional source of dissipation for the resonant modes. A confined wave that traverses the IDT generates an electrical signal that then travels down the transmission line, never to return. This interaction decreases the lifetime of a phonon in the cavity. In the limit that the cavity finesse is much higher than one, this loss rate is given by,

$$\kappa_e = 4.4 G_a(\omega) Z_c \frac{v_s}{L} \zeta(x)^2 \tag{2.51}$$

where Z_c is the characteristic impedance of the transmission line connected to the IDT, $G_a(\omega)$ is the acoustic conductance given in Eq. 2.41, and $\zeta(x)$ characterizes the spatial alignment between IDT and the acoustic standing wave. Essentially, the IDT extracts fractional energy $G_a Z_c$ every round-trip time L/v_s for an IDT with electrodes at the antinodes of a given standing wave where

$\zeta(x) = \pm 1$. Since IDTs are distributed, SAW cavities are many wavelengths long, and the Bragg gratings result in frequency dependent boundary conditions, $\zeta(x)$ can be difficult to predict for a given mode. Symmetry can be helpful; for example, at the cavity center all even modes have an an anti-node and all odd modes have a node. The most robust method is to compare the IDT electrodes to the standing waves described in equation 2.32.

The "loss" caused by energy entering a transmission line is special because, while the effect on the overall cavity lifetime is the same as other sources of dissipation, the energy extracted by the transmission line is not really lost as it can be measured. This type of loss is referred to as an external coupling rate. In addition to being measurable, external coupling rates are usually set intentionally when designing resonators. In contrast, internal losses are typically unwanted, arising from various dissipation mechanisms described in section 2.2.2.

2.3.1 Input-Output Theory

The internal and external coupling rates of a general resonator, acoustic or electric, can be extracted by measuring the scattering of signals from external coupling ports as a function of frequency. The response can be derived from input-output theory as described below. This formalism is useful not only in its simplicity, but also because it extends readily to a quantum mechanical descriptions.

Let $a(t)$ describe the state of the phonon field inside the resonator normalized such that $|a(t)|^2\hbar\omega$ is the energy circulating in the cavity. The rate of change of $a(t)$ depends on the various cavity coupling rates as well as the incident fields. In a frame rotating with the incident field,

$$\dot{a}(t) = -\frac{\kappa}{2}a(t) + i\Delta a(t) + \sqrt{k_1}a_{1,inc}(t) + \sqrt{k_2}a_{2,inc}(t) \tag{2.52}$$

where $\kappa_{1,2}$ are two external coupling rate, $\kappa = \kappa_1 + \kappa_2 + \kappa_i$ is the total cavity linewidth with internal loss rate κ_i, Δ is the detuning between the incident field and the cavities resonant frequency, and $a_{inc}(t)$ is the incident field on port 1 or 2, normalized so that $|a_{1,inc}(t)|^2\hbar\omega$ is the incident power on port 1 of the cavity. To make these equations describe a quantum systems, all of the field terms

a's must become operators, and an additional noise term $\kappa_i f_{inc}$ has to be included to account for unavoidable quantum fluctuations from cavity dissipation.

The steady state internal field generated in response to a constant incident drive is found by setting $\dot{a}(t) = 0$. Then,

$$a(t) = \frac{\sqrt{\kappa_1} a_{1,inc}}{\kappa/2 - i\Delta}. \tag{2.53}$$

The magnitude of $a(t)$ gives the number of circulating phonons,

$$\overline{n} = |a(t)|^2 = \frac{\kappa_1}{\Delta^2 + (\kappa/2)^2} \frac{P_{in}}{\hbar\omega_0}. \tag{2.54}$$

where P_{in} is the power incident on port 1. Intuitively, a resonant drive results in an intracavity phonon number equal to the number of phonons arriving in a cavity lifetime multiplied by ratio of external to total coupling rates.

The reflected field $a_{1,out}$ is composed of both the promptly reflected incident signal $a_{1,inc}$ as well as the field leaking out from the cavity, such that $a_{1,out} = a_{1,inc} - \sqrt{\kappa_1} a$. The reflection coefficient, defined as the ratio of the output field to the input, is given by,

$$\mathcal{R} = 1 - \frac{\kappa_1}{\kappa/2 - i\Delta} = \frac{2i\Delta + (\kappa_i + \kappa_2) - \kappa_1}{2i\Delta + (\kappa_i + \kappa_2) + \kappa_1}. \tag{2.55}$$

This reflection coefficient depends strongly on the ratio κ_1/κ. When $\kappa_1 \ll \kappa$, the reflected field is composed mostly of promptly reflected signal, and its phase is always between $-\pi/2$ and $\pi/2$. In this regime the port is called "under-coupled". When $\kappa_1 \approx \kappa$, the port is "over-coupled" and on resonance the reflected signal is predominantly energy leaving the cavity. Crucially, measuring reflection from an overcoupled port contains a full 2π phase phase wrap across resonance. Finally, if $\kappa_1 \approx \kappa/2$, then the cavity is critically coupled, and on resonance, the promptly reflected signal perfectly cancels the field leaking out of the cavity, resulting in a vanishing reflection coefficient.

The magnitude of the reflected signal is invariant under the exchange $\kappa_1 \leftrightarrow \kappa_2 + \kappa_i$. In the extremes of over- and under-coupled regimes, $|\mathcal{R}| \approx 1$. Thus, if only the amplitude of the reflected signals is considered, it is impossible to tell if the given response is under- or overcoupled, as shown if Fig. 2.6(b). Measuring the phase of the cavity response is the key to differentiating over- and

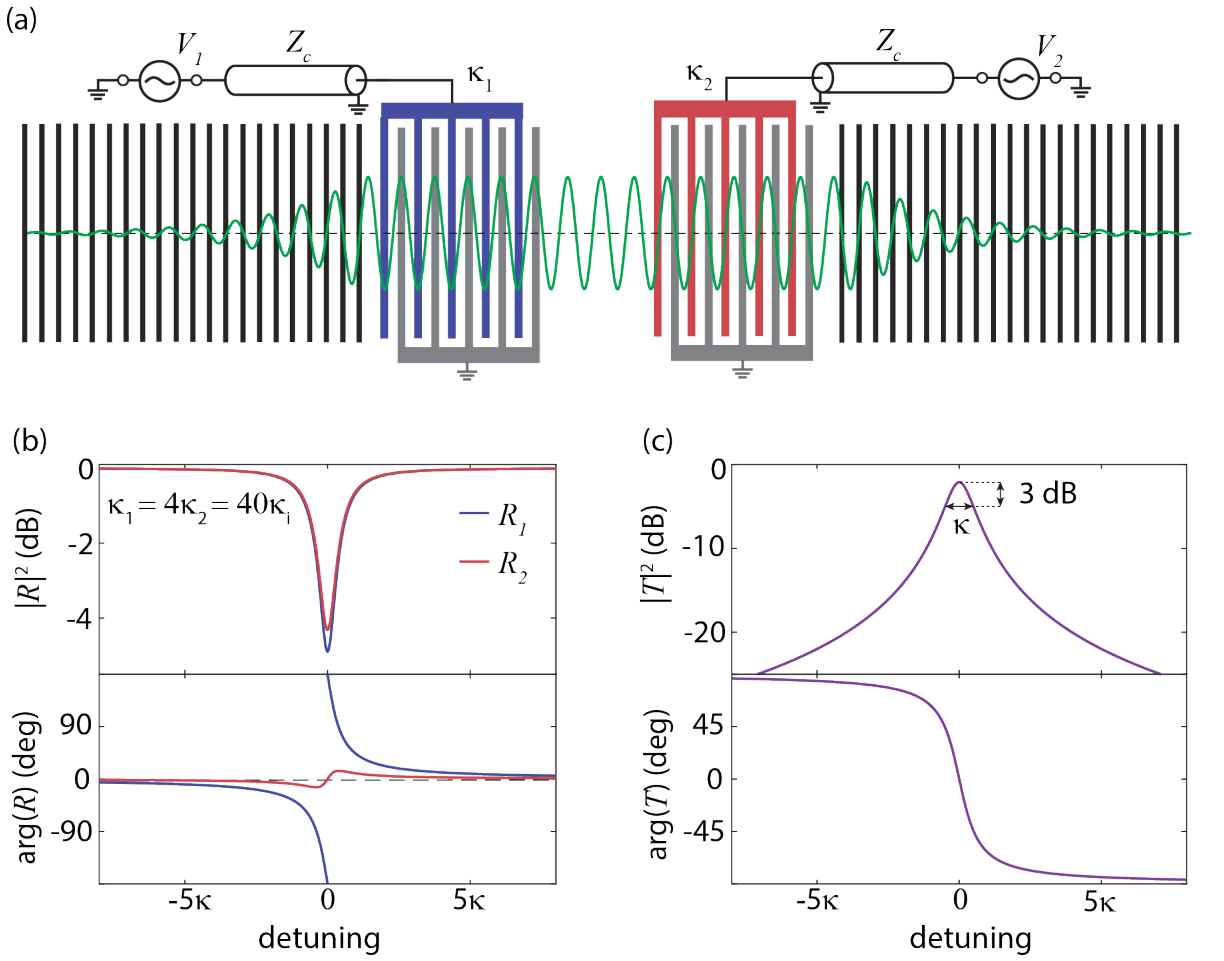

Figure 2.6: (a) The response of an IDT placed inside an acoustic Fabry-Perot cavity can be characterized in terms of internal and external coupling rates. Note that the right IDT (red) couples weakly as the cavity standing wave has nulls at the IDT finger positions. (b-c) The complex reflection off each port and transmission through the cavity are plotted for $\kappa_1 = 4\kappa_2 = 40\kappa_i$. In reflection, the phase information is crucial as the difference between the over- and under-coupled port cannot be distinguished in magnitude alone.

under-coupled resonances. When considering only reflection, the external coupling out the second port can be regarded simply as an additional source of loss.

The transmission from one port to the other is given by,

$$\mathcal{T} = \frac{\sqrt{\kappa_1 \kappa_2}}{\kappa/2 - i\Delta}. \tag{2.56}$$

The phase of the transmitted signal changes by π across resonance regardless of the coupling rates. The magnitude of transmission reaches unity on resonance when $\kappa_1 = \kappa_2$ and $\kappa_i = 0$. These

conditions mean both ports 1 and 2 are critically coupled, so that no power is reflected, and as no power is lost, then it all must be transmitted. The transmitted power is often the most accessible quantity experimentally. It is given by,

$$|\mathcal{T}|^2 = \frac{4\kappa_1\kappa_2}{\kappa^2 + 4\Delta^2}. \tag{2.57}$$

The transmitted power falls to half of its max at $\Delta = \kappa/2$, and so κ is referred to as the full-width-at-half-max, or FWHM, and is the convention used here for specifying a linewidth.

The general results from input-output theory apply easily to describing multi-mode SAW resonators. Including multiple resonant modes is a fairly-straight forward extension of the model, requiring an additional cavity field for each mode, but all with the same input and output fields. The modes are independent, so each has its own linear differential equation as in Eq. 2.52. The output fields have contributions from each resonance,

$$a_{out} = a_{inc} + \sum_m \sqrt{\kappa_m} a_m, \tag{2.58}$$

where m indexes the resonant mode with detuning Δ_m, external coupling $\kappa_{e,m}$, and total linewidth κ_m. The multi-mode reflection is given by,

$$\mathcal{R} = 1 - \sum_m \frac{\kappa_{e,m}}{\kappa_m/2 - i\Delta_m}. \tag{2.59}$$

The multi-mode transmission is just a sum of the transmissions for each resonant mode, with each consecutive mode increasing in phase by π. For most SAW resonators, the spacing between purely longitudinal modes is small compared to their linewidths. In this case, only one term in the sum is significant, and the single-mode case is good approximation. However, resonant modes with non-zero transverse mode number can be nearly degenerate with their corresponding longitudinal mode, and the multi-mode reflection case must be considered.

Chapter 3

Quantum Acoustics with Superconducting Qubits

Investigating quantum acoustics with surface acoustic waves requires a quantum description of the resonators described in the previous chapter. Additionally, a non-linear element is needed to escape the correspondence principle which limits linear quantum systems with classical control to replicate classical physics. In this chapter, I introduce a quantum description of acoustic resonators and superconducting qubits then conclude with a description of the coupled qubit-cavity system.

3.1 Quantum Harmonic Oscillator

The simple harmonic oscillator is a canonical model in physics and in quantum mechanics in particular. While introduced as a mass on a spring, the description is applicable to a diverse range of physical systems including the resonant modes of surface acoustic wave cavities. The model consists of mass m connected to a spring with stiffness k such that a displacement from its equilibrium position x results in a restoring force $F = -kx$. The Hamiltonian for the system is,

$$H = \frac{1}{2m}\hat{p}^2 + \frac{k}{2}\hat{x}^2, \tag{3.1}$$

where $\hat{p} = m\frac{d\hat{x}}{dt}$ is the momentum. The quantum nature of this Hamiltonian comes from the commutation relation between position and momentum, $[\hat{x}, \hat{p}] = i\hbar$. This relation can be manipulated to define the creation and annihilation operators $\hat{a}$ and $\hat{a}^\dagger$,

$$\hat{a} = \sqrt{\frac{m\omega}{2\hbar}}\left(x + \frac{i}{m\omega}p\right), \tag{3.2}$$

and $[\hat{a}, \hat{a}^\dagger] = 1$. Using these operators, the Hamiltonian can be rewritten as,

$$H/\hbar = \omega \left(\hat{a}^\dagger \hat{a} + \frac{1}{2} \right), \tag{3.3}$$

where $\hat{a}^\dagger \hat{a}$ is the number operator. This Hamiltonian has eigenstates $|n\rangle$ such that $\hat{a}^\dagger \hat{a}|n\rangle = n|n\rangle$ with energies $E_n = \hbar\omega(n+1/2)$. Crucially, the energy difference between all eigenstates is identical.

It is this equal spacing that precludes creating non-classical states of motion in harmonic oscillators with classical drives alone. Such a classical drive excites multiple transitions in the oscillator simultaneously, creating a coherent state $|\alpha\rangle$ that follows a Poissonian distribution in the number basis,

$$|\alpha\rangle = \exp\left[-|\alpha|^2/2\right] \sum_{n=0}^{\infty} \frac{\alpha^n}{\sqrt{n!}} |n\rangle. \tag{3.4}$$

Coherent states are eigenstates of the annihilation operator, $\hat{a}|\alpha\rangle = \alpha|\alpha\rangle$ with average excitation number $|\alpha|^2 = \overline{n}$. Importantly, the behavior of a quantum harmonic oscillator in a coherent state appears classical, albeit with unavoidable noise of quantum origins.

Another important state in the simple harmonic oscillator is the thermal state. When in thermal equilibrium with some bath of temperature T, the phonon probability distribution is given by,

$$P(n_{th}, n) = \frac{n_{th}^n}{(n_{th}+1)^{n+1}}, \tag{3.5}$$

where $n_{th} = [\exp(\hbar\omega/k_B T) - 1]^{-1}$ is the mean phonon number. To be cooled to its quantum ground state, the probability of zero phonons $P(n_{th}, 0)$ must be near one. This condition is reached when thermal energy $k_B T$ is be small compared to the transition energy $\hbar\omega$. At temperatures reached in modern dilution refrigerators of near 25 mK, mechanical oscillator must have frequencies larger than 500 MHz to be cryogenically cooled to their ground state.

Electromagnetic cavities are also well described as simple harmonic oscillators. Electromagnetic waveguide cavities and LC oscillators are of particular interest here for their role in superconducting circuit design and measurement. The waveguide cavity is described in more detail as the readout resonator in Sec. 5.2.1.1. The LC circuit is composed of a parallel inductor and capacitor, and is characterized by its resonant frequency $\omega = 1/\sqrt{LC}$ and impedance $\sqrt{L/C}$. A quantum

treatment can be developed by considering the charge on the capacitor $\hat{Q} = CV$ and the flux across the inductor $\hat{\Phi} = LI$, where V is the voltage and I is the current. The Hamiltonian for this systems is,

$$H = \frac{\hat{Q}^2}{2C} + \frac{\hat{\Phi}^2}{2L}, \tag{3.6}$$

with commutation relation $[\hat{Q}, \hat{\Phi}] = i\hbar$. The clear analogy between this system and the simple Harmonic oscillator means they have similar quantum behavior.

3.2 Superconducting Qubits

Superconducting qubits consist of low-loss microwave circuits with an inherent non-linearity that makes their spectrum anharmonic. While these circuits contain many energy levels with varying levels of complexity, the unequal transition frequencies allow individual pairs of levels to be considered exclusively. These pairs can be modelled as a two-level system and mapped to a spin-$\frac{1}{2}$ particle. The Hamiltonian for such a two-level system is,

$$H/\hbar = -\frac{1}{2}\omega_q \sigma^z. \tag{3.7}$$

where ω_q is the qubit frequency and σ^z is the Pauli matrix whose eigenstates have spin oriented along the z-axis, either pointing up or down. Here, I will refer to spin up as the ground state, denoted by $|g\rangle$, and spin down as the excited state, denoted by $|e\rangle$. Similar to the case of the harmonic oscillator, this system will be primarily in the ground state if $\hbar\omega_q \gg k_B T$.

3.2.1 Josephson Junctions

The element that makes superconducting qubits possible is the Josephson junction [90]. This element is formed by a superconductor interrupted by a thin insulating layer as shown in Fig. 3.1(a). In the superconductor, electrons form two electron bound states, known as Cooper pairs, and are characterized by a superconducting phase ϕ. When the insulating interruption is thin enough, typically around a few nm, Cooper pairs can tunnel across the barrier. Crucially, a discrete a phase difference δ can develop between the two superconducting islands. The voltage and current flowing

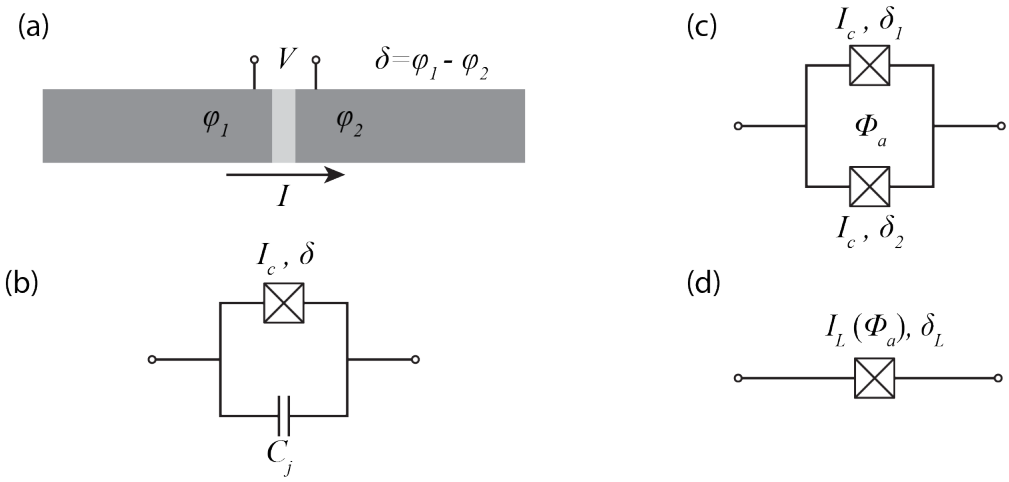

Figure 3.1: (a) A Josephson junction formed by two superconducting leads with an insulating barrier thin enough for Cooper pairs to tunnel across. The difference between the superconducting phases $\phi_1 - \phi_2 = \delta$ and the critical current (I_C) determines the voltage and tunnelling current and voltage across the junction. (b) Josephson junction schematic, including small (several fF) junction capacitance. (c) A DC squid is formed by two junctions in a loop threaded by flux Φ_a and acts as an effective (d) single junction with flux dependent critical current.

across the junction are given by the Josephson relations:

$$I = I_c \sin(\delta) \tag{3.8}$$

$$V = \frac{\Phi_0}{2\pi}\frac{d\delta}{dt}, \tag{3.9}$$

where I_c is the junction's critical current and $\Phi_0 = h/2e$ is the flux quantum.

These relations mean that a Josephson junction acts as a non-linear inductor. To see this, differentiate Eq. 3.8 with respect to time, and then substitute the resulting expression for $d\delta/dt$ into Eq. 3.9. This substitution gives,

$$V = \frac{\Phi_0}{2\pi}\frac{1}{I_c\cos(\delta)}\frac{dI}{dt} = \frac{L_{j0}}{\cos(\delta)}\frac{dI}{dt}. \tag{3.10}$$

The term $L_{j0} = \frac{\Phi_0}{2\pi I_c}$ is defined as an effective Josephson inductance when $\delta = 0$. The tunnelling of Cooper pairs across the junction stores energy much in the same was an inductor, however the relationship between δ and I means that this Josephson inductance changes with current. The

tunnelling energy of these electrons is equal to $E_J(\delta) = E_J \cos(\delta)$ where $E_J = I_c\Phi_0/2\pi$. In addition to an inductance, junctions have an inherent capacitance C_J between the two superconducting islands that depends strongly on its geometry. With the junctions and superconducting circuits we are interested in here, this capacitance is negligible.

A widely used element, known as a DC superconducting quantum interference device (SQUID), consists of two Josephson junctions connected end to end in a loop [Fig 3.1(c)]. In the case that these two junctions have the same critical current I_c, the DC squid acts much like a single Josephson junction with critical current $2I_C$ that decreases depending on the magnetic flux threaded through the SQUID loop. The effective critical current of the full loop is given by [91],

$$I_L = 2I_c \cos\left(\pi \frac{\Phi_a}{\Phi_0}\right). \tag{3.11}$$

where Φ_a is the applied flux. In this way, Josephson junctions can act as tunable, loss-less inductors.

Asymmetry between two junctions may need to be included when more accuracy is needed, particularly as current fabrication methods lead to variation in junction energies on the order of $5 - 10\%$. In the case of two junctions with critical currents I_1 and I_2, the effective critical current of the loop is given by,

$$I_L = (I_1 + I_2) \cos\left(\pi \frac{\Phi_a}{\Phi_0}\right) \sqrt{1 + d^2 \tan^2\left(\pi \frac{\Phi_a}{\Phi_0}\right)}, \tag{3.12}$$

where $d = \frac{I_1 - I_2}{I_1 + I_2}$ quantifies the junction asymmetry [92]. The effect of the asymmetry is small near applied flux near zero. However, near $\Phi = \pi/2$, the asymmetry prevents I_L from approaching zero.

Many useful electrical circuits can be made based on Josephson junctions. A diverse group of superconducting qubits have been realized using the non-linearity of the junctions integrated with different linear elements to design circuit Hamiltonians with desirable properties [43]. The non-linearity of Josephson junctions are also widely used to implement and 4 wave mixing in quantum limited parametric amplifiers [93, 94, 95, 96, 97]

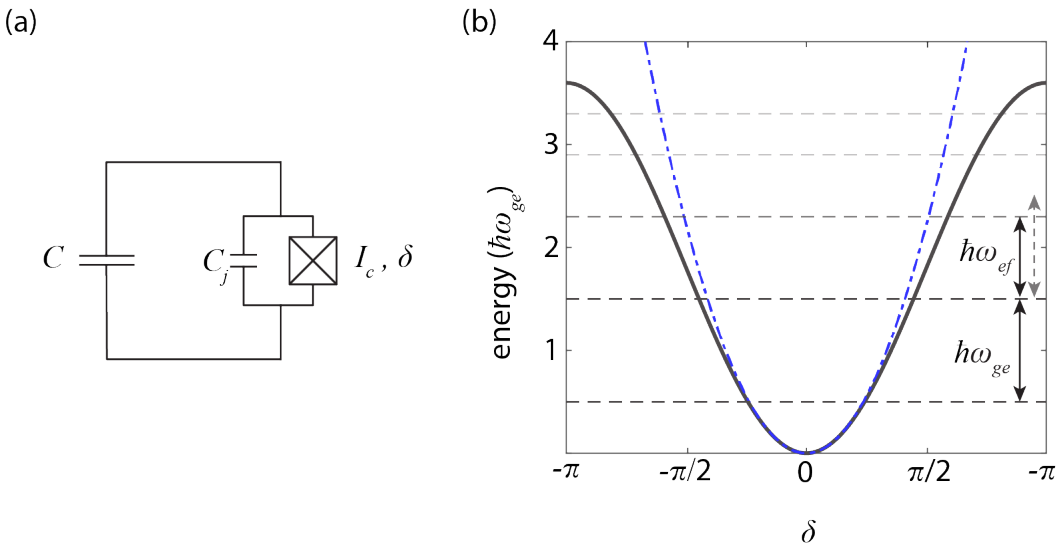

Figure 3.2: (a) The transmon qubit is formed by shunting a Josephson junction or DC squid with a large capacitance C such that $E_J/E_C \gg 1$. (b) The transmon acts as a flux particle in a cosine potential. The weakening potential at larger flux results in a negative anharmonicity α.

3.2.2 Transmon Qubit

A popular type of superconducting qubit, and the one primarily used in this thesis, is formed by shunting a Josephson junction with phase difference $\hat{\delta}$ by a large capacitance with charge $\hat{Q}$. This circuit has a Hamiltonian resembling an LC circuit,

$$H = \frac{\hat{Q}^2}{2C} + E_J \cos\left(\hat{\delta}\right), \tag{3.13}$$

where the cosine potential appears parabolic near its minima before weakening at larger δ. The transmon qubit is a limit of this Hamiltonian where the Josephson energy E_J greatly exceeds the charging energy $E_C = e^2/2C$. In this limit, the ground to excited state transition frequency is given by $\omega_{ge} = \sqrt{8E_C E_J}/\hbar$. Here, $\omega_{ge} = \omega_q$, but the two indices are included to clearly indicate other transitions are being considered. The higher order terms in $\cos\left(\hat{\delta}\right)$ lower the frequency of the next highest transition, so that $\omega_{ef} = \omega_{eg} - E_c/\hbar$. The transmon Hamiltonian can be well approximated

as a Duffing oscillator [92],

$$H = \sqrt{8E_J E_c}\hat{b}^\dagger\hat{b} + \frac{1}{2}E_c\hat{b}^\dagger\hat{b}\left(\hat{b}^\dagger\hat{b} - 1\right). \tag{3.14}$$

This slightly anharmonic oscillator can be treated as a qubit to the extent that ω_{ge} and ω_{ef} are spectrally distinct, which is usually a good assumption given that a typical transmon linewidth γ is below 1 MHz compared to an anharmonicity $\alpha = -E_c/\hbar$ of several hundred MHz. While the two lowest levels can be readily used as a qubit, many important properties of transmon qubits require including at least the $|f\rangle$ level during analysis [92].

The transmon limit involves a trade-off between charge noise sensitivity and anharmonicity. An ideal qubit is insensitive to noise while being very anharmonic. For the transmon Hamiltonian, increasing the ratio of E_J/E_C decreases the qubits sensitivity to charge noise but also decreases its anharmonicity. The sensitivity to noise decreases exponentially with E_J/E_C while the anharmonicity only decreases linearly. At least until $E_J/E_C \approx 50$, the exponentially suppressed noise sensitivity is well worth the linearly reduced anharmonicity, as charge noise has been a significant limit in qubit coherence times and a typical transmon anharmonicity of a few hundred MHz is sufficient for reasonably fast qubit operation. This simple design and its insensitivity to charge noise has led to a vast improvement in coherence times with low circuit complexity, and the state-of-the-art attempts to build a quantum computer with superconducting circuits use transmon qubits [98, 99, 100].

3.3 Jaynes Cummings Model

A fully quantum treatment of the interaction between a harmonic oscillator and a two-level system was introduced by Jaynes and Cummings [101]. Their simple model, first derived for atoms coupled to an optical cavity through their electric dipole moment (Fig. 3.3), captures many phenomena regarding the interaction between light and matter and has become a "standard model" of quantum optics [102]. While the harmonic oscillator of interest in this thesis is phononic in nature and the atom is a superconducting circuit, their model is general enough to accurately

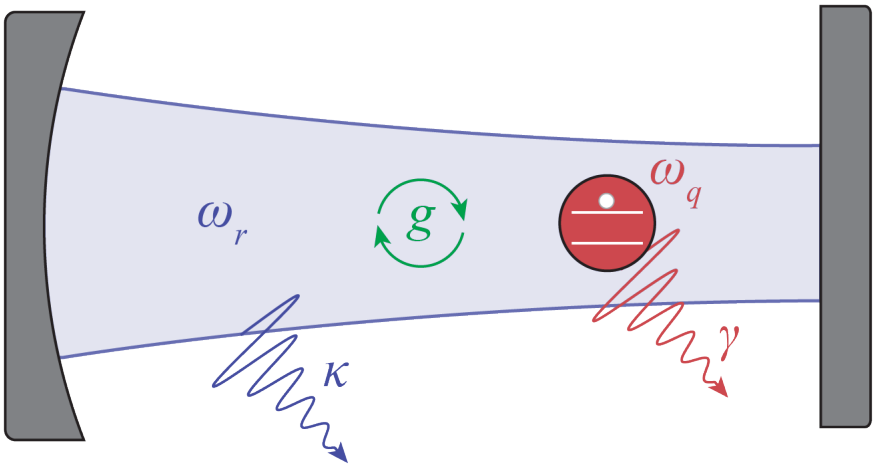

Figure 3.3: The Jaynes-Cummings model describes a two-level system with frequency ω_q and loss rate γ coherently exchanging excitations at rate g with a harmonic oscillator with frequency ω_r and loss rate κ.

describe the system. Indeed, the successful acoustic realization of the Jaynes-Cummings model is one of the fundamental results of this thesis.

In the Jaynes-Cummings model, an effective two-level system exchanges energy with a harmonic oscillator when the two systems are near resonance through a dipole interaction. The Hamiltonian for the coupled system is given by,

$$H_{JC}/\hbar = \omega_r \hat{a}^\dagger \hat{a} + \frac{1}{2}\omega_q \sigma^z + g\left(\hat{a}\sigma^+ + \hat{a}^\dagger \sigma^-\right), \tag{3.15}$$

where $\sigma^+(\sigma^-)$ is the qubit raising (lowering) operator and g is the rate at which the qubit and cavity exchange energy on resonance. As written here, the Hamiltonian ignores the counter-rotating terms $\hat{a}\sigma^-$ and $\hat{a}^\dagger\sigma^+$ that do not conserve the total number of excitations in the coupled system. Known as the rotating wave approximation, this simplification is valid when the coupling strength g and the detuning $\Delta = \omega_r - \omega_q$ between the two systems are small relative to the qubit and cavity frequencies.

The Jaynes-Cummings Hamiltonian in the rotating wave approximation can be exactly diagonalized because interactions only occur between states with the same number of total excitations.

When constructed in matrix form, the Hamiltonian is composed of two-by-two element blocks along its main diagonal, each block corresponding to a set number of excitations n_e,

$$H_{n_e}/\hbar = \begin{bmatrix} \omega_r n_e - \omega_q/2 & \sqrt{n_e}g \\ \sqrt{n_e}g & \omega_r(n_e - 1) + \omega_q/2 \end{bmatrix}. \tag{3.16}$$

These blocks can be diagonalized,

$$E_{\pm,n_E}/\hbar = n_e\omega_r \pm \sqrt{n_e g^2 + \Delta^2/4}, \tag{3.17}$$

where + (-) refers to the higher (lower) energy eigenstate in the n_e excitation manifold. The corresponding eigenstates are given by,

$$|-, n_e\rangle = \cos(\theta_n)|g, n\rangle - \sin(\theta_n)|e, n-1\rangle \tag{3.18}$$

$$|+, n_e\rangle = \sin(\theta_n)|g, n\rangle + \cos(\theta_n)|e, n-1\rangle \tag{3.19}$$

$$\theta_n = \frac{1}{2}\arctan\left(\frac{2g\sqrt{n_e}}{\Delta}\right), \tag{3.20}$$

where n is the number of excitations in the cavity and the effective angle θ_n characterizes the mixing between qubit and cavity states.

3.3.1 Resonant Regime

In analyzing this solution, it is useful to consider two distinct cases: the resonant regime when $\Delta \ll g$ and the dispersive regime when $\Delta \gg g$. The eigenvalues in each regime are shown graphically in the energy level diagram of Fig. 3.4. At small detuning, $\theta_n \approx \pi/4$ and the two eigenstates are approximately even superpositions of qubit and cavity modes with energy splitting $2g\hbar$, implying excitations are swapped at rate g. This is only true if the system is in the strong coupling regime, where the coupling rate g exceeds the dissipation rates of the qubit γ and the cavity κ. The hybridized modes inherit half of the qubit's loss and half of the cavity's, resulting in two modes each with a loss rate $(\kappa + \gamma)/2$.

The hybridization between the qubit and the cavity in the single excitation manifold can be well modelled using the normal modes of two coupled classical oscillators. The non-linear behavior

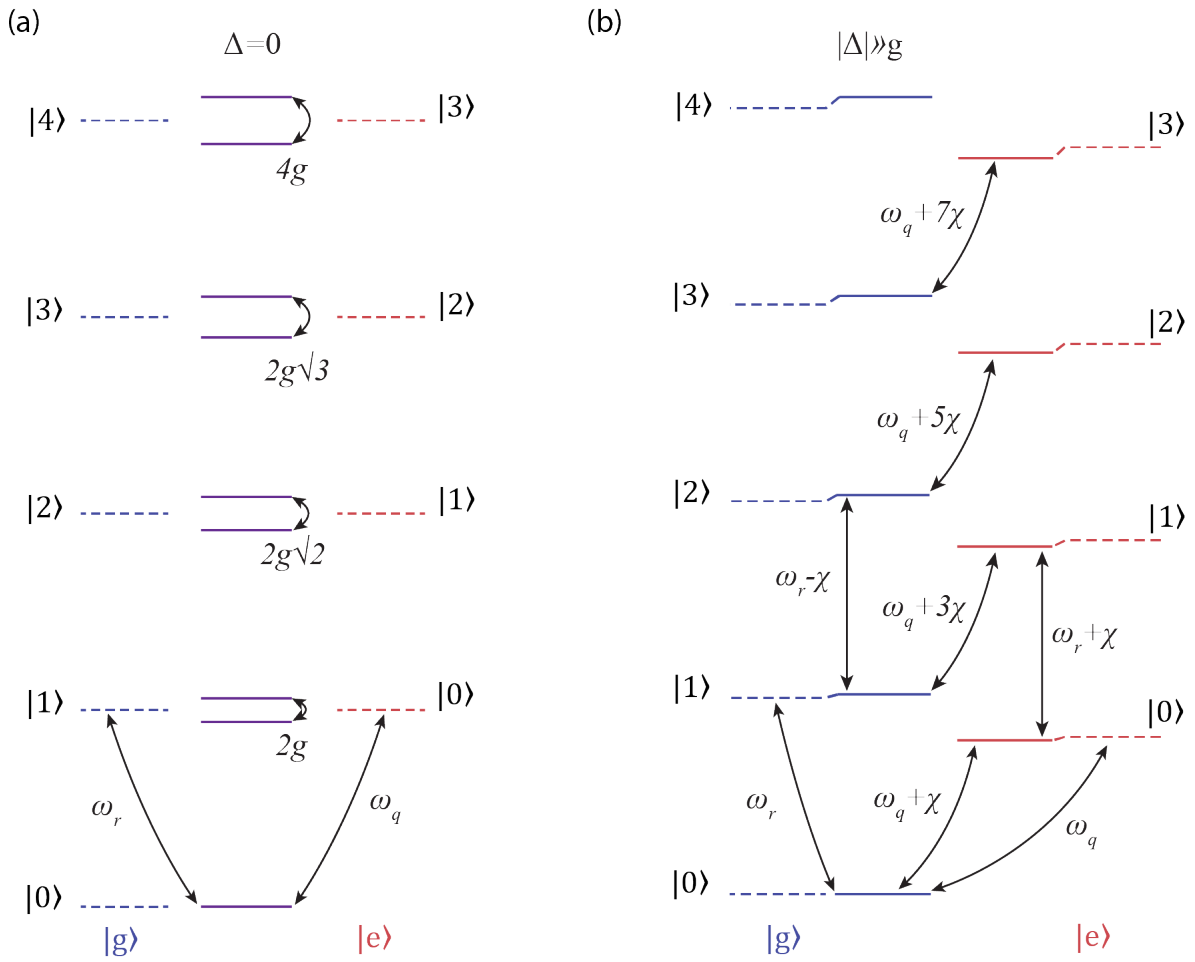

Figure 3.4: The Jaynes-Cummings model can be exactly diagonalized. (a) On resonance ($\Delta = 0$), the qubit and cavity form hybridized modes with a splitting that grows with total excitation number. (b) In the dispersive regime ($g/\Delta \ll 1$), the normal modes correspond closely to the uncoupled modes, but with resonant frequencies that shift by 2χ for each quanta in the other sub-system. In the case shown where $\omega_q < \omega_r$, the dispersive shift χ is negative.

of the Hamiltonian becomes apparent when the number of excitations in the system grows. Each additional quanta increases the qubit-cavity swap rate in discrete steps, growing as the square root of the cavity occupancy [103, 67]. Therefore, resonant swapping of excitations while measuring the exchange rate between a resonant qubit-cavity system performs a measurement of the cavity occupancy.

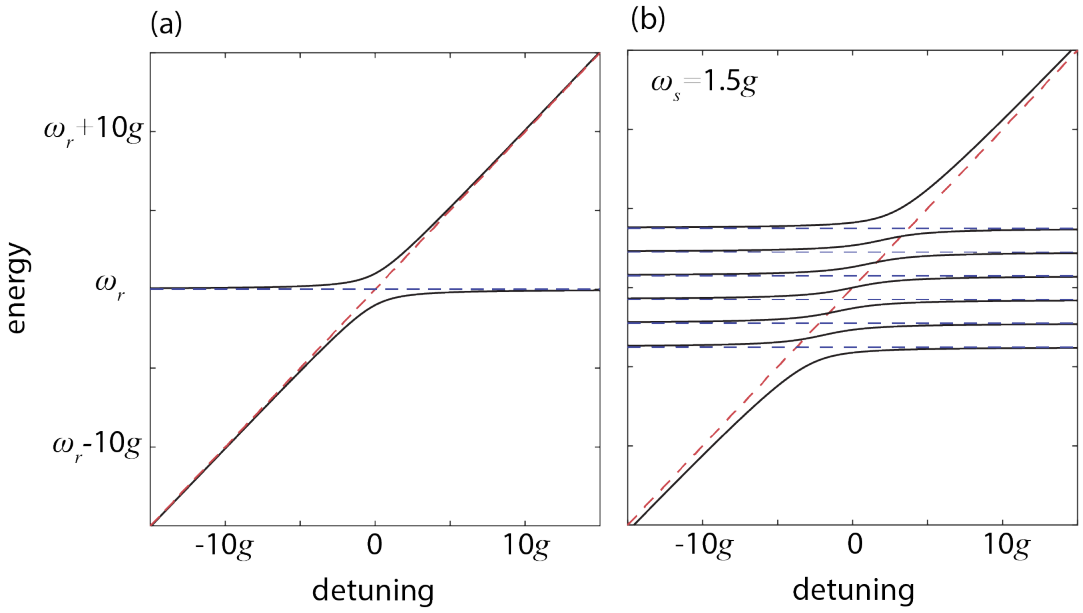

Figure 3.5: (a) As the qubit is tuned across the resonator, the eigenmodes avoid each other, reaching a minimum spacing $2g$ when $\Delta = 0$ and the eigenmodes are even and odd superpositions of qubit and cavity. (b) In the multi-mode regime where the coupling is on a similar scale to the spacing between modes $g \approx \omega_s$, the avoided crossings are more complicated.

3.3.2 Dispersive Regime

With increasing detuning, the hybridization between the qubit and the cavity weakens and the eigenvalues of the coupled system begin to approach their uncoupled values. This avoided crossing behavior is shown in Fig. 3.5(a). The dispersive regime is reached when the detuning is large enough that the eigenmodes correspond closely to the uncoupled qubit and cavity modes, such that $\theta_n \approx g/\Delta \to 0$. In this limit, the Hamiltonian can be approximated using a unitary transformation,

$$D = \exp\left[\frac{g}{\Delta}\left(\sigma^- a^\dagger - \sigma^+ a\right)\right]. \tag{3.21}$$

Keeping terms to second order in g/Δ of the transformed Hamiltonian $H_d = D^\dagger H_{JC} D$ gives the dispersive Hamiltonian,

$$H_d/\hbar = \omega_r \hat{a}^\dagger \hat{a} + \frac{1}{2}\omega_q \sigma^z + \chi \hat{a}^\dagger \hat{a} \sigma^z, \tag{3.22}$$

where $\chi = g^2/\Delta$ is known as the dispersive shift. This Hamiltonian has eigenvalues,

$$E_{g,n}/\hbar = n\omega_r - \omega_q/2 - n\chi \tag{3.23}$$

$$E_{e,n}/\hbar = n\omega_r + \omega_q/2 + n\chi, \tag{3.24}$$

which can also be found by expanding Eq. 3.17 for small g/Δ. This approximation not only assumes that $g/\Delta \ll 1$ but also that the mean photon number does not exceed $n_{\text{crit}} = (\Delta/2g)^2$ [104]. In physical systems, it has been observed that the dispersive approximation frequently breaks down at mean photon numbers well below n_{crit}.

The effect of the $\chi\hat{a}^\dagger\hat{a}\sigma^z$ interaction term is that excitations in one system shift the frequency of the other [Fig. 3.6, Fig 3.4(b)]. If the qubit is in ground state, then the cavity frequency is $\omega_{r,|g\rangle} = \omega_r - \chi$, while if qubit is in the excited state the cavity transition shifts to $\omega_{r,|e\rangle} = \omega_r + \chi$. The problem of determining the state of the qubit can then be mapped onto precise measurement of the resonant frequency of a harmonic oscillator. Moreover, since the interaction term commutes with the qubit part of the Hamiltonian, the measurement effect is only to project the qubit into eigenstates of σ^z, and repeated measurements yield the same answer. The ability to repeat measurements

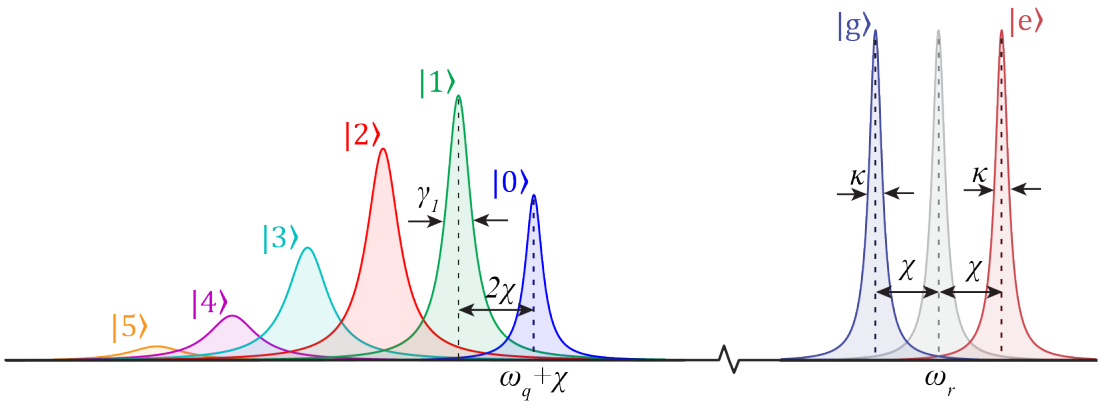

Figure 3.6: In the dispersive regime, the cavity frequency shifts by $\pm\chi$ from its bare resonant frequency ω_r depending on the state of the qubit. Similarly, the qubit frequency shifts by 2χ for every excitation in the cavity. If the cavity is displaced with a coherent state of size $\overline{n}$, then the qubit spectrum splits into multiple peaks, with weights reflecting the probability distribution of cavity excitations. The qubit is also dephased by the loss of cavity excitations which effectively perform measurements of the qubit state.

and measure the same result is known as a quantum non-demolition (QND) measurement [105]. Non-QND measurements include photon counting and other schemes where the quantum state is destroyed during measurement. Additionally, even performing dispersive readout with $\Delta \gg g$, using a coherent state with too large of an amplitude degrades the QND nature of the measurements. As this breakdown amplitude can be quite small, it is imperative to measure the cavity output with a low-noise amplification chain.

The dispersive Hamiltonian also means that the qubit frequency depends on the number of excitations in the cavity. In a semi-classical approximation, the qubit transition shifts smoothly, such that $\omega_{q,|n\rangle} = \omega_q - 2\chi\overline{n}$ where $|\alpha|^2 = \overline{n}$. However, if the qubit frequency can be resolved to better than χ, then this frequency shift is observed to be discrete, such that $\omega_{q,|n\rangle} = \omega_q - 2\chi n$. This so-called strong dispersive regime demonstrates the quantized nature of the excitations of the linear cavity and allows the qubit to measure the number of excitations in the cavity. Combined with displacement of the cavity mode, such measurements can lead to the full reconstruction of the cavity quantum state [106, 105, 52].

The residual hybridization between the qubit and cavity adds potential decay channels for both systems, called the Purcell effect. The coupled loss rates of the qubit γ' and cavity κ' are related to bare linewidths by,

$$\gamma' = \gamma + \left(\frac{g}{\Delta}\right)^2 \kappa, \tag{3.25}$$

$$\kappa' = \kappa + \left(\frac{g}{\Delta}\right)^2 \gamma. \tag{3.26}$$

Although g/Δ is small, this inherited loss can still be significant. Commonly, the cavity loss rate is made large ($\sim$MHZ) by engineering a large external coupling rate to facilitate readout, and even a small fraction of this loss can exceed the qubits intrinsic decay rate [107]. This effect can be circumvented by modifying the density of states as a function of frequency: if cavity is coupled to a transmission line that supports propagating modes at ω_r but not at ω_q, then the qubit sees a reduced density of states and its decay rate from the cavity loss rate suppressed [108].

For transmon qubits, including higher levels is required for accurate predictions of dispersive

physics. The presence of the $|f\rangle$ level modifies the dispersive shift,

$$\chi = g^2 \left(\frac{1}{\Delta} - \frac{1}{\Delta + \alpha} \right) \tag{3.27}$$

where $\alpha = \omega_{ef} - \omega_{ge}$ [92]. The two terms in this dispersive shift usually have different sign, reducing its magnitude. However, if g is small compared to α, then the transmon can be tuned such that $\omega_{ge} > \omega_r$ but $\omega_{ef} < \omega_r$. In this configuration, known as the "straddling regime", the two terms add constructively and boost the dispersive shift. In practice, this approximation is accurate when the highest frequency transmon level is below the cavity frequency. When the transmon frequency is above the cavity, however, higher transmon levels complicate the interaction, particularly when the cavity occupancy grows beyond a few excitations. This case requires numerical diagonalization using a truncated energy basis including several photons and several transmon levels, a process discussed further in Sec. 4.2.3.4.

3.3.3 Multi-mode Jaynes Cummings Model

Many cavities, both acoustic and electromagnetic, support multiple resonant modes. The multi-mode Jaynes Cummings Hamiltonian is a simple extension,

$$H/\hbar = \sum_m \omega_m \hat{a}_m^\dagger \hat{a}_m + \frac{1}{2}\omega_q \sigma^z + \sum_m g_m \left(\hat{a}_m \sigma^+ + \hat{a}_m^\dagger \sigma^- \right), \tag{3.28}$$

where $\hat{a}_m$ is the latter operator for mode with frequency ω_m and qubit coupling strength g_m. When the qubit is far detuned from all of the modes compared to their coupling strengths, then the multi-mode dispersive approximation gives,

$$H/\hbar = \sum_m \omega_m \hat{a}_m^\dagger \hat{a}_m + \frac{1}{2}\omega_q \sigma^z + \sum_m \chi_m \hat{a}_m \hat{a}_m^\dagger \sigma^z, \tag{3.29}$$

where $\chi_m = g_m^2/\Delta_m$ and $\Delta_m = \omega_m - \omega_q$. For most systems, the scale of the interaction strengths is small compared to the spacing between resonant modes. In this limit, the qubit will be in the dispersive regime with all modes but one and the analysis from the single-mode case can be accurately applied. If the spacing between different resonant modes is comparable to the interaction strength, then near resonance the model must consider possible hybridization between the qubit

and more than one mode [24]. The eigenvalues of these multi-mode systems, which are the focus of this thesis and are shown in fig. 3.5(b), must be calculated numerically. Interestingly, in the multi-mode limit, the strong coupling criteria is weakened such that clear avoided crossings no longer indicate that the coupling strength exceeds the decoherence rates of all sub-systems. In the multi-mode dispersive limit, the behavior is a simple sum of dispersive shifts from individual modes. However, when the coupling rate is much larger than the mode spacing, these shifts may differ significantly from g_m^2/Δ_m, a regime not accessed in this thesis.

3.3.4 Transmon Qubit-SAW Cavity Coupling Strength

To realize the Jaynes-Cummings model with surface acoustic waves coupled to a transmon qubit, we need to engineer a strong interaction between the two systems. This is achieved by using an interdigitated transducer on a peizoelectric material as the shunting capacitance in a transmon qubit. Such IDT geometries can have capacitances of several tens of fF, comfortable for the transmon regime corresponding to E_c of several hundred MHz.

The interaction between the transmon and acoustic waves can be calculated in much in the same way as that between a transmon with an electric dipole in a resonant electromagnetic cavity. Such an interaction is driven by the charge operator $\hat{n}$ which denotes the number of Cooper pairs transferred between the islands and is related to the transmon effective ladder operators as,

$$\hat{n} = \left(\frac{E_J}{8E_C}\right)^{1/4} \frac{\sqrt{2}}{2}(\hat{b}^\dagger - \hat{b}). \tag{3.30}$$

The coupling between cavity mode indexed by number m and the transmon transition from $|i\rangle$ to $|j\rangle$ is given by,

$$\hbar g_m = 2\beta e V^0_{\mathrm{rms,m}}(x)\langle i|\hat{n}|j\rangle A(\omega_m) \tag{3.31}$$

where $V_{\mathrm{rms,m}}(x)$ is the root mean squared zero-point voltage fluctuations of either the electromagnetic or piezo-mechanical resonator at location x, β is the ratio of coupling capacitance to total capacitance, and $A(\omega_m)$ captures the frequency sensitivity of the interaction and is absent in the electromagnetic case. As β is controlled in design and typically of order unity, three terms deter-

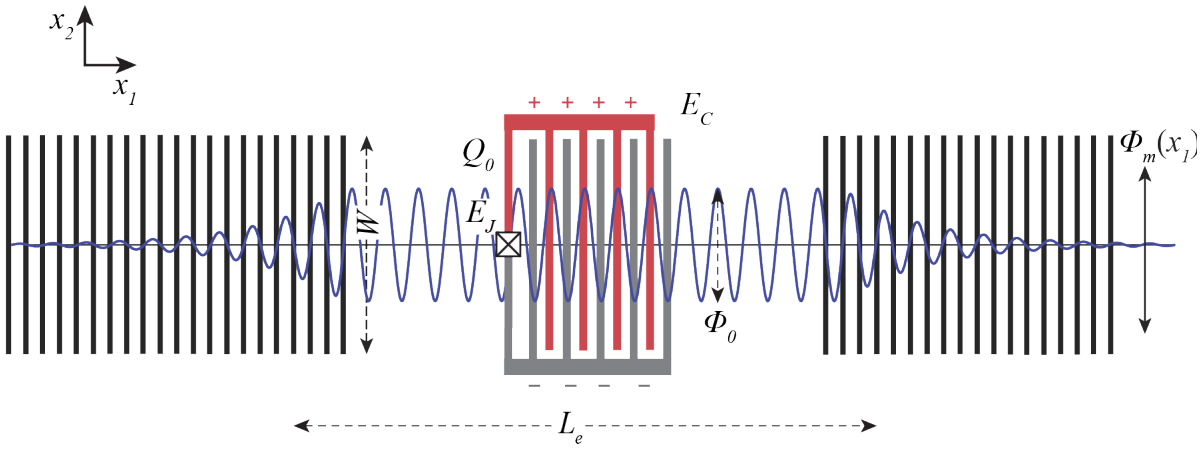

Figure 3.7: A transmon qubit that interacts strongly with a confined SAW mode can be formed by shunting an interdigitated transducer with a Josephson junction placed between two Bragg reflectors.

mine the coupling rate: the voltage fluctuations, the matrix elements, and the match of the IDT to the standing wave, both in frequency and position.

For a transmon, the only significant matrix elements are between nearest-neighbor transitions, with symmetry forbidding transitions between states of the same parity due to the lack of odd terms in the transmon potential [92]. Such nearest neighbor transitions have matrix element,

$$\langle j+1|\hat{n}|j\rangle = \sqrt{\frac{j+1}{2}}\left(\frac{E_J}{8E_C}\right)^{1/4}, \tag{3.32}$$

where $\hat{n}$ is the number operator of the island. This matrix element grows as $\sqrt{j+1}$ with increasing level. The dependence on the transmon energies E_J and E_C is weak, and does not strongly effect the coupling strength.

The main factor in determining the scale of interaction rate is the zero-point voltage fluctuations of the acoustic cavity. In most piezoelectric materials, the dominant form of energy is mechanical. The amplitude of the zero-point position fluctuations are then determined by calculating the displacement of a single phonon in mode m, given by $U_{0,m}$, with energy $\hbar\omega_m$,

$$U_{0,m}(x) = \sqrt{\frac{\hbar}{2\rho L_e W v_s}} U_m(x), \tag{3.33}$$

where ρ is the material density, L_e is the effective cavity length and W is its width, and v_s is the SAW velocity. These fluctuations depend on position based on the amplitude of the acoustic standing wave inside the cavity, given by $U_m(x)$ [Eq. 2.32]. The magnitude of the voltage fluctuations are related to this displacement by the piezoelectric properties of the material,

$$V^0_{\mathrm{rms,m}}(x) = \frac{e_{pz}}{\epsilon} U_{0,m}(x) \tag{3.34}$$

where ϵ is the dielectric constant of the material and e_{pz} is the appropriate element of the piezoelectric tensor in stress-charge form that depends on propagation direction. For weak piezoelectric materials like quartz and gallium arsenide, e_{pz}/ϵ is typically on the order of 1 V/nm.

The novel aspect of using an IDT rather than traditional dipole coupling is that the IDT samples the acoustic field at many many locations separated by many wavelengths. This multi-wavelength extent has implications for the strength of resonant interactions by introducing a frequency-dependent factor $A(\omega)$ in direct analogy to how the acoustic conductance depends on IDT geometry in Eq. 2.41. The dominant contribution to this term is the array factor $A(\omega)$ found by Fourier transform of the IDT geometry including the polarity of each finger as in Eq. 2.43 but normalized. As discussed in Ch.5, the coupling can be designed to have a specific frequency dependence to meet experimental needs [59]. Additionally, such "giant atoms" can be used to explore physics far outside the dipole coupled regime, including non-Markovian effects such as non-exponential decay [109].

All together, the coupling strength between an acoustic mode and the ground to excited state transition of a transmon can be calculated as,

$$\hbar g_m = e\beta \frac{e_{pz}}{\epsilon} \sqrt{\frac{\hbar}{\rho L_e W v_s}} \left(\frac{E_J}{8E_C}\right)^{1/4} A(\omega_m) U_m(x) \tag{3.35}$$

$$= g_0 A(\omega_m) U_m(x), \tag{3.36}$$

where g_0 characterizes the mode-independent strength of the qubit-acoustic coupling. For a transmon with most of its capacitance in the IDT and well-aligned to the acoustic standing wave, both in space and in frequency, then $\beta \approx 1$, $A(\omega_m) \approx 1$, and $U_m \approx 1$. In this thesis, the substrate is

typically GaAs, which has charge-strain piezoelectric tensor element $e_{pz} = 0.14$ C/m^2, dielectric constant $\epsilon = 12.5\epsilon_0$, density $\rho = 5307$ kg/m^3, and wave velocity $v_s = 2860$ m/s. For multi-mode cavities of somewhat narrow width, coupling rates of several MHz are achievable. Surprisingly, the number of fingers in the IDT does not significantly affect the coupling rate.

3.4 Waveguide Quantum Acoustodynamics

A tunable qubit coupled to a SAW resonator can interact with a continuum of unconfined phonon modes by tuning outside the mirror bandwidth. Access to these propagating phonons could be used to transfer information across a chip, while the distributed nature of the qubit-phonon coupling could lead to qubit-qubit interactions protected from waveguide losses [110]. Additionally, the slow travel time of SAWs could lead to novel routing schemes, where the destination of a wavepacket can be determined and altered during its relatively long transit time [111], or the creation of cluster states with using time-delayed feedback [112].

The spontaneous emission rate of a transmon qubit to a propagating SAW mode can be calculated semi-classically by considering the transmon qubit as a parallel RLC circuit with capacitance and inductance set by the E_J and E_C and a resistor determined by Eq. 2.41. This gives,

$$\Gamma_{10} = \omega_{ge}\frac{G_a(\omega_{ge})}{2}\sqrt{\frac{L_J}{C_\Sigma}} \approx \frac{1}{2}\sqrt{\frac{C_T}{C_\Sigma}}K^2\omega_{ge}G_{a0}A(\omega_{ge})^2, \tag{3.37}$$

where L_J is the equivalent inductance of the Josephson junction, C_T is the IDT capacacitance, C_Σ is the total circuit capacitance, and G_{a0} is given by Eq. 2.47. Interestingly, the typical anharmonicity of transmon qubits is on the same order as the size of typical SAW stop-bands. Therefore, if ω_{ge} lies in the acoustic stop-band, then the ω_{ef} lies below the stop-band. The relatively fast decay of the $|f\rangle$ state into propagating phonon modes state reduces leakage out of the $|g\rangle - |e\rangle$ manifold and could be used for unconditional resets.

Interactions with the modes at the edge of the mirror stop-band generates a rich array of phenomenon. When the qubit is inside the mirror stop band but near the edge, it creates localized phononic modes inside the band gap. If the localized phonon modes between two qubits overlap,

they will exchange energy through virtual phonons, emulating interacting spins with a distance-dependent interaction that, as the characteristic decay length depends strongly on detuning from the band edge, can easily be tuned in-situ [62, 113]. Such systems have been explored using trapped atoms and transmon qubits near a photonic stop-bands. Implementing such systems with SAWs is promising as it would avoid the difficulties of trapping atoms and strongly coupling them to a waveguide as well as the awkwardly long structures needed to create microwave photonic stop-bands [114].

Chapter 4

Strong Multi-mode Coupling in Quantum Acoustodynamics

In this chapter, I will present results from a device demonstrating that surface acoustic wave cavities can indeed be integrated with superconducting qubits. I describe how these two systems can interact strongly enough for their coupling rate to exceed the dissipation rates in the system. Moreover, the interaction rate can also exceed the cavity free spectral range, meaning that phonons and qubit excitations are exchanged faster than a single cavity round trip time. Together, these results show that surface acoustic waves cavities can realize an acoustic analog of circuit QED but with access to large delays that can be used to create multi-mode cavities and frequency-sensitive qubit-phonon interactions.

4.1 Device Design

The device consists of a transmon qubit positioned in a multi-mode SAW cavity on a GaAs substrate, as depicted in Fig. 4.1. The qubit is formed by a SQUID loop shunted by an IDT, which serves both as its capacitance and coupler to surface acoustic waves. The multi-mode acoustic cavity is defined by two Bragg reflectors made of open aluminum stripes. The cavity is driven and measured using a second IDT also positioned inside the cavity that is connected to a coplanar waveguide which carries microwave signals to and from the device. As the acoustic structures are periodic in nature, the number of parameters needed to describe the device is relatively small.

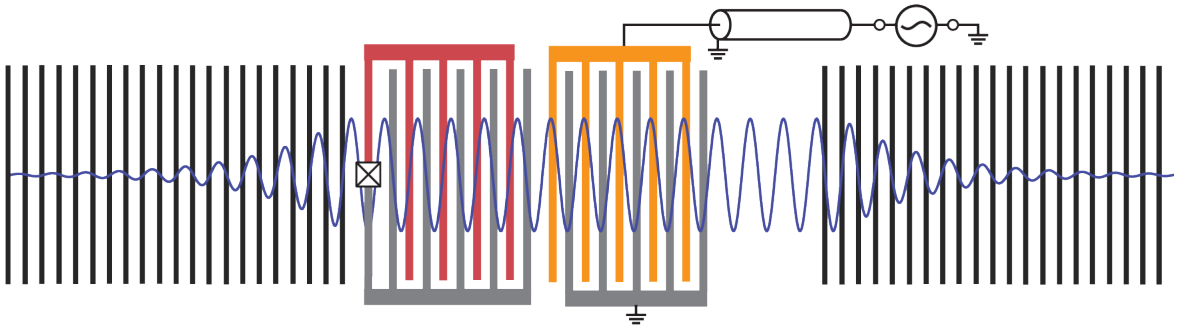

Figure 4.1: Two Bragg mirrors confined SAWs into a cavity. An IDT shunted by a Josephson junction couples to those standing waves, forming an acoustically-coupled transmon qubit (red). The system is driven and measured through a second IDT (yellow) coupled to a transmission line.

4.1.1 Acoustic Cavity Design

The SAW cavity design is characterized by its center frequency ω_c, mirror-to-mirror length L, transverse width W, number of periods in the measurement IDT N_e, and reflectivity per element of the Bragg mirrors r_s. The acoustic cavity center frequency is designed to lie in the standard 4-8 GHz band typical of most cryogenic superconducting circuit measurements. In addition to compatibility with the microwave architecture built in our laboratory, this frequency range is comfortable for transmon qubits to operate. Additionally, a dilution refrigerators can cool these high frequency mechanical oscillators into their quantum ground state. Fabrication considerations focus the design goal on the lower end of this band despite an effectively higher thermal occupation; on GaAs, surface acoustic waves travel at about 2880 m/s, so a 4 GHz wave has a length of 700 nm. At this wavelength the fingers of a split-electrode IDTs, used to improve performance through suppressed reflections [Sec. 2.2.4.3], have widths of $\lambda/8 \approx 90$ nm. These fine features are at the edge of what is achievable with university-grade electron beam lithography. All of the acoustic structures, including both IDT and mirror, are designed to have a center frequency at $\omega_c = 2\pi \times 4.25$ GHz, corresponding to $\lambda_c = 675$ nm.

The reflectivity per element of the mirrors is heavily constrained in this design. For SAW

systems in general, r_s is kept below 3% to suppress scattering to bulk acoustic modes. Additionally, the IDTs and the mirrors are fabricated in the same lithography step for simplicity, and so the ideal film thickness for the IDTs also sets the thickness of the metal grooves in the mirrors. The IDTs must have good electrical performance, which means the aluminum must be greater than 20 nm, while thicker metal will create more scattering from the IDTs in the cavity even with a split-electrode IDT design. Therefore, a thickness of 30 nm is chosen. With 50% metallization in the mirrors, this gives a reflectivity per element of $r_s \approx 2\%$ and a mirror bandwidth of 55 MHz. There are 400 metal stripes in each mirror so that transmission through the mirrors is a negligible source of loss across nearly all of the mirror bandwidth.

The length of the cavity is chosen so that approximately 10 modes are supported within the mirror bandwidth. As the mirrors have a 55 MHz bandwidth, the free spectral range should be $\omega_s = 2\pi \times c/(2L_e) \approx 2\pi \times 5$ MHz corresponding to a cavity length of 300 µm. The effective cavity length L_e is given by the spacing between the mirrors plus twice the SAW penetration length $L_e = L + 2L_p$ where $L_p = \lambda_c/(4r_s)$ ≈12 µm. The chosen mirror-to-mirror length L =275 µm accounts for this effective length increase.

The transverse dimension of the cavity would be hundreds of wavelengths wide if the only concern were the quality factor of the cavity. Wider cavities lose less energy to diffraction, following Eq. 2.33. However, as discussed in the next section, the cavity width plays a role in determining the transmon qubits charging energy. Therefore, a narrow transverse dimension was chosen that limited the acoustic internal loss rate to $\kappa_d \approx 2\pi \times 100$ kHz.

Lastly, an IDT placed inside the cavity and connected to a transmission line enables drive and measurement of the acoustics with microwave signals. The number of electrode periods in this IDT is chosen to achieve an external coupling rate that exceeds the diffraction limited loss rate. With $N_e = 100$, the bare external coupling rate should be $\kappa_{e,0} \approx 2\pi \times 230$ kHz with a bandwidth of $\omega_0/N_e \approx 2\pi \times 40$ MHz. This IDT is placed near the center of the cavity where the spatial structure of the many SAW resonances can be well approximated by only two standing wave profiles having either even or odd symmetry [Fig. 4.3]. The placement of the IDT relative to these two profiles

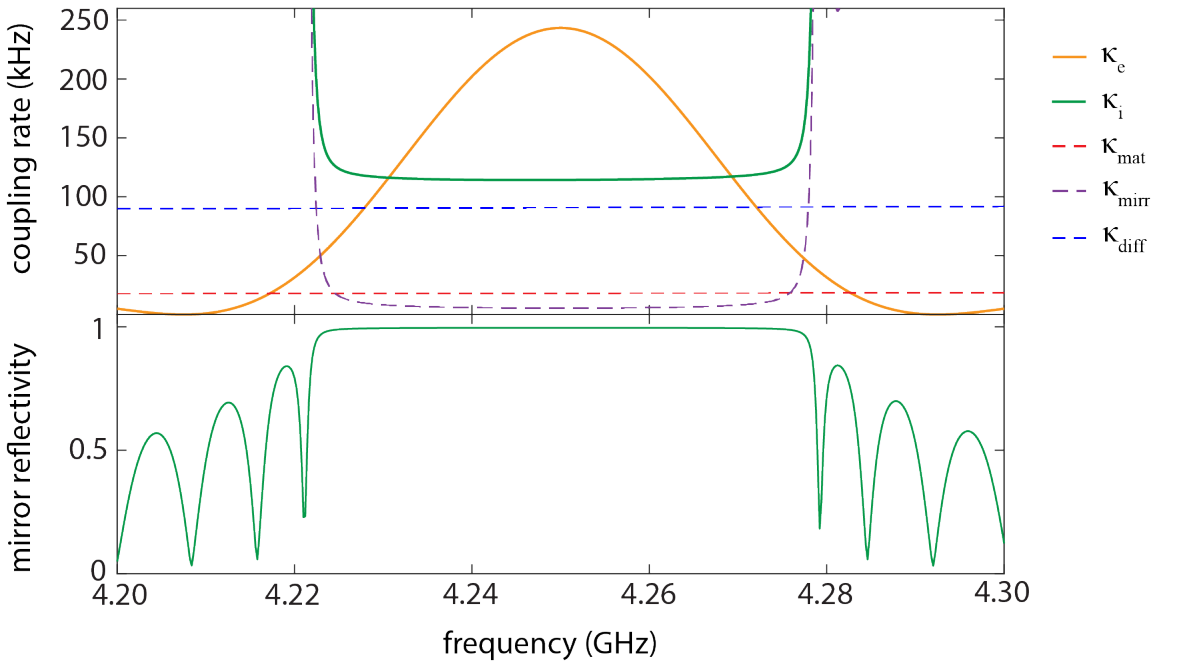

Figure 4.2: The acoustic cavity is designed to have an external coupling rate that exceeds internal loss over most of the mirror bandwidth. The cavity loss rate is dominated by diffraction until propagation through the mirrors takes over at the edge of the mirror bandwidth. Material loss assumes a $Q \cdot f_0$ product of 10^{15}, and the mirror contribution assumes a loss-per-wavelength of 10^{-3} for propagation inside the mirrors, which limits the mirror reflection to 99.6% at the center of the mirror bandwidth.

determines its external coupling rate; if the IDT was exactly centered, then it would couple only to odd modes (as IDTs with a whole number of periods have odd symmetry about their center). The fabrication constraints described in the next section limit the position resolution of the IDT placement to a precision of about ~ 400 nm $\approx \lambda/2$. This placement error is large enough that a design cannot intentionally couple preferentially to even or odd modes.

The measurement IDT is connected to a coplanar waveguide (CPW) leading to the drive line and amplification chain. The waveguide has finite extent ground electrodes as they are written with electron beam lithography where exposing a large area becomes prohibitively time intensive. Ideally, the IDT would shunt the center conductor to both ground electrodes. However, to avoid extraneous aluminum leads inside the acoustic cavity, the IDT connects the CPW center to ground

only on one side, with half of the acoustic cavity located in a gap formed by increasing the spacing between the center conductor and ground [Fig. 4.6(a)]. The CPW was designed to be near 50 Ω on GaAs, with a center conductor of 60 um, a gap of 40 um of GaAs with a relative dielectric constant of 12.5. In hindsight, the finite width of the ground electrodes (100 µm) combined with the significant kinetic inductance fraction of the 30 nm aluminum film (near 40%) [115], means the impedance of the line was likely between 65 Ω and 75 Ω.

4.1.2 Transmon Qubit Design

An attractive aspect of the transmon qubit is its simplicity: it is defined by only its charging energy, E_C, its Josephson energy E_J, as well as by how strongly it interacts with the system of interest, here confined acoustic modes [Sec. 3.3.4]. Typically, transmon qubits have $E_J/E_C \gg 50$, and so several hundred MHz of anharmonicity. Here, E_C is designed to be 230 MHz, which sets the overall capacitance of the transmon qubit to be 80 fF. This total capacitance then constrains the product of the cavity width and the number of qubit IDT finger periods N_q. The number of IDT finger periods should be much larger than one to suppress unwanted excitation of bulk waves; here, $N_q = 20$. Combined with the capacitance per unit length of IDTs on GaAs of 120 pF/m [81], this sets the IDT and cavity width to be 25 µm.

Using a DC SQUID allows E_J to be decreased by applying an external magnetic field. In order to create resonant interactions between the qubit and the acoustic cavity resonances at ω_c, the bare resonant frequency ω_0 is designed to be about 20% above the acoustic band at $\omega_0 \approx 2\pi \times 5$ GHz. This corresponds to a bare Josephson energy of $E_J = 12.5$ GHz. The SQUID loop has an area of 49 µm^2 [Fig. 4.6(d)] with a mutual inductance to an off-chip superconducting coil such that 1 mA of current in the coil corresponds to approximately 1 flux quantum in the SQUID loop.

The transmon IDT is positioned in the cavity at a distance of approximately $L/4$ from one mirror. Its coupling is determined by Eq. 3.35, with overall strength $g_0 \approx 2\pi \times 6.5$ MHz that changes from one acoustic mode to another based on the modes frequency and its spatial overlap with the IDT. As the qubit IDT has only $N_q = 20$ finger periods, its bandwidth of 200 MHz is

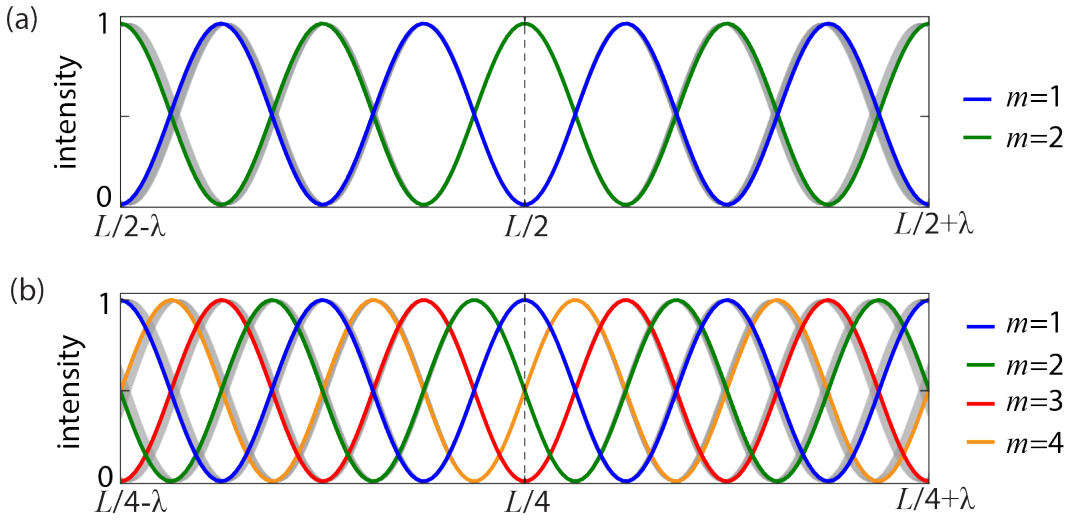

Figure 4.3: The measurement and qubit IDTs are placed at (a) $L/2$ and (b) $L/4$ in the cavity, respectively. At these high-symmetry points, many cavity standing waves are closely aligned. This symmetry degrades away from these points, shown by the spread in the standing waves modes (gray).

large compared to the mirror bandwidth, so its frequency sensitivity can safely be ignored. The $L/4$ point in the cavity, though not as high symmetry as the cavity center, still simplifies the mode-dependence of the coupling rate [Fig. 4.3(b)]. As increasing the mode index by one means the wave must pick up an additional π phase over the cavity length L, then the wave must pick up a phase of $\pi/4$ by length $L/4$, so that the standing wave amplitudes follow,

$$g_m = g_0 \sin\left(m\frac{\pi}{4} + \phi_q\right), \tag{4.1}$$

where ϕ_q accounts for a small displacement from $L/4$ introduced by fabrication uncertainty.

There are two obvious traits of this transmon design that will significantly reduce its coherence times compared to the state-of-the-art. First, the piezoelectric substrate required to couple the transmon to the acoustic cavity will also allow it to couple strongly to the dense spectrum of phononic modes supported by the chip. This same effect limits coplanar waveguide resonators fabricated on GaAs to quality factors of several few thousand [116]. The IDT structure does preferentially couple the transmon to the quasi-1D surface acoustic waves of interest, but phonon

radiation to other modes will still contribute a significant amount of loss.

Second, the fine pitch of the capacitor stores a high density of electric field energy at the surface of the dielectric. Interfaces between different materials host impurities, such as defects, oxides, organic residues, and adsorbed water, that lead to a substantially higher loss tangent at interfaces than for bulk dielectrics. A study of transmon qubits made from evaporated aluminum on sapphire, a common process for fabricating transmon qubits, approximated the dielectric loss tangent at the metal-surface interface to be $\tan(\delta) \approx 2.6 \times 10^{-3}$ by assuming the interface to be 3 nm thick with relative dielectric constant of 10 [117]. With these assumptions, a 10 micron pitch capacitor leads to a 0.1% participation ratio and surface limited quality factor $Q_s \approx 4 \times 10^5$. For the $\lambda_c/4 \approx 180$ nm pitch capacitors used here [Fig. 4.6(c)], the participation of the interface is 6%, limiting the quality factor to $Q_s \approx 6 \times 10^3$, or a linewidth of 600 kHz at 4 GHz. This is a significant loss channel, and is likely optimistic as it is extrapolated from transmons fabricated on a sapphire substrate, which almost surely outperforms GaAs. Together, unwanted phonon radiation and significant participation of the surface constitute major limits on the potential performance of transmon qubits coupled to GHz surface acoustic wave cavities.

4.1.3 Device Fabrication

The device is fabricated on a chip of GaAs using electron beam lithography as standard optical lithography does not have the resolution to pattern the required fine pitch transducers or small critical current junctions. After cleaving 6.2 mm square chips from a (001)-oriented wafer of epitaxial GaAs, the chips were submersed in ammonium hyrdoxide for 300 s to strip the surface oxide layer, then sonicated in standard solvents. Note that GaAs cleaves along the (011) plane, which is parallel to the direction that supports clean Rayleigh wave modes.

After this simple cleaning procedure, three metal layers were patterned all using metal evaporation and lift-off processes. The active parts of the device are composed of aluminum, but multiple layers are required because the Josephson junctions and acoustic structures have incompatible requirements: the junctions require a resist bridge to be formed between two lines several hundred

nm apart, as described shortly, while the IDTs, also consisting of several lines separated by about 100 nm, would fail if the resist formed bridges. This incompatibility then requires two separate lithography steps which must be aligned to better than a micron. This alignment is achieved using a third layer containing alignment markers. Gold is an ideal marker material because it is a common microfabrication material, and it reflects incident high energy electrons in the electron beam writer much more strongly than GaAs due to its larger atomic number: gold nuclei have 79 protons compared to gallium's 31 or arsenic's 33.

The gold marker layer is deposited first using a stack of 400 nm MMA under 200 nm PMMA. Both resists are sensitive to incident and electrons, and will develop away in a mixture of MIBK/IPA if the electron beam deposits a sufficient amount of energy. Crucially, MMA is more sensitive than PMMA. This elevated sensitivity combined with the spread and back-scatter of the electron beam enlarges the developed area in the MMA compared to the PMMA, creating an undercut [Fig. 4.4(a-b)]. The mark pattern is exposed in an SEM reconfigured as an ebeam writer, controlled using NPGS software. After exposure, the resist is developed and 100 nm of gold is deposited, with 10 nm of titanium underneath to promote adhesion. The unwanted titanium and gold film sitting on unexposed resist are lifted off in acetone.

Next, the aluminum layer containing everything except the Josephson junctions is deposited using a single layer of 200 nm PMMA. Each acoustic structure was aligned to a separate marker pattern using the SEM, then exposed, developed in MIBK/IPA, and cleaned using a weak oxygen plasma, before 30 nm of aluminum is deposited. This aluminum was oxidized in the chamber to promote a well-controlled and reproducible oxide layer, before lift-off in warm (40° C) acetone for at least 30 minutes. Lift-off of fine features without a bilayer is difficult. With the 30 kV beam used, an undercut still forms even in just PMMA. For good lift-off, it was crucial to have the gap between the ends of the fingers and the bus bar to match the separation of the fingers. We believe the metal between fingers lifts off like the peeling of a sticker, and having a uniform width helped significantly. Sonication was often required to remove tenacious but unwanted metal. The back-scattering of electrons effects an area much larger than the radius of the electron beam, and

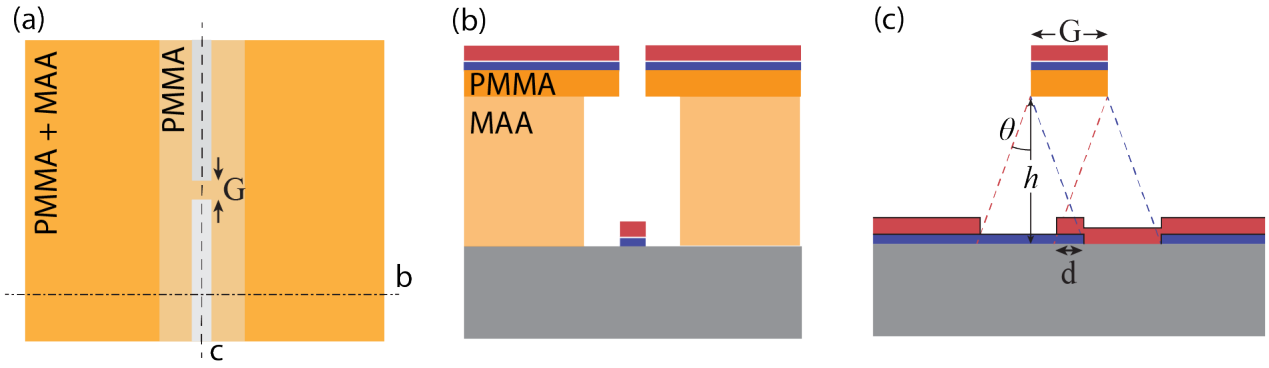

Figure 4.4: (a) The bilayer of resist creates an undercut and bridges as the bottom layer (MAA) is more sensitive to than the top layer (PMMA). Horizontal (b) and vertical (c) linecuts show the undercut and bridging used for lift-off generally and Dolan-bridge Josephson junctions in particular.

the applied dose must be adjusted for the density of features in close proximity. This adjustment is crucial for successful lithography of the fine IDT electrodes and was implemented by segmenting the design into several sections with a dose compensation determined iteratively.

Lastly, the junction layer is deposited using the same resist stack, exposure, and development as the marker layer. After development, a brief, weak oxygen plasma is performed to clean resist residue from the substrate. The evaporation for the junctions involves two angle depositions at $\pm 20^\circ$ separated by a several minute oxidation period, where a small amount of O_2 ($\sim$ 1 mbar) is introduced to the deposition chamber. The junction geometry is shown in Fig. 4.4, where a discontinuity of length G creates a overlap length $d = 2h\tanh(\theta) - 2G$ where θ is the evaporation angle and h is the height of the resist. The length and pressure of the oxidation set the thickness of the insulating barrier, and combine with the junction geometry to determine the junction critical current.

The junction critical current can be inferred using room temperature resistance measurements. The Ambegaokar-Baratoff relation provides a direct relation between the metals superconducting gap Δ, the critical current I_C, and the normal resistance from electrons tunning across the junction R_N, [118]

$$I_c = \frac{\pi\Delta}{2eR_N}, \tag{4.2}$$

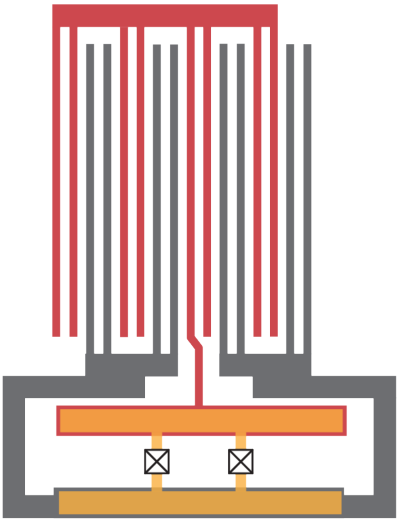

Figure 4.5: The Josephson junctions are connected capacitively to the IDT using a large ($50\,\mu m^2$) overlap between the two layers. A single electrode is pulled through the bottom bus bar, which allows the junctions to shunt the IDT while being placed outside the acoustic beam.

for $k_B T \ll \Delta$. For this device, $E_J = 12.5$ GHz corresponds to $I_C = 32$ nA and $R_N = 4$ kΩ. While the critical current of a junction can be estimated coarsely from geometry and oxidization parameters, in practice, an array of test junctions are fabricated and measured, varying the oxidation time and measuring iteratively to hone in on the design value of the normal resistance.

In this design, there is no galvanic connection between the qubit IDT and the Josephson junctions. The aluminum in the qubit IDT is exposed to atmosphere after deposition and during the junction processing, and therefore an insulating aluminum oxide layer forms on its surface. Instead of a galvanic connection, a large overlap is designed between the two layers, which creates strong capacitive connection [Fig. 4.5]; the overlap area of $50\,\mu m^2$ and an oxide thickness of 5 nm with a relative dielectric constant of $\epsilon_r = 10$ gives a capacitance of 1 pF. At 4 GHz, this capacitance is 3 Ω, sufficiently small compared to the transmon impedance of 400 Ω to be considered a good short. However, this oxide layer has been exposed to atmosphere and is therefore likely to contain defects, water vapor, resist residue, and other contamination that will adversely impact the qubit coherence.

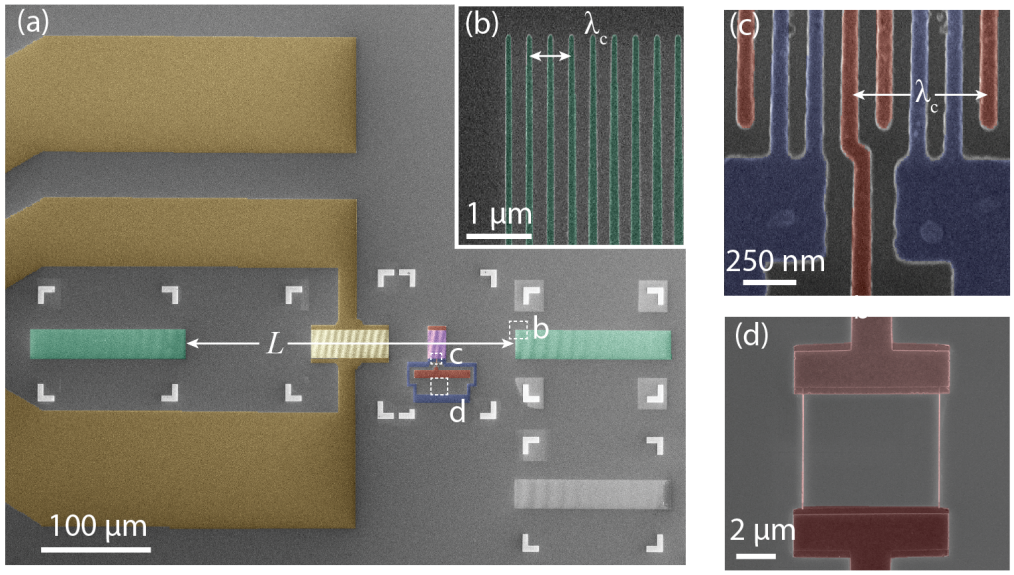

Figure 4.6: (a) False-color SEM image of the device, showing aluminum on GaAs with gold alignment marks. An acoustic cavity is formed by two Bragg reflectors (green) and contains both a transmon qubit (red and blue) as well as a measurement IDT (yellow). The measurement IDT connects the center conductor of a CPW to ground. Insets show higher magnification images of the (b) mirror elements, (c) qubit IDT, and (d) Josephson junctions, the last of which was deposited after the full image was acquired.

At the magnification required to write the small features, the SEM has a writing field of 150 µm per side. As this window is much smaller than the device, the SEM stage has to move the sample to expose the full pattern. This stage movement introduces significant positioning errors on the order of ±1 µm. Each structure (measurement IDT, each mirror, etc...) is written in a separate writing field and referenced to the gold marker layer. As the marker layer was also written in the same SEM and required the same stage movement, there is the same relative uncertainty between each writing window. However, as both the acoustic and junction layers are referenced to the same gold markers, the position error between these two layers is reduced to well below 100 nm.

4.2 Device Measurement

The device is characterized using microwave reflection from the measurement IDT at the base temperature of a dilution refrigerator. At these temperatures (20 mK), both the transmon

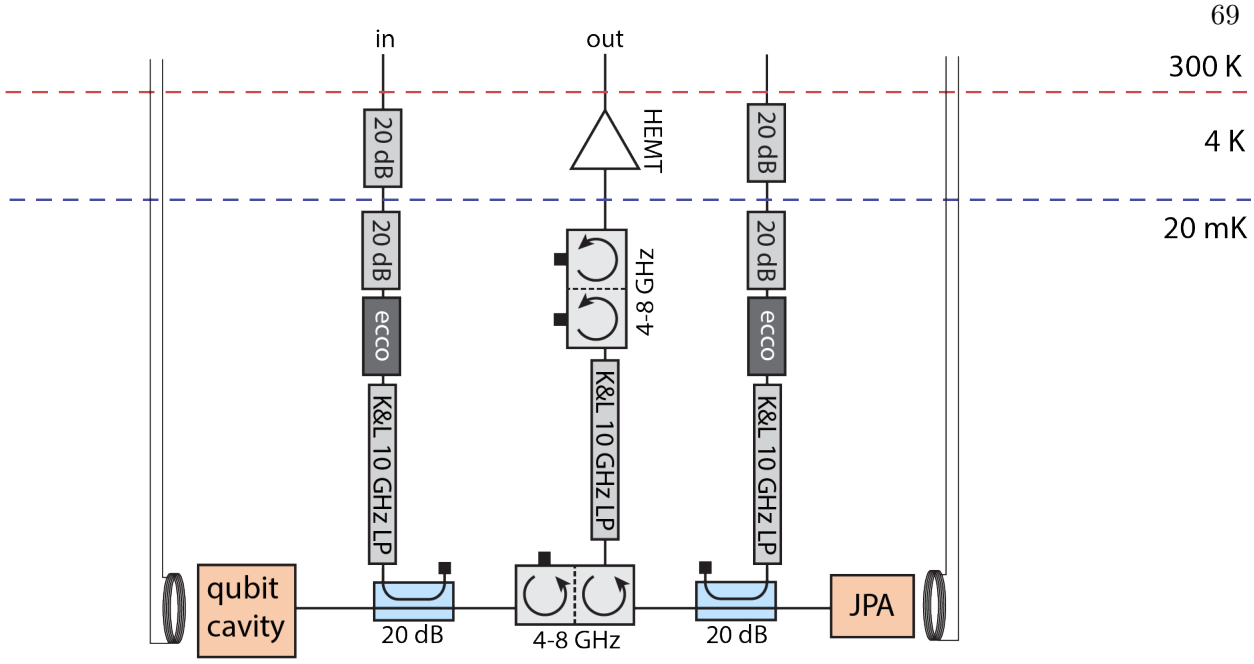

Figure 4.7: The acoustic cavity is measured in reflection at the base of a dilution refrigerator. A Josephson parametric amplifier (JPA) either provides 25 dB of narrow-band gain or acts as an open, losslessly reflecting incident signals. Off-chip magnetic coils provide uniform magnetic flux to tune the resonant frequencies of the qubit and the JPA.

qubit and the acoustic modes of the cavity are passively cooled to their quantum ground state. The reflected microwave signals carry information about the acoustic resonances and their interaction with the transmon qubit. This section will describe the various microwave measurements that demonstrate that the device is well described by multi-mode Jaynes-Cummings physics with a "giant atom," far from the dipole approximation.

4.2.1 Acoustic Response

The acoustic spectrum is measured in reflection using a directional coupler [Fig. 4.7] with the qubit tuned off resonance. Over the 55 MHz mirror bandwidth, there are 11 prominent resonances spaced by approximately $\omega_s \approx 2\pi \times 4.8$ MHz [Fig. 4.8]. The magnitude of reflection changes significantly on resonance, indicating that the acoustic modes are near critically coupled. Three modes have full 2π wraps in phase across their resonances and therefore are slightly over-coupled.

We are unable to determine the absolute index of each mode, and instead begin enumeration of the modes at the first visible resonance, which corresponds to approximately the 880th longitudinal mode of the resonator. There is a clear alternating pattern in the external coupling strength of the resonant modes, with the odd modes being more strongly coupled than the even. This is because, in the center of the cavity, the standing wave moves by $\pi/2$ phase with each increased mode, and the external coupling rate is proportional to the intensity of the wave at the IDT [Fig. 4.3(a)].

The resonances become more under-coupled near the top and bottom of the acoustic band. There are two effects that contribute: the measurement IDT is less sensitive to these frequencies and the mirrors are slightly less reflective. The large number of fingers in the IDT gives it a bandwidth of 40 MHz which reduces the external coupling rate to the outer modes. At the center of the IDT bandwidth, this corresponds to a coupling rate of about 100 kHz, but this decreases quickly away from its center frequency. The acoustic modes have internal linewidths that are comparable to this at the center of the mirror bandwidth, which matches the diffraction limited loss calculated earlier. However, near the edge of the mirror bandwidth, phonons penetrate further into the mirrors, resulting in increased loss both from propagation all the way through the mirrors as well as increased time spent trapped in the lossy mirror region. The combination of decreasing external coupling and increasing internal loss, shown in Fig. 4.8, significantly decreases the visibility of modes near the edge of the acoustic bandwidth.

In addition to the 11 prominent resonances, the spectrum shows at least six additional modes on the high-frequency shoulders of every other prominent resonance. These modes have about three times the internal loss and about one eighth the external coupling rate, dramatically reducing their visibility. These spurious modes are most likely transverse modes that have two nodes along the transverse direction of the cavity. Although there is little transverse confinement in the cavities, there are slight velocity differences along the transverse direction associated with the mirrors and the IDT bus bars which nonetheless provide sufficient confinement to produce visible resonances [83]. The frequencies of these tranvserse modes $\omega_{m,t}$ can be estimated by considering the cavity as

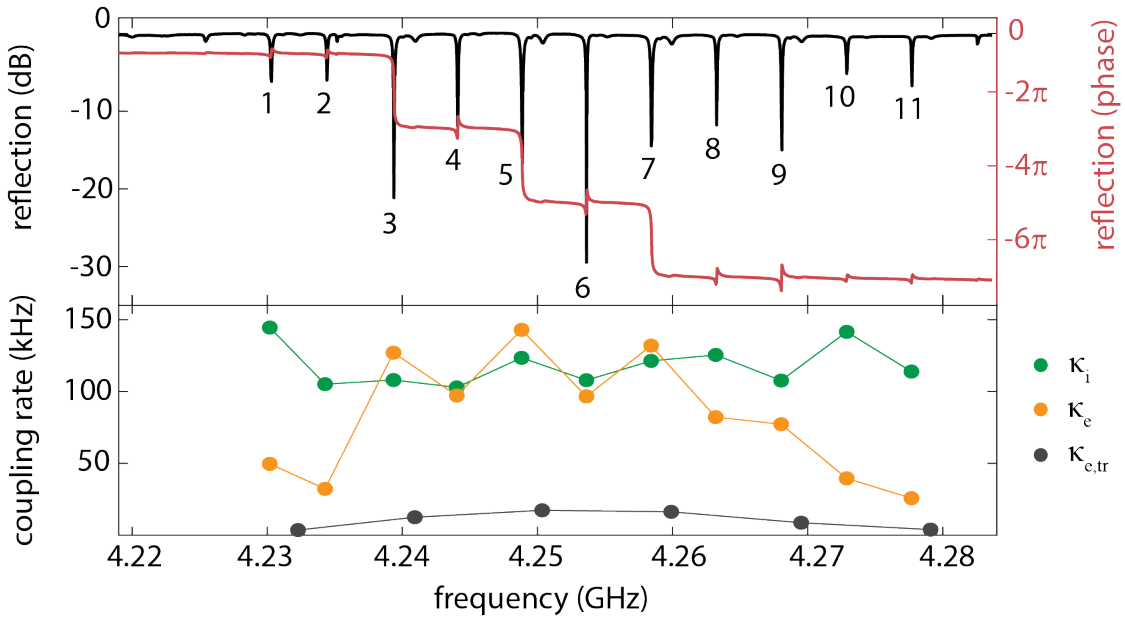

Figure 4.8: Reflection from the acoustic cavity with the qubit detuned shows 11 prominent resonances in a 50 MHz span. The main resonances are nearly critically coupled, as shown by the extracted coupling rates, and are accompanied by transverse modes on the high-frequency shoulder.

a rectangular waveguide with the same velocity in all directions,

$$\omega_{m,t} \approx 2\pi \times v_s \sqrt{\frac{m^2}{4L_e^2} + \frac{t^2}{4W^2}}, \tag{4.3}$$

where m is the longitudinal mode number and t is the transverse mode number. For the cavity with of 25 µm, $t = 1$ corresponds to tranverse modes about 0.4 MHz above and $t = 2$ modes about 1.7 MHz above. By symmetry, the odd order transverse modes do not couple strongly to the even-symmetry IDTs. The prediction for $t = 2$ approximately matches the measured transverse mode spacing of ~ 1.5 MHz.

4.2.2 Resonant Interaction

After characterizing the uncoupled acoustic resonances, we investigate their resonant interaction with the transmon qubit by tuning it through the acoustic bandwidth with an applied magnetic flux while monitoring reflection with a low power probe tone. Two sets of avoided crossings are

visible as the magnetic field is swept over one flux quantum, as shown in Fig. 4.9. Several features of the system are immediately apparent from the measured interaction. First, the clarity and size of the avoided crossings indicates that the qubit and cavity exchange energy coherently and at a rate comparable to the spacing between resonant modes. Second, the qubit interacts with different modes with different strengths: indeed, there are three acoustic modes that barely couple to the qubit at all, as shown by their small avoided crossings. Lastly, although the uncoupled modes all interact relatively equally with the measurement IDT, the external coupling rates of the hybridized modes vary dramatically; half of the modes become dark, no longer coupling to the measurement IDT, while the other half remain bright.

The prominent features of the measured avoided crossings can be accurately described by a simple model despite their apparent complexity. As described earlier in Eq. 4.1, the qubit-cavity coupling rates can be described by a simple 2-parameter model accounting for an overall coupling strength and an offset accounting for an offset from $L/4$ of the cavity. The transverse modes must also be included, as they clearly participate in the avoided crossings. The frequencies of the transverse modes can be determined from the acoustic spectrum with the qubit detuned, while the qubit-transverse resonance interaction strength is extrapolated from how the longitudinal and transverse modes interact with the measurement IDT: from the measured external coupling rate, the measurement IDT has a 2.8 times stronger spatial overlap with the transverse modes, and so the same factor is assumed for the qubit-transverse mode interaction strength.

Using these simplifications and measurements of the acoustic resonant frequencies with the qubit detuned, the interaction Hamiltonian between the qubit and the 17 acoustic modes of interest can be described by just three parameters: g_0, ϕ_q, and a fine offset in the flux-dependence of the qubit frequency. In the low-power limit, where on average there is below a single excitation in the

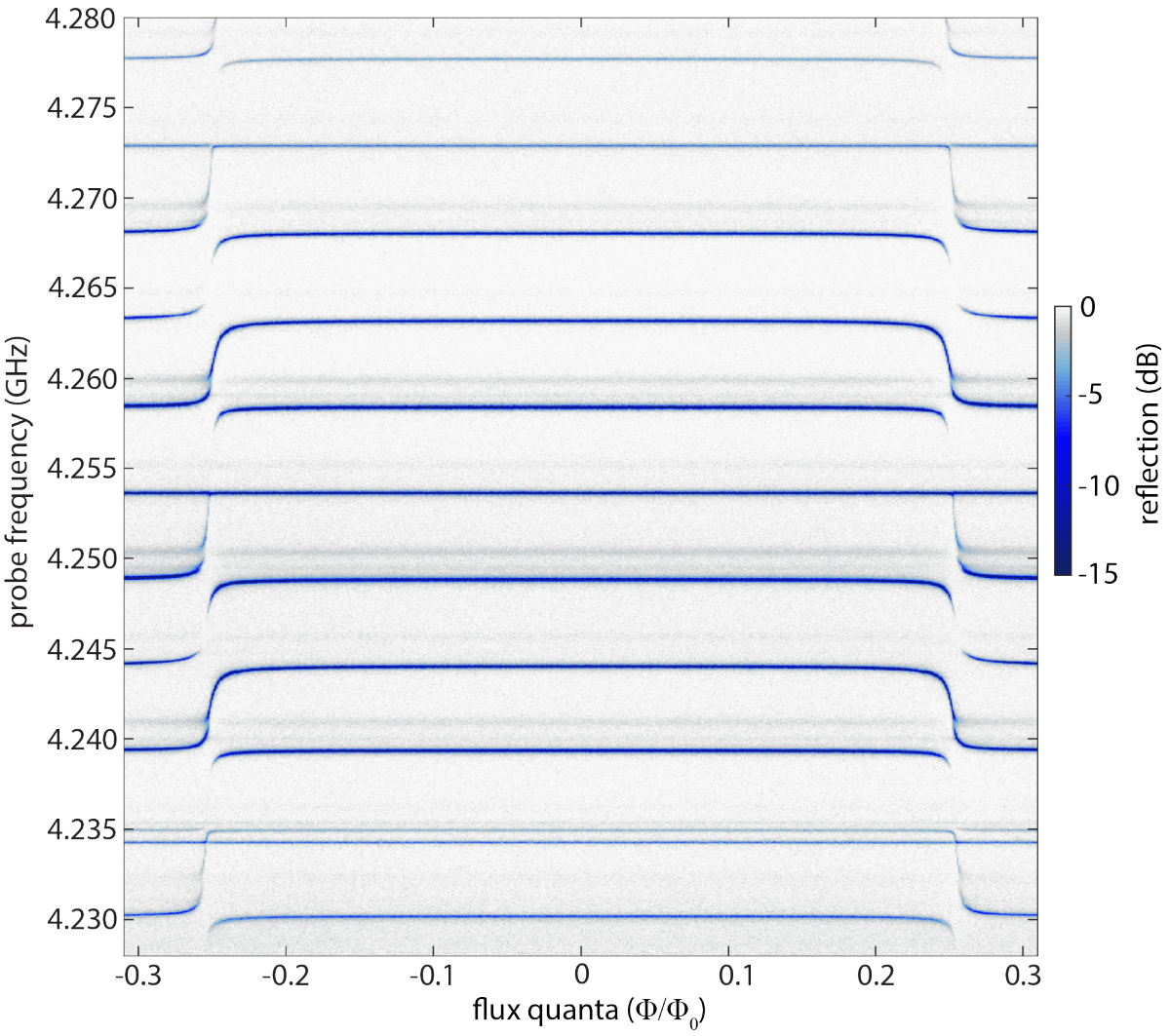

Figure 4.9: Applying a magnetic flux tunes the qubit across the acoustic modes. Clear avoided crossings are observed at $\pm 0.26\Phi/\Phi_0$ with a coupling strength on the same scale as the mode spacing.

system, the Hamiltonian has the form,

$$H/\hbar = \begin{pmatrix} \omega_1 & & & g_1 \\ & \omega_2 & & g_2 \\ & & \ddots & \vdots \\ g_1 & g_2 & \cdots & \omega_q \end{pmatrix}. \tag{4.4}$$

The eigenmodes of the system at each ω_q can be determined by diagonalizing the Hamiltonian

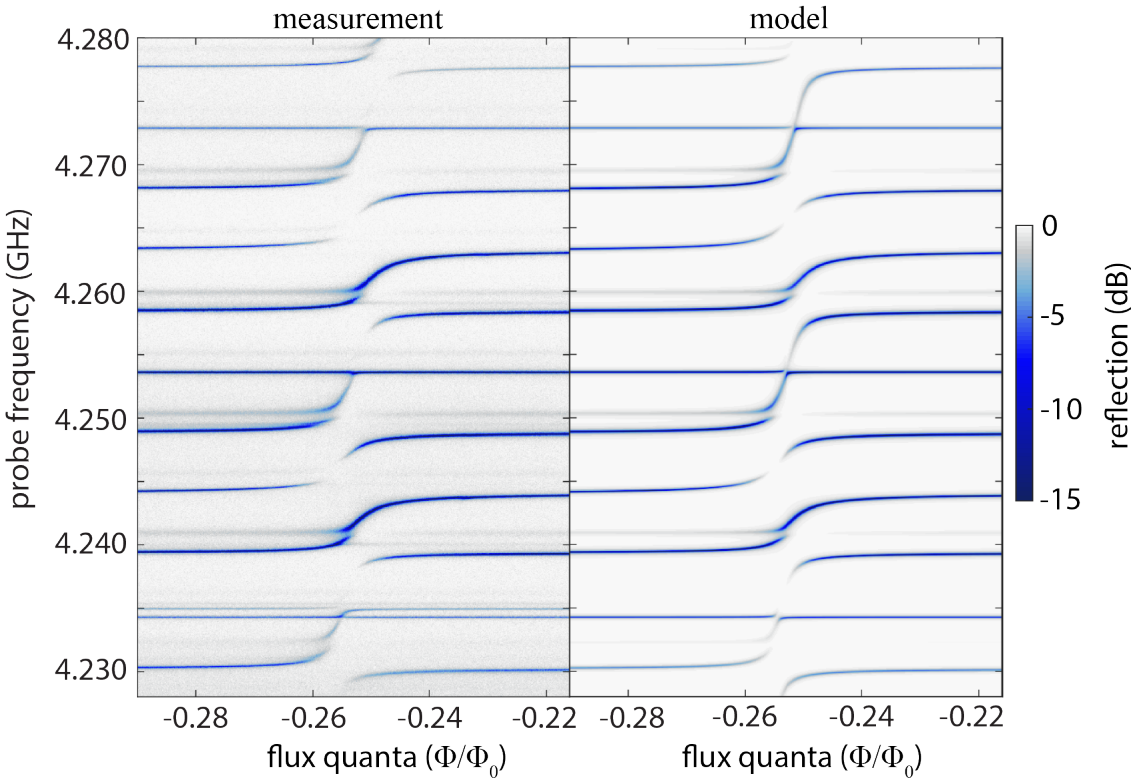

Figure 4.10: The measured acoustic response with the qubit in resonance shows complicated crossings with various strengths as well as bright and dark modes. A model describing the reflection across the crossing with 3 free parameters closely matches the measurements.

above. The best fit between the measured resonant frequencies and the eigenvalues of the model gives $g_0 = 2\pi \times 6.5$ MHz and $\phi_q = -0.1$ rad. There are two modes that achieve nearly the maximum coupling strength, with $g_{4,8} \approx 2\pi \times 6.48$, while three modes have near vanishing coupling, with $g_{2,6,10} \approx 2\pi \times 650$ kHz. The remaining modes have intermediate coupling strengths of either $g_{1,5,9} \approx 2\pi \times 4.1$ MHz or $g_{3,7,11} \approx 2\pi \times 5.0$ MHz.

The microwave reflection from the cavity can be reconstructed by modelling the internal and external coupling rates of the cavity in addition to the eigenvalues. The model presented here replicates the measured acoustic response well for all acoustic modes and all flux points, as shown in Fig. 4.10. The model requires not just the eigenvalues, but also the eigenmodes of the system.

These eigenmodes $|\psi'_m\rangle$ are superpositons of the uncoupled modes $|\psi_n\rangle$,

$$|\psi'_m\rangle = \sum_n c_{n,m}|\psi_n\rangle, \tag{4.5}$$

where $c_{n,m}$ are found by diagonalizing the Hamiltonian, and the sum of their squares is one, i.e. $\sum_n c_{n,m}^2 = 1$. The internal loss rates of the hybridized modes are a sum of the loss rates of each participating mode weighted by its weight in the eigenmode,

$$\kappa'_{i,m} = \sum_{n=1}^{18} c_{n,m}^2 \kappa_{i,n}, \tag{4.6}$$

where $\kappa_{i,18} = \gamma$ is the qubit linewidth. As the new loss rate is just a weighted average of the uncoupled modes and as most modes have similar internal linewidths, the overall loss rates of the coupled modes closely approximates the uncoupled ones.

The external coupling rate must be considered differently from these internal channels because there can be coherent interference between external coupling from different modes. Intuitively, the eigenmodes of the system correspond to some hybridization of the acoustic cavity modes plus some qubit participation. Spatially, these eigenmodes are superpositons of cavity standing waves, which have distinct spatial profiles that can have significantly different overlap with the measurement IDT. Mathematically, these external coupling rates are,

$$\kappa'_{e,m} = \kappa_0 \left| \sum_{n=1}^{17} c_{n,m} \sin(n\pi/2 + \phi_i) A(\omega_n) \right|^2, \tag{4.7}$$

where κ_0 is scale of the external coupling rate of the cavity, $A(\omega)$ is the frequency dependence of the IDT [Eq. 2.44], and the sine term describes the amplitude of the SAW at the IDT of mode n, which is near $L_e/2$ but with offset phase $\phi_i \approx \pi/4$. Near resonance the hybridized modes are mostly composed of two neighboring acoustic modes, each with approximately equal external coupling magnitude, but with a sign that flips every other mode, thus creating an alternating bright-dark mode pattern in the measured cavity response.

The defining characteristic of the strong, multi-mode coupling regime is that the eigenmodes of the system are composed of many uncoupled modes. If $|g_m| \ll \omega_s$, then the avoided crossings will be pairwise, with the qubit hybridizing with only one mode at a time. Here, even though

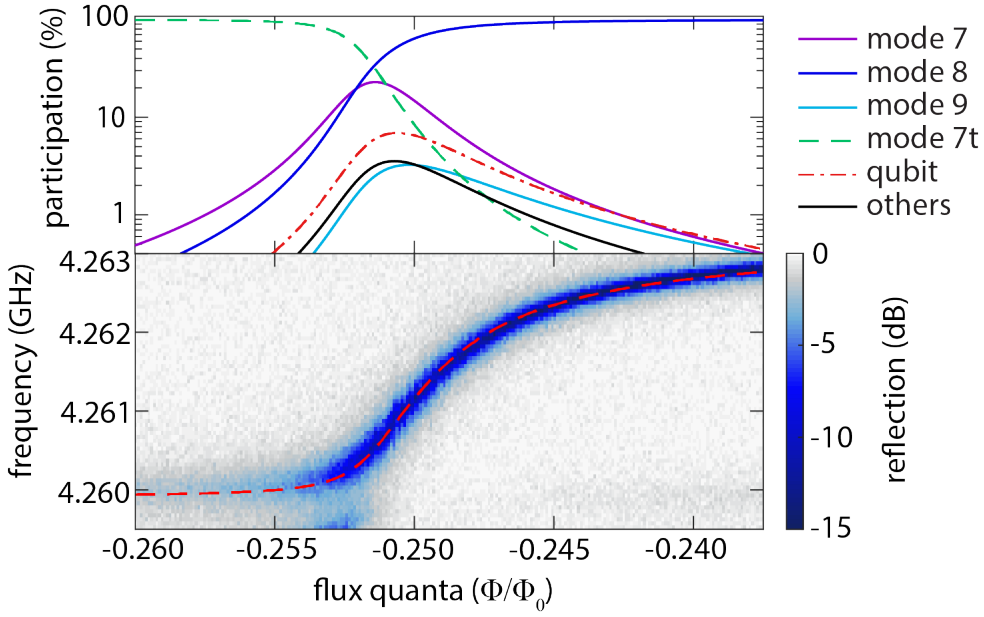

Figure 4.11: Focusing on one eigenmode shows that, with the qubit on resonance, there is a significant contributions from a large number of the uncoupled modes. The eigenmode shown here is composed primarily of three neighboring acoustic modes; the qubit participates only weakly, below 7%, across the whole crossing. The predicted frequency closely matches the measurement (dashed).

g_m depends strongly on the mode index, the avoided crossings are far from pairwise between the qubit and individual cavity modes. As shown in Fig. 4.11, many modes participate in the avoided crossing. Interestingly, the qubit participation remains small over the flux range near the center of the acoustic band because the qubit participates in many eigenmodes at a given flux. Essentially, the qubit mediates strong coupling between neighboring acoustic modes. This effect also dilutes the qubit loss over many modes and implies that clear avoided crossings do not directly imply the system has exceeded the strong coupling criteria $g_m > \{\kappa_m, \gamma\}$. Indeed, the full model recreating the measured spectra is somewhat insensitive to the input qubit linewidth. Verifying the device meets the strong coupling criteria requires independent verification that the qubit linewidth is below the measured coupling strengths.

4.2.3 Qubit Measurements in the Dispersive Regime

The system can be tuned into the dispersive regime despite $g_0 > \omega_s$ because the acoustic reflectors only support resonances over a narrow bandwidth. In the dispersive regime, the acoustic resonances experience a shift dependent on the state of the qubit, and the qubit state can be determined by monitoring an acoustic resonance [Sec. 3.3.2]. The dispersive shift is largest, and readout is easiest, for the most strongly coupled resonances, and here we use $m = 8$ to read out the qubit state.

4.2.3.1 Qubit Spectroscopy

Spectroscopy of the qubit is performed by sweeping a drive tone near its resonant frequency while a second tone is reflected off the acoustic cavity near ω_8. The acoustic resonance is at $\omega_8 - \chi$ if the qubit is in the ground state and $\omega_8 + \chi$ if it is in the excited state. Changes in the qubit population from the qubit drive result in changes in reflection from the shift of the cavity frequency. The JPA is used when measuring qubit spectroscopy as its bandwidth is more than sufficient for these slow, single-frequency measurements and the improved signal-to-noise makes spectroscopy significantly faster.

Using this acoustic readout, the qubit frequency can be tracked as a function of flux up to its maximum frequency near 5 GHz. The measured qubit frequency closely follows the expected flux dependence of the SQUID inductance [Eq. 3.12] over the measured range shown in Fig. 4.12. The clean spectrum shown required significant compensation of the drive power as a function frequency, as the drive more strongly polarized the qubit at small detuning from the cavity. Driving with too much power not only broadens the qubit, but extra transitions appeared, complicating the spectrum. At very high drive powers, several two-level system defects were visible. One such two level system near 4.8 GHz showed clear Rabi and Ramsey oscillations with coherence times of order microseconds. The nature of these defects is yet undetermined, but we suspect a defect in the dirty oxide layer sandwiched between the IDT and junction aluminum films.

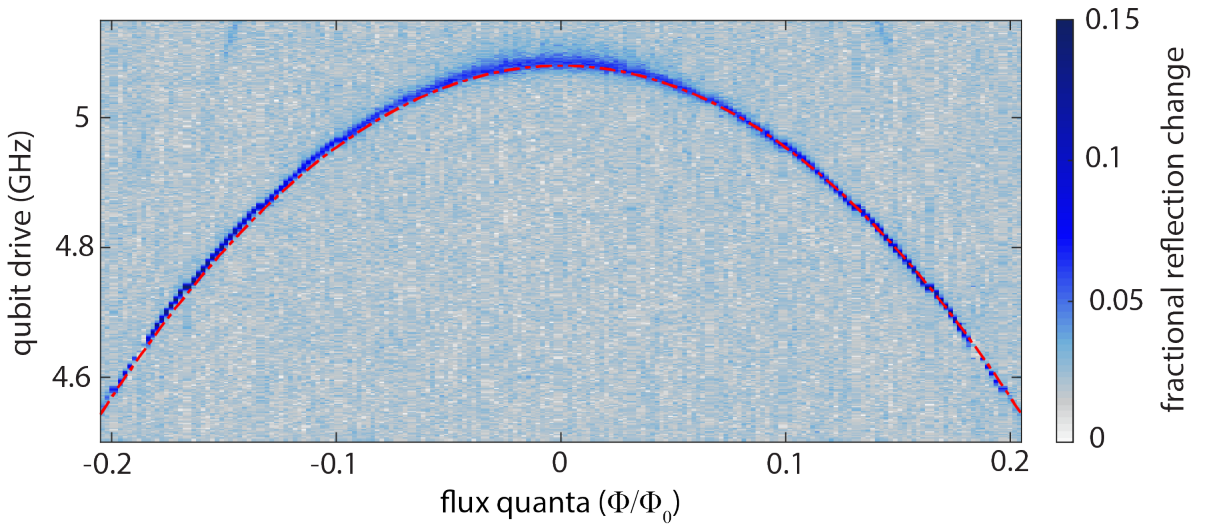

Figure 4.12: The qubit spectrum is measured by monitoring the reflection from acoustic mode $m = 8$ while sweeping a qubit drive tone. The measured qubit spectrum closely follows the predicted flux dependence (dashed).

4.2.3.2 Transmon Anharmonicity

Acoustic readout can also be used to measure the anharmonicity of the transmon. With the qubit tuned to 4.077 GHZ, just below the acoustic band, applying a strong qubit drive 20 dB above the low-power limit shows the power-broadened ω_{ge} as well as the two-photon $|g\rangle - |f\rangle$ transition at $\omega_{gf}/2 = \omega_{ge} - \alpha/2 = 3.952$, as shown in Fig. 4.13. This gives an anharmonicity of $\alpha = 2\pi \times 250$ MHz. To see the $|e\rangle - |f\rangle$ transition, there must be population in the $|e\rangle$ state. Retaking the spectroscopy with a second pump fixed at ω_{ge} indeed shows a dip at $\omega_{ef}/2\pi = 3.828$ GHz, which gives a second measurement $\alpha/2\pi = 249$ MHz. This anharmonicity corresponds to a qubit capacitance of 77 fF, within 10% of the design value of 85 fF.

The range of qubit spectroscopy is limited by the resonant interaction of the ω_{ef} transition with the acoustic modes as well as prohibitively large phonon emission rates just outside the mirror bandwidths. For a transmon qubit, the dispersive regime must also consider the interaction of the harmonic modes with the ω_{ef} transition. These interactions make qubit readout breakdown between 4.4 GHz $< \omega_q/2\pi <$ 4.55 GHz. Additionally, the qubit has a prohibitively large linewidth

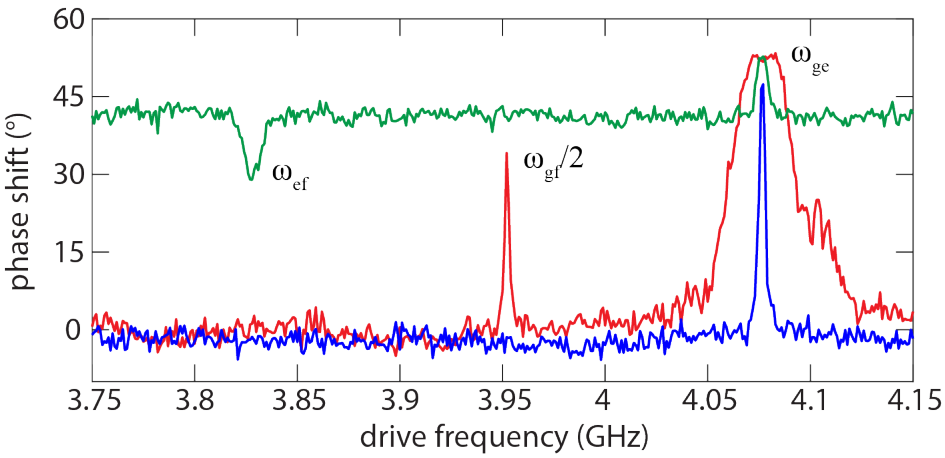

Figure 4.13: A weak spectroscopy tone shows the qubit transition (blue), while increasing the power 20 dB shows a broadened qubit transition as well as the two-photon $|g\rangle - |f\rangle$ transition (red) at a lower frequency. This gives $\alpha = 2\pi \times 250$ MHz. This anharmonicity is verified by observing the $|e\rangle - |f\rangle$ transition directly by applying an additional pump tone fixed at ω_{ge} (green).

above 10 MHz in the roughly 100 MHz span on either side of the acoustic band where its IDT efficiently converts the qubit excitation into propagating modes, as discussed more in the following sub-section.

4.2.3.3 Qubit Linewidth

Qubit spectroscopy can be used to characterize the qubit decay rate γ and the dispersive shift of any acoustic mode χ_m as a function of qubit frequency. The decay rate is measured spectroscopically by using a variable strength qubit drive to measure its linewidth. We observe the qubit linewidths depends on drive power even at the lowest powers that the transition is visible. To account for this power dependence, we infer the undriven qubit linewidth by fitting the power dependent linewidth and extrapolating to the zero power limit. This extrapolated linewidth does not differ dramatically from the lowest measured one.

The low-power qubit linewidth shows clear structure as a function of its frequency [Fig. 4.14]. The qubit interaction with the continuum of phonon modes is mediated by the inderdigitated transducer. The IDT has many coupling points over its many-wavelength extent that create a strong

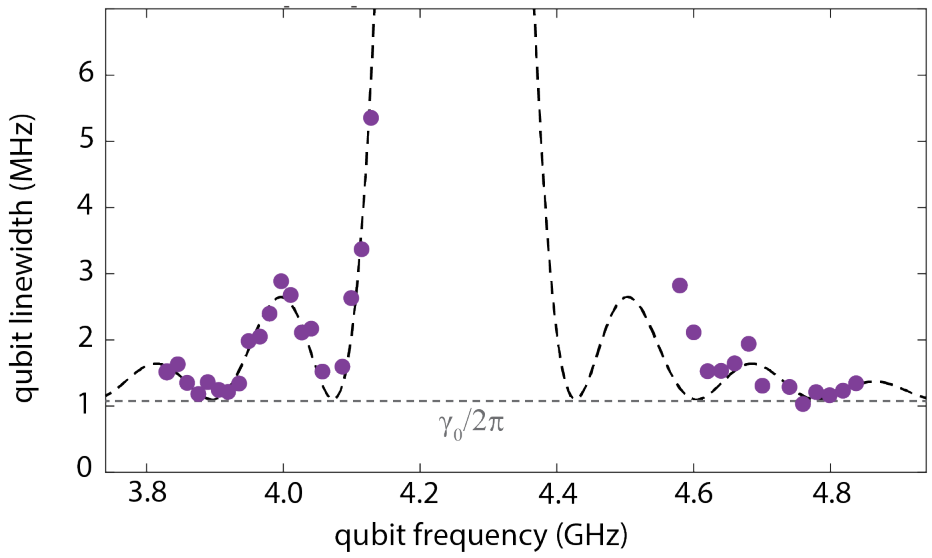

Figure 4.14: The qubit linewidth extrapolated to the low-power limit shows clear oscillations as a function of frequency. This structure closely matches the predicted qubit spontaneous emission rate to phonons, with a frequency-insensitive offset $\gamma_0 = 2\pi \times 1.1$ MHz.

frequency sensitivity in the qubit-phonon interaction strength which translates into a frequency-dependent qubit linewidth [Eq. 2.41]. The measured linewidths are well fit by the prediction for the qubit emission rate to acoustic modes based on the IDT geometry, which gives a simple $\sin^2 X/X^2$ form where $X = N_q\pi(\omega - \omega_c)/\omega_c$ dependence, plus a constant offset that accounts for other decay channels. The overall scale of the emission rate is given by Eq. 3.37, and here is equal to $\Gamma_0 = 2\pi \times 32$ MHz. The best fit for the constant offset gives $\gamma_0 = 2\pi \times 1.1$ MHz.

The qubit linewidth at the special frequencies were phonon emission from the IDT is prohibited by its geometry has special significance. First, this linewidth can be attributed to the frequency-independent qubit decay channels that are present when the qubit is tuned through the mirror bandwidth where phonon emission into the main SAW channel is suppressed. As this qubit internal loss rate of $\gamma_0 \approx 2\pi \times 1.1$ MHz is well below the qubit-cavity coupling strength, the device does indeed operate in the strong coupling regime. Second, this frequency of minimal loss demonstrates a unique feature of quantum acoustics with surface acoustic waves: a qubit can be

completely decoupled from the phonons at its resonant frequency to which it could decay while maintaining a strong coupling to detuned modes. This feature is leveraged successfully in an acoustic device in the following chapter (Ch. 5), but also suggests an alternative to standard Purcell filters in planar qubit design [119]. Instead of changing the density of states of the transmission line at the qubit resonant frequency, the qubit could be designed to decouple from modes at its resonant frequency by engineering interference between multiple points of coupling.

4.2.3.4 Acoustic Dispersive Shift

The dispersive shift of the qubit is measured by driving a given acoustic mode, here $m = 8$, with a coherent state of varying size while monitoring the qubit spectrum. The qubit linewidth exceeds the size of the dispersive shift, which means the shift of individual phonons is unresolved, and in the low phonon number limit the qubit experiences a smooth shift of size $2\chi_8\overline{n}_8$ where $\overline{n}_8$ is the average phonon number in mode 8. For qubit frequencies below the acoustic band, measurements indeed show that the qubit experiences a linear frequency shift with increasing average phonon number.

A calibrated measurement of χ_8 requires precise knowledge of average phonon number corresponding to each drive strength. However, the net attenuation in the lines is not known within ± 2 dB, which translates to a large uncertainty in the scaling of the power axis. The dispersive shift calculated from Eq. 3.27 matches the measured values when the qubit is below the cavity modes within this uncertainty. The conversion between drive power and average phonon number is then assumed to produce the calculated dispersive shifts.

While the dispersive shifts as a function of frequency closely follow the prediction below the acoustic band, at higher frequencies there is significant deviation [Fig. 4.15(a)]. The measured qubit frequency shift as a function of drive power is not linear for many frequencies in this range, and requires a description beyond the dispersive approximation. The model used here is a generalized Jaynes-Cummings model that takes into account the lowest four levels of the transmon as well as phonon occupancies in mode 8 up to 50 excitations. Like the standard Jaynes-Cummings model,

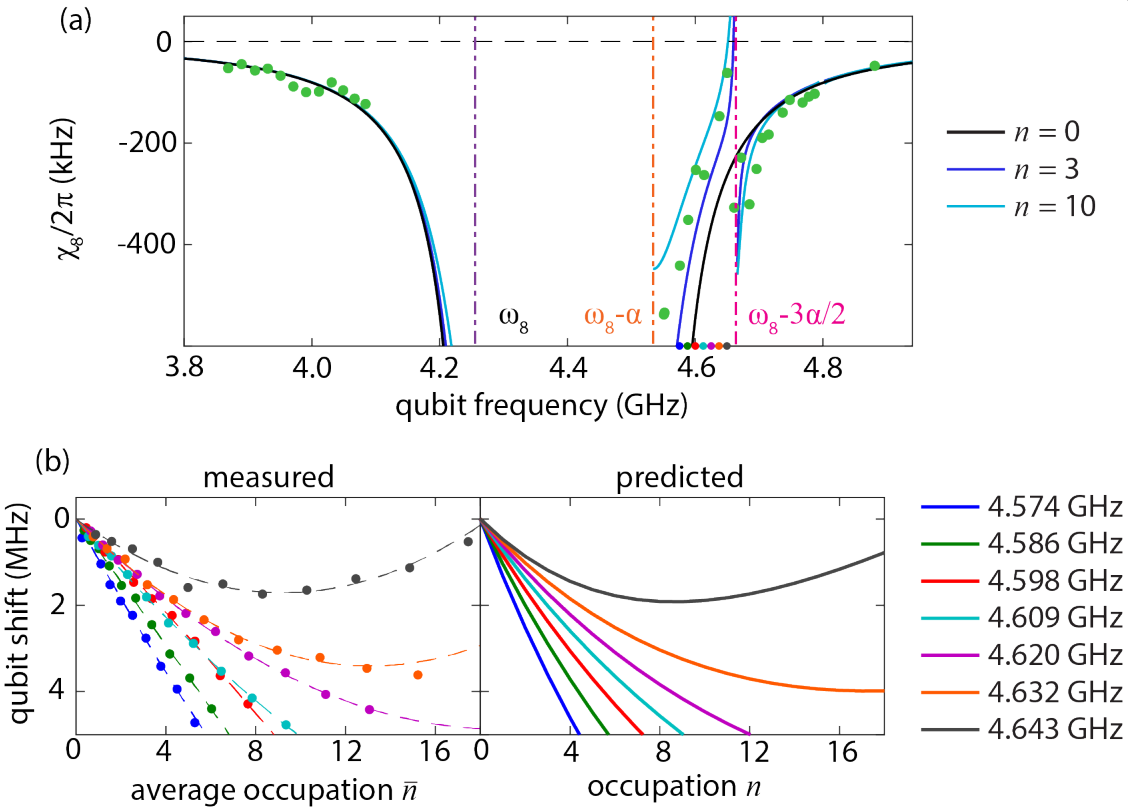

Figure 4.15: (a) The extracted dispersive shift for mode $m = 8$ shows good agreement with the predicted transmon behavior when $\omega_{ge} < \omega_8$, but deviates significantly above the cavity. A model incorporating multi-phonon transitions and higher levels of the transmon captures the behavior well, but predicts a (b) non-linear behavior with phonon-drive that is indeed measured in the experiment.

the Hamiltonian in matrix form is block diagonal. In manifold with at least four excitations n_e, each block of the Hamiltonian has the form,

$$H_{n_e}/\hbar = \begin{pmatrix} E_4 + (n-4)\omega_8 & 2\sqrt{n-3}g_8 & & & & \\ 2\sqrt{n-3}g_8 & E_3 + (n-3)\omega_8 & \sqrt{3(n-2)}g_8 & & & \\ & \sqrt{3(n-2)}g_8 & E_2 + (n-2)\omega_8 & \sqrt{(2(n-1)}g_8 & & \\ & & \sqrt{2(n-1)}g_8 & E_1 + (n-1)\omega_8 & \sqrt{n}g_8 & \\ & & & \sqrt{n}g_8 & E_0 + n\omega_8 & \end{pmatrix} \tag{4.8}$$

where $E_i = i\omega_q + i(i-1)\alpha/2$ are the levels of the transmon approximated as a duffing oscillator [Eq. 3.14] indexed by i, and the transmon-cavity coupling matrix elements are approximated to

grow as $\sqrt{i}$. The full matrix is diagonalized with a cutoff of 50 phonons for an array of qubit frequencies.

In the dispersive regime, the eigenvalues of the system $E(i,n)$ can be identified with a given transmon state i and phonon number n. The qubit transition with n phonons in the cavity is given by,

$$\omega_{ge}(n) = E(1,n) - E(0,n), \tag{4.9}$$

and so dispersive shift per phonon with n is,

$$2\chi(n) = \omega_{ge}(n+1) - \omega_q(n). \tag{4.10}$$

The dispersive shift diverges, and the dispersive approximation becomes invalid, when pairs of uncoupled energy levels become degenerate. In a standard three mode analysis, the two important degeneracies are when the $|g\rangle - |e\rangle$ transition or $|e\rangle - |f\rangle$ transitions are resonant with the cavity, i.e. E(1,n)=E(0,n+1) or E(2,n)=E(1,n+1). These interactions are both first order as they involve the exchange of one excitation. The presence of non-linear behavior in χ suggests that second order interactions also matter. The primary degenaracies to consider are when $E(2,n-2) = E(0,n)$ and when $E(3,n-2) = E(1,n)$. These second order crossings occur when $\omega_{ge} = \omega_8 + \alpha/2$ and $\omega_{ge} = \omega_8 + 3\alpha/2$. The former occurs in the straddling regime and is not measured, while the latter condition is precisely where the measured shifts deviate from the simple prediction.

The model can produce predictions for the dispersive shift given n phonons in the acoustic mode. The prediction with $n = 10$ phonons in the cavity closely follows the measured dispersive shift across the entire flux region measured [Fig. 4.15(a)]. However, as the shift per phonon is not constant, this misrepresents the qubit response; in many frequency regions, the qubit response to an increased drive is quadratic, not linear. The model qualitatively matches the measured qubit frequency in response to a phononic drive [Fig. 4.15(b)]

4.3 Conclusion

The device described in this chapter successfully demonstrated that surface acoustic waves could be strongly coupled to multi-mode acoustic resonators. Moreover, these quantum acoustic systems are shown to be well described by the familiar Jaynes-Cummings model, but with access to large delays that miniaturize multi-mode resonators and structure the qubit-phonon coupling in the frequency domain. Combined, these features give surface acoustic wave systems a unique ability to realize strong, multi-mode coupling, but with the access to specific frequencies where the qubit is dispersive with all resonant modes without significant spontaneous emission to unconfined modes.

The device also made clear several drawbacks of coupling superconducting qubits to surface acoustic waves. The qubit lifetimes are severely limited by dielectric loss from fine pitch of the capacitor and acoustic loss from radiation into uncontrolled phonon modes. At the same time, the qubit readout speed is limited by the small cavity external coupling rate and the small dispersive shift. The fast qubit decay compared to the readout time prohibited time-domain measurements of the qubit state. Additionally, the capacative coupling between the IDT and junctions likely contributed significant losses from interactions with defects hosted in the dirty oxide layer.

Chapter 5

Resolving Phonon Number States in a Multi-mode SAW Cavity

This chapter discusses the motivation, design, and measurement of a multi-mode acoustic cavity coupled to a transmon qubit that enters the strong dispersive regime where single phonons shift the qubit by more than its linewidth.

5.1 Multi-mode Strong Dispersive Regime

The strong dispersive regime provides many strategies for quantum control over linear resonant modes. For superconducting qubits coupled to electromagnetic resonators, reaching this regime [46] precipitated a large number of results demonstrating non-demolition photon measurement [105], creation of arbitrary photonic states [48], and interaction between photon modes with mutual coupling to a superconducting qubit [120, 25]. Entering the strong dispersive regime in mechanical systems would enable quantum control of phonons by deploying these similar techniques.

In particular, high-fidelity control over the high density of resonant modes present in SAW resonators would prove a powerful resource for processing quantum information. Harmonic oscillators are attractive candidates for storing quantum information because they typically have one dominant source of error (bit flips) [52], which simplifies correction schemes, and their large Hilbert space provides the freedom to store information in a range of encodings [53]. Electromagnetic resonators at microwave frequencies perform well but are bulky [51], and fitting large numbers of them in a dilution refrigerator is a daunting task. Mechanical resonators occupy a small fraction of the volume [121], and as demonstrated in the previous chapter, a dozen modes can be easily coupled to

a single superconducting qubit. Entering the strong dispersive regime with this significant number of modes would provide an alternative and hardware-efficient route to many qubits, where information is stored in the acoustic modes. The dispersive regime is particularly relevant in acoustic systems because the superconducting qubits typically have poor lifetimes compared to the acoustic resonances, an asymmetry that likely will grow as acoustic resonators can be exceptionally high-Q [19, 122, 123, 124]. Dispersive operation limits the loss inherited by the acoustic modes from the superconducting qubit [26].

There is, however, a tension inherent in trying to reach the strong dispersive regime in a multi-mode cavity. Consider a system composed of a cavity with resonant modes ω_m spaced by ω_s that couple to a qubit with strength g_m. To be dispersive, the detuning between the qubit and any acoustic mode must exceed their coupling strength, such that $g_m \gg \Delta_m$ for all m. If the coupling strength is constant between all modes, such that $g_m = g_0$, then since the maximum detuning is $\omega_s/2$, then $g_0 \ll \omega_s/2$ [Fig. 5.1(a)]. This limited coupling then constrains the dispersive shift, and a system must compromise either mode density or coupling strength to achieve dispersive operation.

A finite-bandwidth reflector side-steps this constraint by supporting resonant modes only in a specific frequency range. The qubit can then be dispersive with all resonant modes by operating at frequencies outside the mirror bandwidth as done in the previous chapter [Ch. 4]. However, once outside the mirror bandwidth, the qubit is exposed to the continuum of propagating modes, and its lifetime may be limited by spontaneous emission. The device in the previous chapter also demonstrated that the IDT allows the qubit to decouple from specific phonon modes, shielding it from acoustic loss at particular frequencies. However, in that device, the frequencies where emission was prohibited were too far detuned from the resonant modes for the acoustic dispersive shifts to be appreciable compared to the qubit intrinsic linewidth.

Another related strategy to enter the strong dispersive regime with a densely multi-mode resonator is to engineer the coupling strength to the resonant modes to vary. If, for example, g_m is proportional to detuning from a particular frequency with zero coupling, ω_z, then large coupling strengths can be achieved for modes more detuned without sacrificing dispersive operation or mode

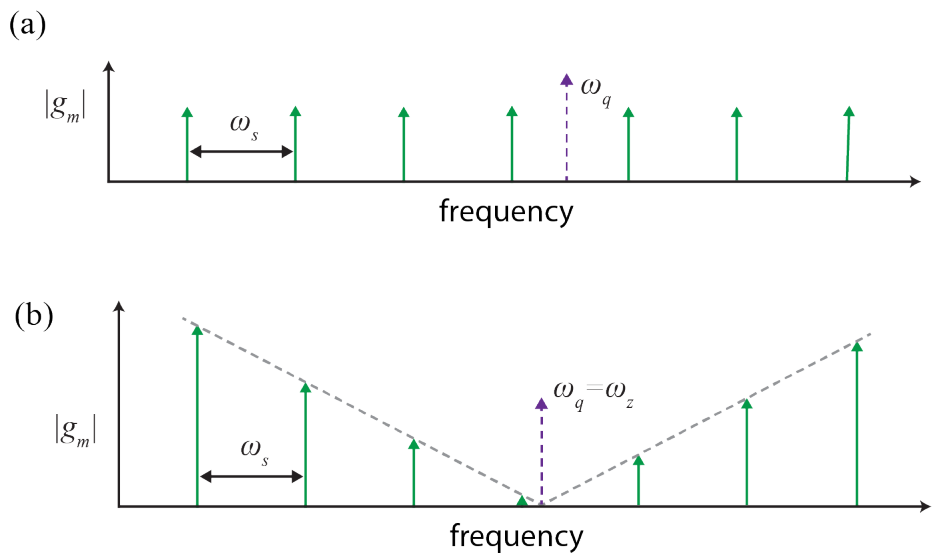

Figure 5.1: (a) A multi-mode cavity coupled to a two-level system with uniform strength is only dispersive if $g \ll \omega_s/2$. (b) If the coupling strength is proportional to detuning from the qubit with sufficiently shallow slow slope (dashed), then there is no such constraint.

density [Fig. 5.1(b)]. This proportionality creates a region of decreased coupling strength amid an array of strongly coupled modes; the qubit can be tuned into the low-coupling region for dispersive operation, while maintaining a high-density of resonant modes and a strong coupling rate to the rest of the resonances.

A qubit coupled to SAWs through an IDT is capable of realizing this frequency-structured interaction. The Fourier transform of the IDT geometry sets its frequency response [Eq. 2.41], and so a desired frequency response can be engineered by computing its inverse Fourier transform and shaping the IDT accordingly. And, as the speed of sound is slow, megahertz frequency resolution can be realized with millimeter geometries.

In a continuous wave context, an IDT can be designed to realize nearly arbitrary frequency responses. However, when the IDT forms the capacitor of a resonant circuit, either classical or quantum, the finest frequency resolution is limited by decay time of the resonance. The sharp features in the continuous wave IDT response depend on interference between spatially separated electrodes. A resonant circuit is not sensitive to these sharp features if it fully decays in a time scale

that is short compared to the travel time between these distant electrodes. This limitation includes decay into the SAW mode of interest as well as internal losses, so that if one segment of the qubit IDT radiates a phonon on a time scale faster than the transit time across the whole IDT, even a perfect qubit with no unintentional losses will not see the continuous wave IDT response. In this regime, the qubit environment becomes non-Markovian, characterized by information back-flow resulting in non-exponential decays [125, 109].

5.2 Split IDT Concept

The desired frequency dependent qubit-phonon interaction is realized by splitting the IDT in half. As in the previous device, a transmon qubit is formed by an IDT shunted by a SQUID loop and positioned inside a multi-mode SAW cavity. However, in this design, the IDT is split into two halves each of length D and separated by S [Fig. 5.2(a)]. The frequency domain response $A(\omega)$ is determined by the Fourier transform of the split IDT about its symmetry point [Eq. 2.44]. In close analogy to double slit diffraction, the Fourier transform of these two separated regions is the product of two terms: a slow sinc envelope centered on ω_c with period $2\pi \times v/D$ and a fast sinusoidal modulation with period $2\pi \times v/S$:

$$A(\omega) = \mathrm{sinc}[(\omega - \omega_c)D/2v] \sin[\omega\tau/2]. \tag{5.1}$$

where $\tau = S/v$. Essentially, a long phonon travel time τ between the two IDT halves creates sharp fringes in the qubit-phonon interaction rate as a function of frequency. In the absence of mirrors, the qubit spontaneous emission rate is proportional to $|A(\omega)|^2$ [Fig. 5.2(b)]. Inside the mirror band, the coupling between the qubit and a given acoustic mode is proportional to $A(\omega)$ and the amplitude of the acoustic mode at the center of the split IDT [Fig. 5.2(c)]. If the IDT is perfectly centered,

$$g_m = g_0 A(\omega_m) \approx g_0 \sin(\omega_m \tau) \tag{5.2}$$

where g_0 is the scale of the acoustic-qubit coupling strength if the IDT and the SAW standing wave were perfectly aligned, and the slow sinc is approximated as unity.

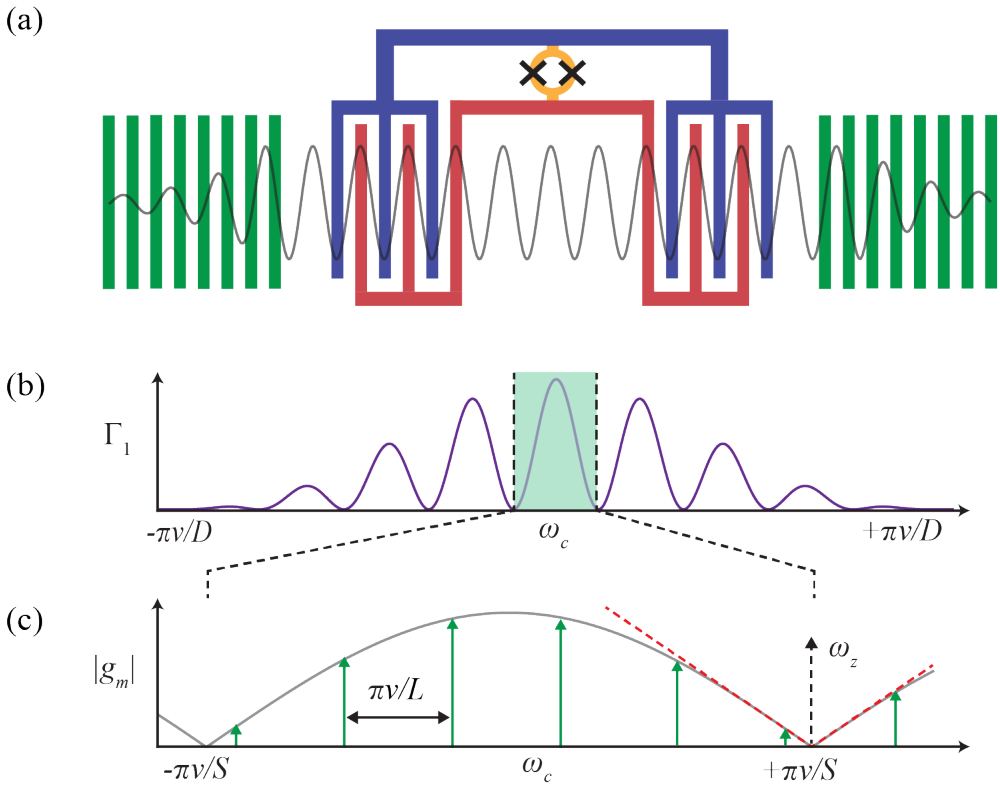

Figure 5.2: (a) A qubit with a intentionally designed frequency sensitivity is realized by splitting the IDT in half and embedding it in a SAW resonator. (b) The spontaneous emission rate of the qubit depends strongly on frequency with direct analogy to a double slit diffraction pattern in frequency space. (c) The strength of the resonant coupling inherits the same frequency dependence. The slope of the coupling near a zero crossing (red line) sets a floor on how dispersive the interactions are with nearby acoustic modes.

Dispersive operation with all acoustic modes can be realized regardless of the acoustic density or maximal coupling strength by careful design of $A(\omega)$. If the qubit is tuned to a frequency ω_z such that $A(\omega_z) = 0$, then it will decouple from phonons at its resonant frequency. Moreover, a cavity mode with detuning Δ_z from the qubit will couple with strength g_z that is bounded above by this detuning multiplied by the slope of the coupling strength near ω_z, i.e.,

$$|g_z| < g_0 A'(\omega_z)\Delta_z. \tag{5.3}$$

The magnitude of the slope at the crossing $g_0 A'(\omega_z)$ sets an upper bound on g_z/Δ_z and therefore sets

a floor for how dispersive the qubit-cavity interactions can be as shown in [Fig. 5.2(c)]. If the slope is sufficiently shallow, then all resonant modes will be dispersive, regardless of the mode density or their exact resonance frequencies. The robustness of the design to the exact frequencies of the acoustic cavity is especially important because these resonant frequencies of acoustic cavities cannot be determined in design; as in the earlier device [Sec. 4.1.3], there is uncertainty in the positioning of the acoustic structures that exceeds a wavelength, which means that while the mirror bandwidth and free spectral range are well determined, the actual resonant frequencies vary significantly device to device.

5.2.1 Split IDT Design

The acoustic cavity is centered at the same frequency $\omega_c = 2\pi \times 4.25$ GHz as the previous device, but its area is decreased to increase the coupling to the qubit. Its width of 16 µm limits the acoustic linewidth to approximately 250 kHz, and the length of 125 µm gives a free spectral range of $\omega_s \approx 2\pi \times 10$ MHz after accounting for the 16 µm of mirror penetration per side. The transmon has $N_q = 16$ finger periods total in its IDT, this results in a bare acoustic coupling strength of 15 MHz.

5.2.1.1 Readout Cavity

To readout and control the qubit, it is strongly coupled to a 3D electromagnetic resonator by attaching antenna paddles to either side of the IDT. The electromagnetic resonator is a metal box made from a machined slot in two pieces of copper [Fig. 5.3]. Its transverse dimensions of 35 mm by 35.5 mm are designed to support a fundamental TE_{01} resonant frequency near $\omega_r = 2\pi \times 6$ GHz while pushing higher modes above 10 GHz. The seam is located at the center of the cavity, where by symmetry no currents flow, thereby reducing seam losses. The cavity is 5 mm deep, which, with paddles that are each 725 µm long and 150 µm wide, creates a bare coupling strength with the 3D resonator of 180 MHz. The copper cavity also creates a clean and well controlled microwave environment for the qubit, particularly compared to the complicated environments typical in sample

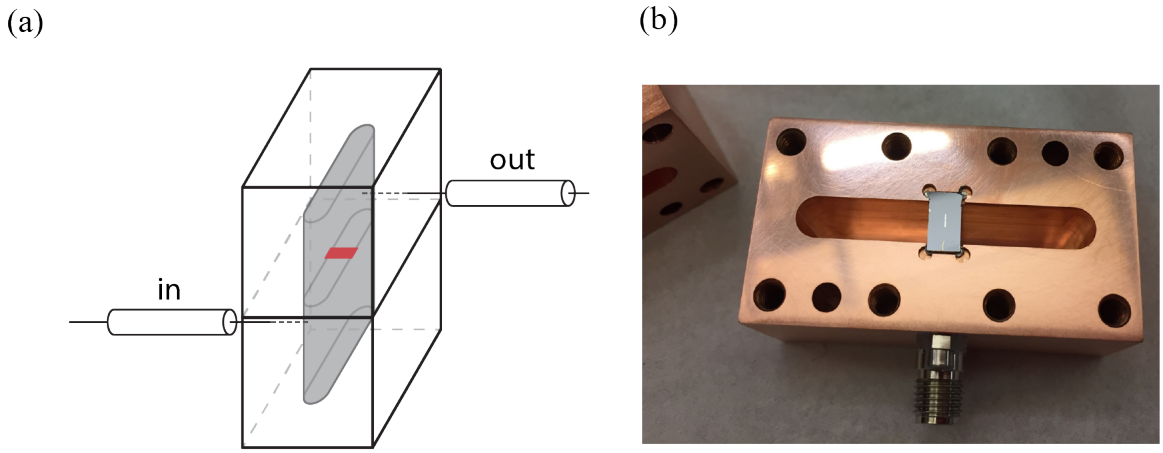

Figure 5.3: The qubit is strongly coupled to a copper waveguide cavity with frequency near 6 GHz. The qubit state is read out by monitoring the resonant frequency of the cavity.

packaging for devices with planar readout cavities. The qubit rests in a slight recess in one half cavity and is held in place by indium dots [Fig. 5.3(b)].

Two microwave transmission lines are coupled to the cavity by inserting their center conductors some length into cavity. One pin is farther into the cavity, giving it an external coupling rate of near 2 MHz that dominates the cavity linewidth. This line runs to the microwave measurement chain. The other pin is recessed somewhat from the cavity mode in a waveguide below cutoff, reducing its external coupling rate to near 100 kHz. This line is used to drive the cavity and the qubit.

5.2.1.2 Transmon Qubit Design

The transmon is made up of two capacitors; one for coupling to the acoustic cavity and the other to couple to the readout cavity. This two capacitor design reduces the coupling to both the 3D resonator as well as the IDT. The total capacitance is approximately 120 fF, giving $E_C/h \approx 160$ MHz. The IDT makes up about 40% of this capacitance, and so its coupling is reduced to $g_0 \approx 2\pi \times 5.5$ MHz, while the readout cavity coupling is reduced to $g_e = 2\pi \times 110$ MHz. The

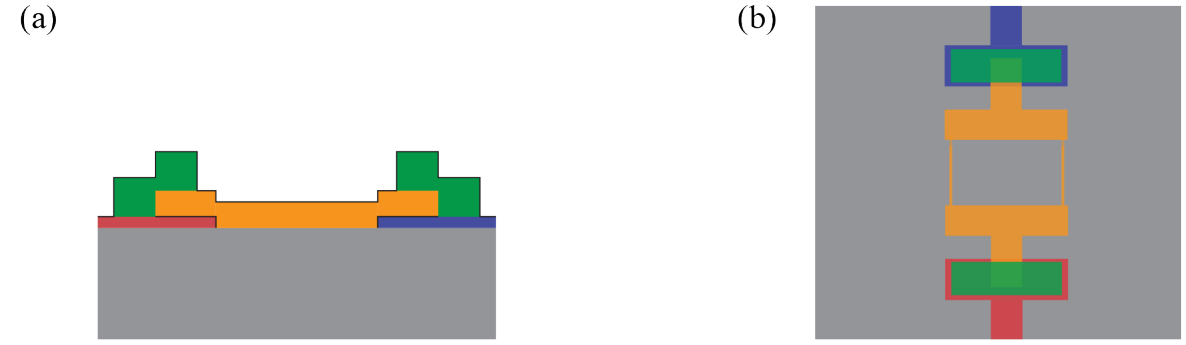

Figure 5.4: The two separate depositions of aluminum used to define the acoustic features (red/blue) and the Josephson junctions (yellow) are connected using a third layer of aluminum (green). Immediately before depositing the bandage layer, the sample is cleaned with an argon plasma to remove the oxide layer (black).

large capacitor paddles also reduce the electrical participation ratio of the GaAs surface. This would improve the qubit linewidth if this lossy surface was the dominant loss source in the device, but would do little to improve unwanted radiation into unconfined acoustic modes.

The delay between the two IDT halves is chosen so that, with the qubit tuned to a zero crossing in the qubit-phonon interaction, all the acoustic modes will be dispersive. This slope is given by $g_0 A'(\omega_z) \approx g_0\tau/2$. We chose $\tau = 9$ ns so that $g_0\tau/2 = 0.14 \ll 1$. This guarantees that modes will be detuned by at least 7.2 times their coupling strength when the qubit is tuned to ω_z. This delay also conveniently results in a period between coupling minima of 110 MHz that matches the expected mirror bandwidth of near 80 MHz, guaranteeing there will be a maximum in $A(\omega)$ within the mirror band.

5.2.2 Fabrication

The fabrication of this device differs from the previous device only in how the IDT layer is connected to the junctions. Here, these two layers are galvanically connected by a third layer of aluminum [Fig. 5.4]. This third layer, called the bandage layer, is deposited on top of both of the other layers. Electrical continuity is achieved by preceding the bandage layer deposition with an

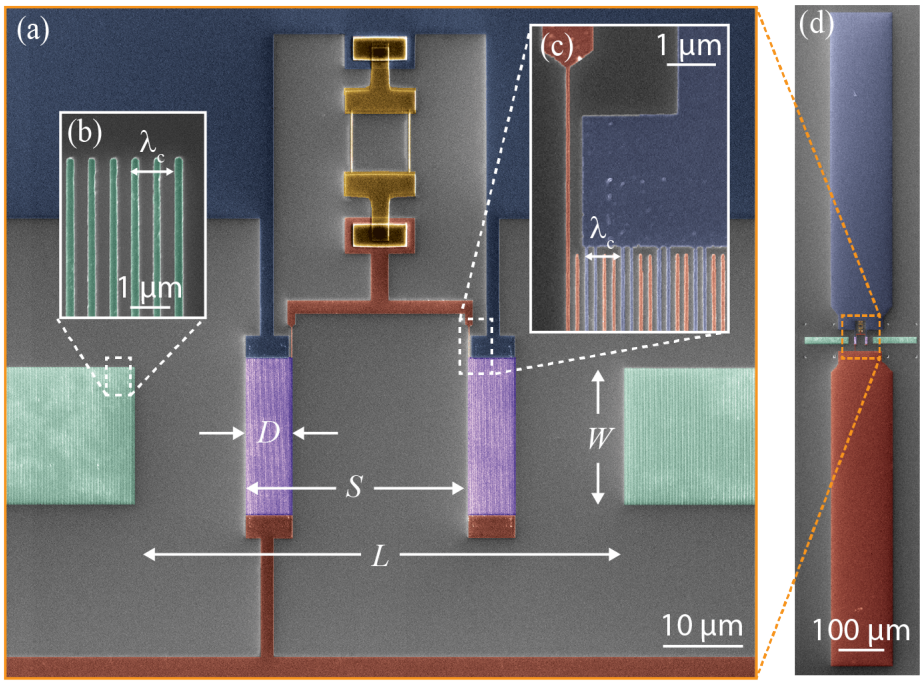

Figure 5.5: A false color SEM image showing the aluminum device on the GaAs substrate. Acoustic reflectors (green) confined phonons to form a multi-mode SAW resonator. The qubit is formed by a pair of Josephson junctions (yellow) shunted by both an IDT (purple) as well as large antenna paddles (red/blue) that couple it to the readout cavity. The mirrors in the imaged device have half the separation as the mirrors in the measured device.

argon plasma clean that scrubs away the oxide layer on the underlying aluminum. The bandage layer is deposited shortly after the argon plasma clean without breaking vacuum. Such an argon plasma etch would ruin the resist bridges of the Josephson junctions, and so it cannot be done in the same step as the junctions.

A false color SEM image shows the device in Fig. 5.5. The acoustic cavity is formed by two Bragg mirrors situated between the paddles that couple the qubit to the readout cavity. An IDT formed by two 8-period halves split by 27.2 μm is placed at the center of the cavity. The innermost fingers of each IDT are pulled through the cavity so that the junctions can shunt the IDT easily. Only one pair of these IDTs is connected to the lower paddle to avoid creating a superconducting loop. All of the aluminum except the junctions and the bandage layer are deposited in one step.

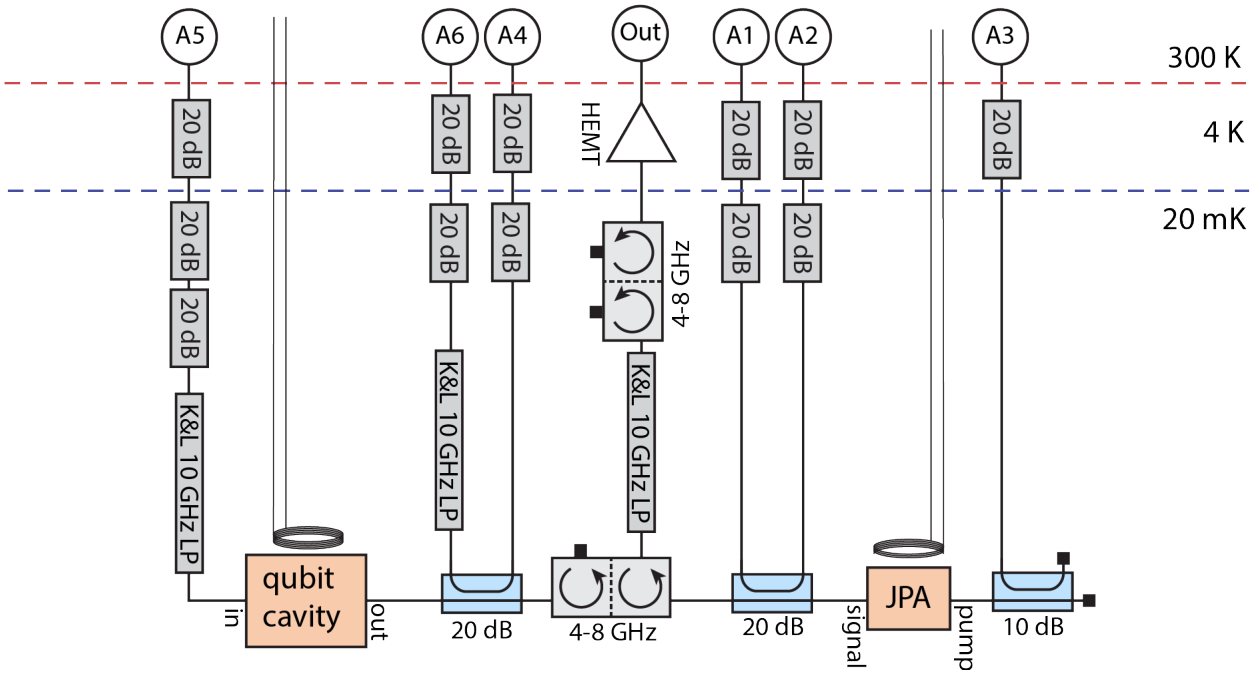

Figure 5.6: The readout cavity is driven through a weakly coupled port, while a strongly coupled port leads to the amplification chain. The JPA has a separate pump port used for direct flux modulation at $2\omega_r$.

5.3 Measurement

Measurements are performed by measuring transmission through the electromagnetic readout resonator at the base of a dilution refrigerator. As shown in the wiring diagram [Fig. 5.6], a JPA downstream from the cavity either provides narrow-band gain when pumped or else acts as an open and completely reflects incident signals. Magnetic flux applied from a coil attached to the readout cavity tunes the qubit frequency down from a maximum frequency above the readout cavity. Sweeping the applied flux reveals an avoided crossing between the transmon qubit and the readout cavity, which gives both the coupling rate $g_e = 2\pi \times 114$ MHz as well as a good approximation of the qubit frequency as a function of flux.

5.3.1 SAW cavity Avoided Crossings

Away from the avoided crossing with the readout cavity, the dispersive qubit-cavity interaction can be used to perform qubit spectroscopy. The transmission of the readout tone changes as a drive tone polarizes the qubit. Here, measurements of the qubit-acoustic interactions are made by observing the qubit, instead of the acoustics as in the previous chapter.

As the qubit is tuned across the acoustic band, its spectrum shows pronounced avoided crossings with a clear frequency-dependent coupling strength [Fig. 5.7(a)]. The eigenmodes of the system are found by diagonalizing a multi-mode interaction Hamiltonian as in the previous chapter [Eq. 4.4]. Here, however, each mode has an independent coupling strength, which can be extracted as the coupling strengths are less than ω_s. Fitting this model to the avoided crossings extracts coupling strengths that vary significantly from one mode to the next [Fig. 5.7(b)]. Three main effects explain the observed variation. First, neighboring cavity modes spaced by $\omega_s \approx 2\pi \times 10$ MHz have alternating coupling strength because the IDT is approximately symmetric about the cavity center, coupling the qubit strongly to even acoustic modes and weakly to odd ones. Second, the interference between the IDT halves modulates the coupling proportional to $A(\omega)$ as intended; strong coupling with $g_0 = 2\pi \times 5.1$ MHz is achieved at the center of the mirror band, but the coupling vanishes by ± 50 MHz in either direction. This is precisely the frequency-dependent structure that the split IDT was designed to achieve. Finally, resonant exchange between the qubit and the cavity modes at the edge of the mirror bandwidth is spectrally unresolved as the coupling rate is reduced by $A(\omega)$ and the intrinsic loss of the cavity increases. Transverse modes are also present at slightly higher frequency than the even longitudinal modes, and couple with a strength about five times smaller than their associated purely longitudinal modes.

5.3.2 Interaction with Unconfined Phonons

The avoided crossing measurements, while showing the desired mode-dependent interactions, only sample $A(\omega)$ discretely and in a small frequency range. The structuring of the qubit-phonon

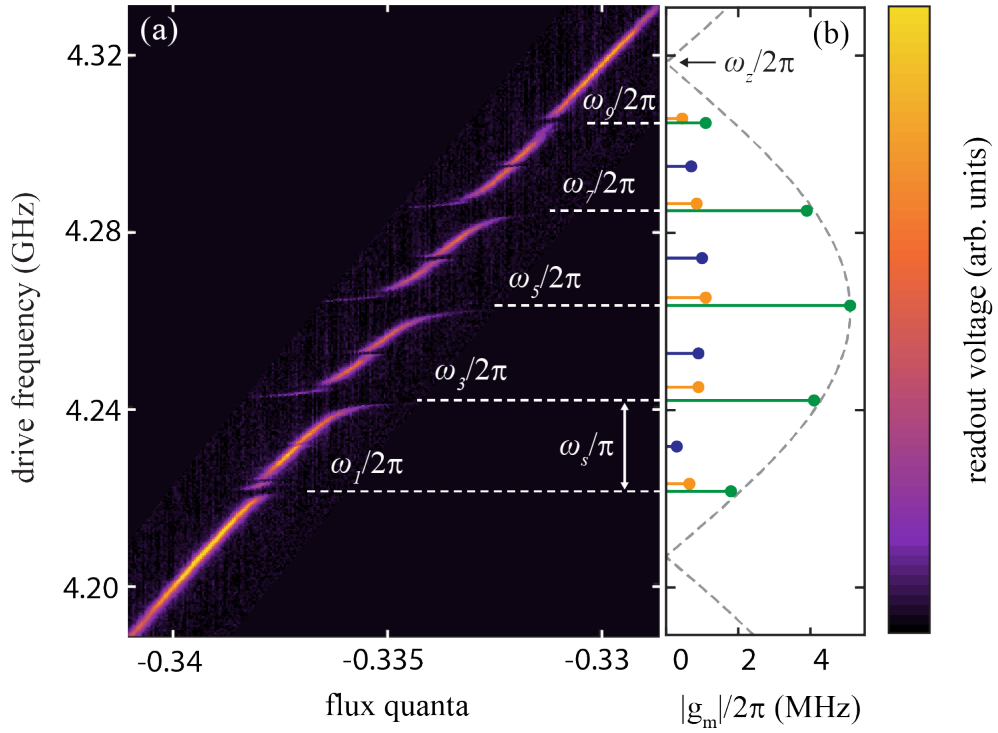

Figure 5.7: (a) As the qubit is tuned across the acoustic modes, pronounced avoided crossings appear in its spectrum. (b) The extracted coupling strengths show that the qubit couples preferentially to even modes (green) at the center of the mirror bandwidth while decoupling odd modes (blue) as well as from phonons at either end of the mirror bandwidth. Transverse modes (yellow) were present at the high-frequency shoulder of the even longitudinal modes. A prediction for $A(\omega)$ extracted from T_1 measurements fits the data well (dashed).

interaction can be determined with greater clarity by monitoring the qubit spontaneous emission rate and resonant frequency as it is tuned outside the mirror bandwidth. When exposed to the continuum of unconfined phonon modes, the qubit emits a phonon at a rate proportional to $|A(f)|^2$. The qubit spectra is recorded as it is tuned over a 1-GHz span, and the flux dependence is subtracted to emphasize the features arising from acoustic interactions [Fig. 5.8]. At frequencies detuned from the mirror bandwidth and its associated avoided crossings, the qubit linewidth oscillates with a period of 110 MHz that is consistent with a delay time of 9 ns and an amplitude that decays as the qubit tunes out of the bandwidth of the IDT halves. Additionally, the qubit frequency itself deviates from a simple model of its flux dependence, with residuals from a best fit flux dependence

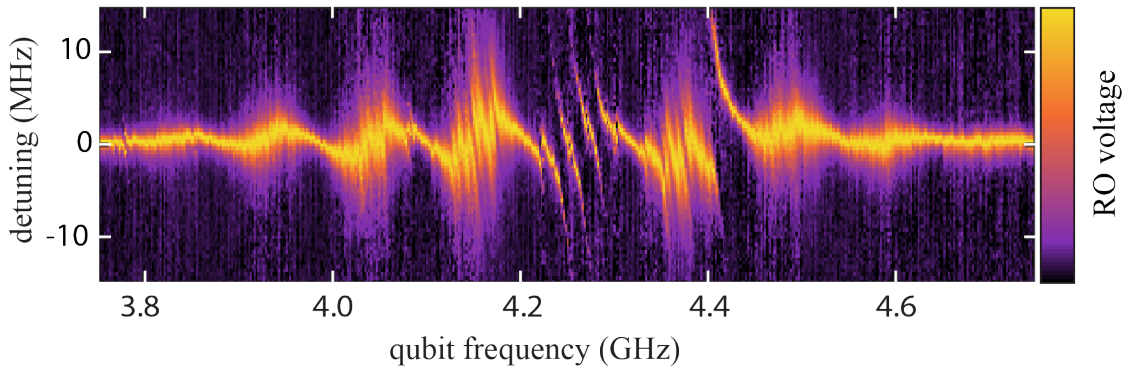

Figure 5.8: The qubit spectrum is monitored as it is tuned over a 1-GHz span, and the best-fit flux dependence of its resonant frequency is subtracted to highlight the acoustic features. Outside the bandwidth of the mirrors, where the qubit hybridization with the acoustic modes creates avoided crossings, the qubit linewidth and frequency both show clear oscillations generated by its frequency-sensitive interaction with propagating phonon modes. A crossing with a mode of unknown origin occurs at 4.41 GHz.

showing oscillations at 110 MHz with an envelope matching the linewidth variation. This deviation from a simple flux dependence arises from the reactive part of the IDT admittance, and is analogous to the Lamb shift from atomic physics [126, 59]. Both of these effects, investigated in more detail below, are well described by modelling the qubit emission of phonons from the IDT as a frequency-dependent conductance, which must be accompanied by a frequency dependent reactance from Kramers-Kronig relations. The spectrum also shows a large avoided crossing with a defect mode at 4.41 GHz of unknown nature.

5.3.2.1 Phonon emission rate

The qubit energy decay rate is determined by measuring the excited state lifetime (T_1) in the time domain [Fig. 5.9]. In contrast to spectroscopic measurements of linewidth, the measured excited state lifetime is insensitive to dephasing effects as well as broadening from the applied drive. With the qubit far detuned from the acoustic cavity modes, we observe oscillations of $\Gamma_1 = T_1^{-1}$ in frequency with large amplitude; the loss increases by a factor of 25 above its minimal value within a 55 MHz span. The loss follows a model that combines a prediction for the phonon emission rate

from the IDT and a constant internal quality factor Q_i,

$$\Gamma_1(\omega_q) = \frac{\omega_q}{Q_i} + \frac{\Gamma_0}{2}\text{sinc}\left(\pi N_q \frac{\omega_q - \omega_c}{\omega_c}\right)^2 [1 - \cos(\omega_q \tau)], \tag{5.4}$$

where Γ_0 is the qubits maximal loss rate to phonons. The best fit is for $Q_i = 1.2 \times 10^4$, $\Gamma_0 = 2\pi \times 11$ MHz, $\omega_c = 2\pi \times 4.24$ GHz, and $\tau = 9.04$ ns. The measured value of Γ_0 is close to the predicted value using room temperature GaAs parameters of 12.5 MHz.

The minima in the qubit linewidth are caused by destructive interference between a single phonon emitted from both halves of the IDT, an effect which has close parallels to an atom interfering with its mirror image [127, 128]. The uniformity of the minima cross the IDT strongly suggests that any residual loss from imperfect interference between the IDT halves is below 100 kHz; the emission from each IDT changes by more than order of magnitude over the measured span, which would impact the depths of the nulls if the interference between the two halves were imperfect. This uniformity confirms that $A(\omega)$ is real and goes through zero, implying the IDT halves are indeed symmetric.

The qubit constitutes a so-called "giant-atom" where the intra-IDT delay time approaches the phonon-emission limited qubit lifetime. As discussed earlier, deep in this regime the qubit decays fully before a phonon can travel between the IDT halves, leading to non-Markovian physics [125, 109]. The transition to this regime occurs when the product $\Gamma_0\tau/2$ approaches unity; for this device, $\Gamma_0\tau/2 = 0.3$. Any potential evidence of non-Markovian physics is obscured by the presence of the mirrors which structure the phononic environment near the center of the IDT bandwidth, as well as the shortness of the time scale (9 ns) of the non-exponential features compared to the measurement time. A small fraction of measured decays did display non-exponential features, but with time scales long compared to τ. The frequencies associated with these decays were excluded from the fit [Fig. 5.9(b)].

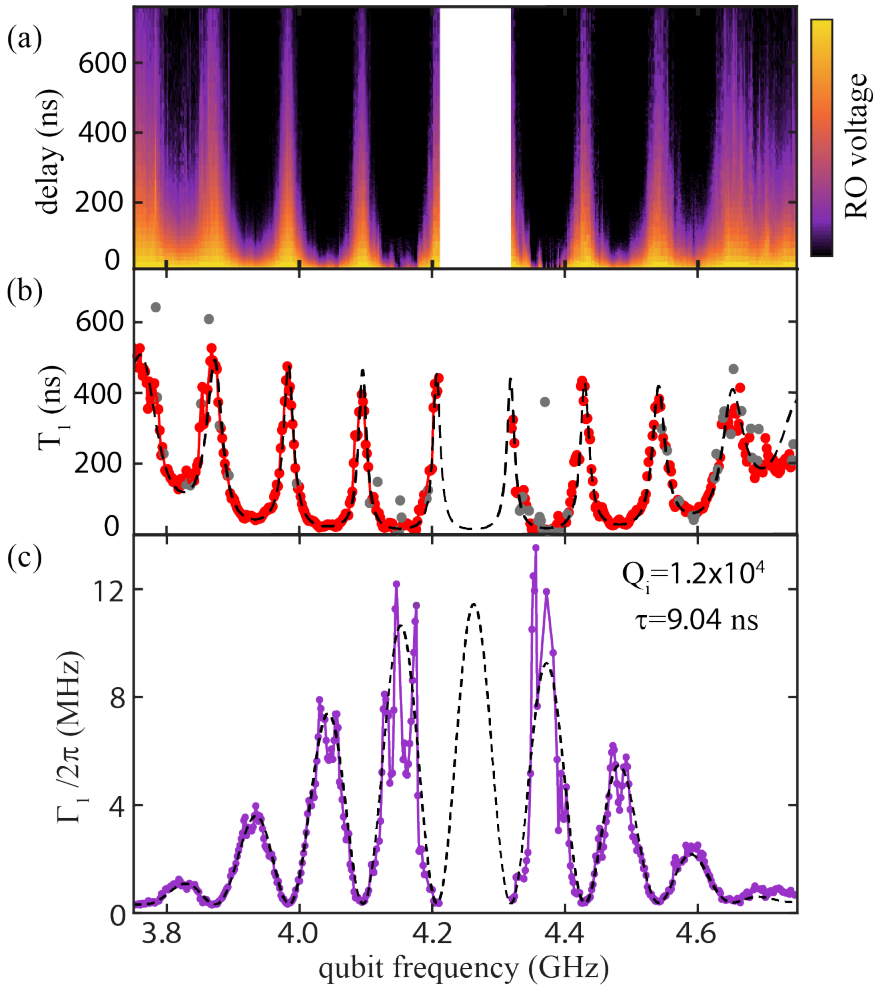

Figure 5.9: (a) The qubit excited state lifetime is measured as a function of flux over a 1-GHz span excluding inside the mirror bandwidth. The observed decays become significantly longer at specific frequencies where phonon emission is prohibited by the coherent cancellation between a single phonon emitted emitted from each half of the IDT (b) The extracted decay times closely match the a model for the T_1 time based on a fixed Q_i and phonon emission from the IDT. Non-exponential decays occur occasionally and are excluded from the fit (gray). (c) The qubit relaxation rate highlights the agreement at short lifetimes and shows the clear analogy to double-slit diffraction. At the largest Γ_1, two effects contribute to increased variability: the mirrors are slightly reflective and structure the phonon environment, and the exceedingly fast decays are difficult to measure precisely.

5.3.2.2 Phononic Lamb Shift

The precise measurements of the IDT parameters from the qubit loss rate can be used to calculate the effective phononic Lamb shift of the qubit. This shift is related to the reactive part of the IDT admittance [Eq. 2.42], and is given by,

$$\delta(\omega_q) = \frac{\Gamma_0}{4}\mathrm{sinc}\left(\pi N_q \frac{\omega_q - \omega_c}{\omega_c}\right)^2 \sin(\omega_q \tau/2). \tag{5.5}$$

While the magnitude of this shift is small (± 3 MHz), the oscillations have mean zero over a large span and are on a much finer frequency scale than the flux dependence. Including junction anisotropy as in Eq. 3.12, the qubit flux dependence follows,

$$\omega_q(I) = \omega_0 \left[a^2 + (1-a^2)\cos\left(\pi \frac{I - I_0}{I_c}\right)^2\right]^{1/4}, \tag{5.6}$$

where ω_0 is the zero-field qubit frequency, I_c is the coil current required to thread a half flux quantum through the $50\,\mu\mathrm{m}^2$ qubit loop, I_0 is the current offset required to offset ambient fields, and a is the normalized difference between the junction critical currents. Fitting the measured qubit frequency [Fig. 5.10(a)], gives $\omega_0 = 2\pi \times 5.718\,\mathrm{GHz}$, $I_c = 1.168\,\mathrm{mA}$, $I_0 = 79.2\,\mu\mathrm{A}$, and $a = 0.14$. This fit cannot capture the fast fluctuations from the phononic Lamb shift; indeed, the residuals from the flux dependence match the expectations for the Lamb shift with no free parameters, excluding regions near avoided crossings [Fig. 5.10(b)]

The measurements of the qubit interacting with propagating SAWs provides also provides an independent inference of the interaction strength between the qubit and the cavity resonances. The best-fit model for $A(\omega)$ from the qubit loss rate can be extended to frequencies inside the mirror bandwidth. This prediction is shown in Fig. 5.7(b) and shows good quantitative agreement with the measured coupling strengths.

5.3.3 Number Splitting Measurements

Having characterized the resonant interaction between the qubit and both propagating and cavity phonons, we turn to measuring the dispersive shift of the qubit from cavity phonons. To

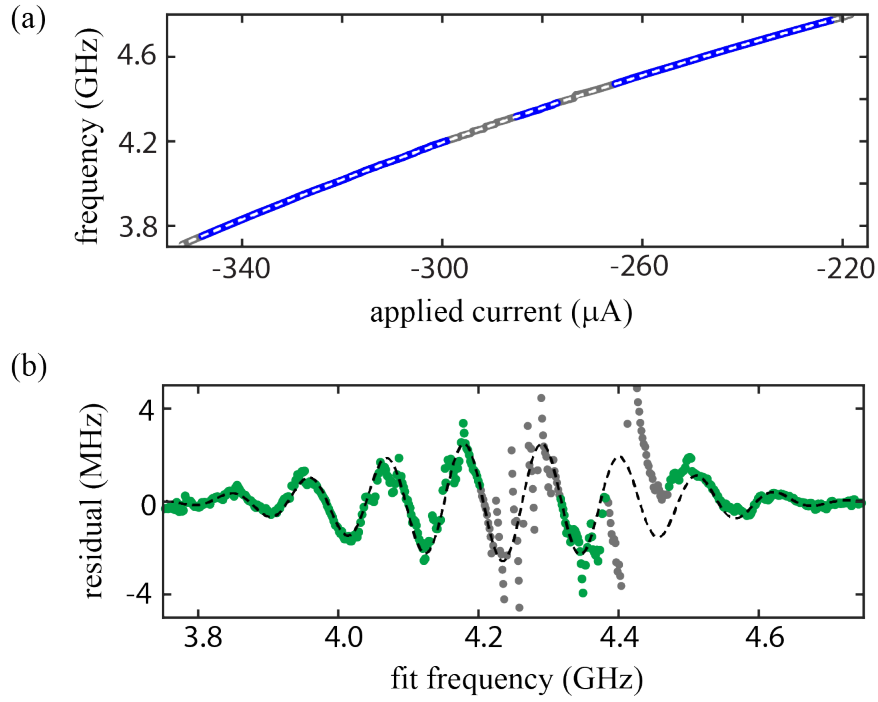

Figure 5.10: (a) The measured qubit frequency away from avoided crossings (blue) is fit well a flux-dependent model including junction asymmetry (white dashed) excluding points near avoided crossings (gray). (b) The residuals from the flux-dependent fit show clear oscillations. A prediction with no free parameters based on the measured phonon emission rate closely matches the residuals, indicating that these features are a phononic Lamb shift.

achieve the goal of entering the strong dispersive regime, we must confirm both that the qubit is detuned from all cavity modes by many times its coupling strength, i.e. $g_m \ll |\Delta_m|$, and that the dispersive shift χ_m exceeds both the qubit and acoustic loss rates. Tuning the qubit to $\omega_z = 2\pi \times 4.318$ realizes dispersive operation: the least-dispersive interaction is with mode $m = 7$, with $\Delta_7/g_7 = 8.5 \gg 1$. In this dispersive regime, the Hamiltonian simplifies to a sum of dispersive shifts of size χ_m for each mode, as in Eq. 3.29, where χ_m must include the third level of the transmon, as in Eq. 3.27. The anharmonicity for this device is $\alpha = -2\pi \times 190$ MHz measured at $\omega_q = 2\pi \times 4.318$ GHz, although this anharmonicity does depend on frequency because of the phononic Lamb shift.

The qubit would be dispersive with all acoustic modes if it was tuned to either the top or

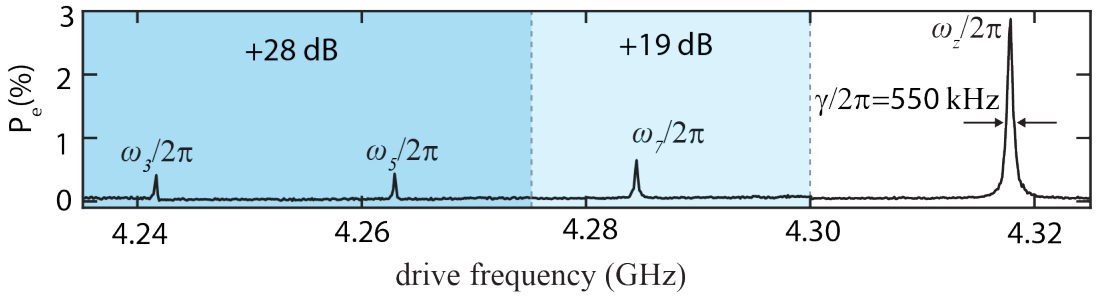

Figure 5.11: With the qubit tuned to ω_z, it does not hybridize strongly with any acoustic mode and has a linewidth of $\gamma = 2\pi \times 550$ kHz. By driving orders of magnitude harder, the small residual qubit hybridization with the acoustic modes allows them to be driven and read-out. The acoustic modes have linewitdhs $\kappa_1 = 2\pi \times 200$ kHz, $\kappa_3 = 2\pi \times 250$ kHz, $\kappa_7 = 2\pi \times 275$ kHz,

the bottom of the mirror bandwidth. However, the dispersive shift is much larger with the qubit tuned above the acoustic resonances. This asymmetry is because, with the qubit at the bottom of the mirror bandwidth, the contribution to the dispersive shift from the $|e\rangle - |f\rangle$ transition of the transmon counteracts the shift from the $|g\rangle - |e\rangle$ transition, while at the top of the mirror band these two contributions add constructively to create large and positive dispersive shifts. This configuration is called the straddling regime [92] and the boost it provides to dispersive shifts was recently used to enter the strong dispersive regime between a superconducting qubit and a magnon [129].

The measurement of the dispersive shift of a given mode requires that mode to be populated with phonons. To displace a target mode, we drive the qubit at a frequency far detuned from its own transition frequency but resonant with the cavity mode [67]. The slight residual hybridization turns this qubit drive into a weak cavity drive. Qubit spectroscopy in Fig. 5.11 shows the qubit transition at $\omega_q = 2\pi \times 4.318$ GHz, and, with orders of magnitude higher drive power, the three acoustic resonances with the strongest qubit coupling at lower frequencies.

The measured qubit linewidth of $\gamma = 2\pi \times 550$ kHz is consistent with measurements of energy decay, intrinsic dephasing, and broadening from the qubit drive tone. The qubit coherence times are measured in the time domain to be $T_1 = 415$ ns and $T_2^* = 705$ ns [Fig. 5.12]. The T_1 decay

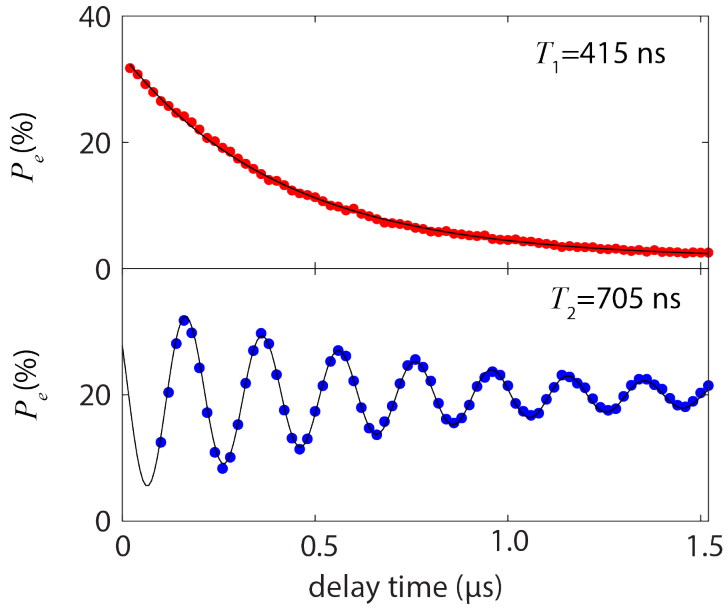

Figure 5.12: The qubit $T_1 = 415$ ns and $T_2 = 715$ ns times are measured with the qubit tuned to ω_z.

contributes the most to the qubit linewidth, at $T_1^{-1} = 2\pi \times 360$ kHz. As the T_2^* time is nearly twice T_1, the intrinsic dephasing time T_ϕ is small, adding only $T_\phi^{-1} = 2\pi \times 30$ kHz to the qubit linewidth. Together with the effective Rabi rate from the drive tone (100 kHz) and the finite pulse duration (50 kHz), the expected qubit linewidth is 540 kHz. Additionally, the measured acoustic linewidths of $\kappa_m \approx 2\pi \times 250$ kHz agree with the expectations of diffraction limited Q [Eq. 2.33] from their finite width of 16 µm.

We measure the dispersive shift of the three strongly coupled modes by varying the population in these modes while monitoring the qubit spectrum. A 3 µs drive pulse at ω_m creates a coherent state in mode m with $\overline{n}_m$ average phonons. The resulting spectrum, measured with a spectroscopy pulse concurrent with the acoustic drive, consists of a sum of Lorentzians that each correspond to a phonon number state in the cavity [Fig. 5.13]. These Lorentzians are spaced by $2\chi_m$ and broaden with higher phonon number in proportion to κ_m; the loss of a phonon effectively measures the qubit state and therefore causes increased qubit dephasing. As the drive power at each of the three modes

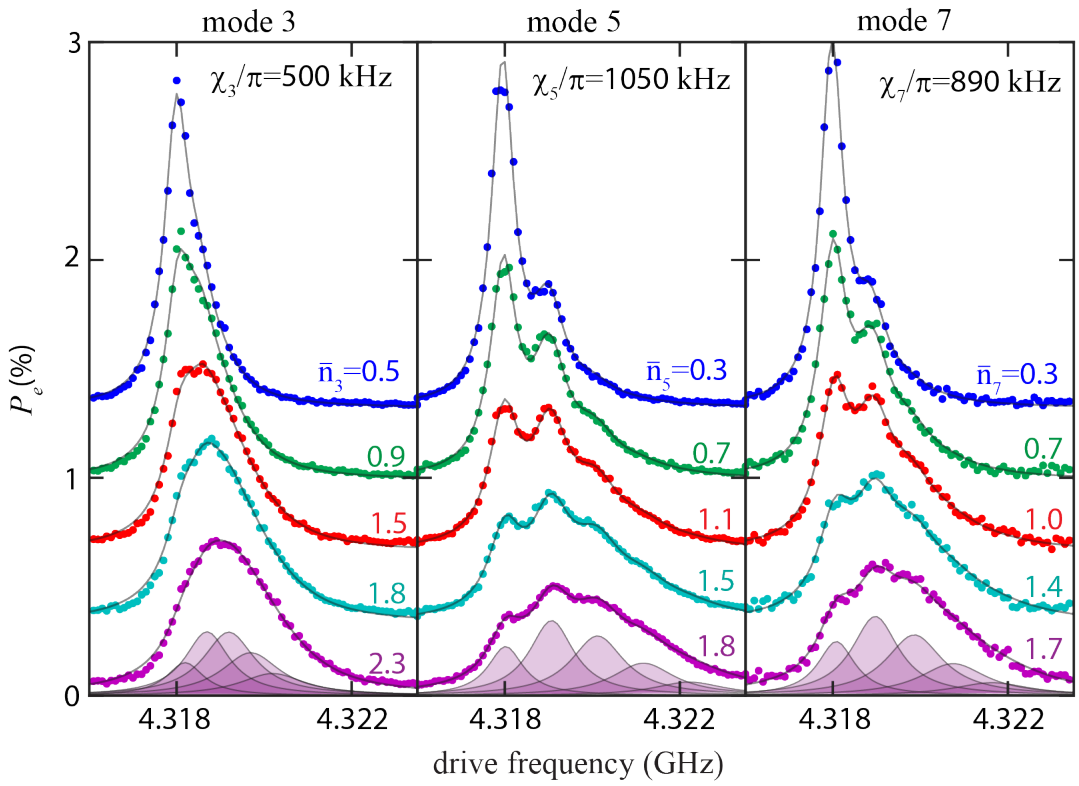

Figure 5.13: The qubit spectrum is measured while three different acoustic modes are driven. For modes $m = 5, 7$, multiple resolved peaks appear, each corresponding to a different phonon number state. The fits assume a coherent state distribution and agree well with the measured spectra. The contribution from each phonon number state to the highest $\overline{n}$ trace are plotted separately at the bottom of each panel.

is increased, the measured qubit spectrum broadens and shifts upwards in frequency, consistent with the positive dispersive shifts in the straddling regime [92]. Crucially, several resolved peaks appear in the qubit spectrum for modes $m = 5$ and $m = 7$. Each peak corresponds to a different Fock state in the phonon number distribution.

To model the measurement, we assume the cavity occupation is Poissonian distributed and fit the average phonon number in each trace. The measured spectra are fit to a sum of Lorentzians,

$$P_e(\omega, \overline{n}) = C_0 + C_1 \sum_{n=0}^{n_{\max}} P_n(\overline{n}) S(\omega, \overline{n}, n), \tag{5.7}$$

where C_0 is an overall offset, C_1 an overall amplitude, ω is the spectroscopy frequency, $n_{\max} = 6$ is

a cutoff phonon number, and P_n is the weight of Lorentzian $S(\omega, \overline{n}, n)$ with n phonons. These two terms are given by,

$$P_n(\overline{n}) = e^{-\overline{n}} \frac{\overline{n}^n}{n!} \quad \text{and,} \tag{5.8}$$

$$S(\omega, \overline{n}, n) = \frac{\gamma + \kappa(n + \overline{n})}{(\omega - (\omega_q - 2\chi n))^2 + (\gamma + \kappa(n + \overline{n}))^2/4}. \tag{5.9}$$

For the acoustic cavity parameters n, $\overline{n}$, χ, and κ, a subscript m is assumed. The measurements are constrained by independent measurements of the qubit and cavity linewidths as well as the qubits bare resonant frequency. The dispersive shift for a given mode is well constrained from the measurements without any fitting, particularly for modes $m = 5$ and $m = 7$, and is measured manually and input into the model. The strong acoustic drive creates a small background excited state population causing C_0 to grow with $\overline{n}$. This effect can be measured from the off-resonant qubit spectrum and subtracted. The drive also pushes the qubit frequency upwards at a rate of about 150 kHz per phonon, which can be determined well from the low-occupancy traces.

After inputting the independently calculated parameters and accounting for the unwanted effects of the strong acoustic drive on the qubit, the spectra are fit by varying $\overline{n}$. The resulting fits with $2\chi_{3,5,7} = 2\pi \times 500, 1050, 890$ kHz and $\kappa_{3,5,7} = 2\pi \times 200, 250, 275$ kHz agree closely with the measurements for all three modes measured. The measured spectra are not well-resolved enough to extract the phonon weights to high precision. However, the good quality of the fits to over $\overline{n} > 1$, combined with linear scaling of $\overline{n}$ with applied drive power for all three modes [Fig. 5.14] strongly suggests that the acoustic modes are in a coherent state created by the classical drive. In the absence of the acoustic drive, the qubit transition is indistinguishable from the ground state $\overline{n} = 0$. This means the total thermal occupancy of the two strongly coupled modes is below $n_{\text{th}} < 0.02$, corresponding to a temperature below 50 mk.

An unstable avoided crossing with sub-MHz coupling rate appeared intermittently between 4.312 GHz and 4.322 GHz. The frequency and coupling rate of the defect both fluctuated on a several-hour timescale. We reject data when the defect was present within a 15 MHz span around the qubit by interleaving independent diagnostics with the Stark-driven spectra and removing

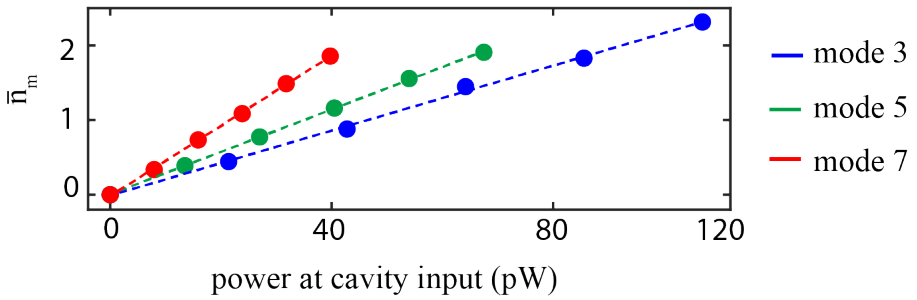

Figure 5.14: The extracted average number of phonons from the number splitting measurements increases linearly with applied power.

defect-present data in post-processing.

The device measured here demonstrates both halves of the wave-particle duality of phonons in a single device. The granularity of the dispersive shift shows that phonons come in discrete energy packets. This particle-like nature means phonons can be counted. At the same time, a single phonon's wave-like nature means that a phonon emitted from the IDT can interfere with itself, as demonstrated by the high-quality fringes in the qubit decay rate.

5.3.4 Qubit Readout

Three different types of qubit readout, all based on its dispersive interaction with the readout cavity, were performed depending on the measurement requirements. Qubit spectroscopy as a function of flux was performed using continuous wave homodyne dispersive readout backed by a flux-pumped JPA [Fig. 5.7, 5.8, 5.10]. For the qubit spectroscopy taken at ω_z, a pulsed version of this readout was used [Fig. 5.11, 5.12, 5.13]. The long qubit lifetime at this frequency results in high-contrast measurement, and the temporal separation of the qubit drive and cavity readout tones means the qubit is not dephased by the readout dispersive shift. Lastly, for broadband T_1 measurements, heterodyne bright state readout was used [Fig. 5.9] [130]. This type of readout is well-suited for measuring fast qubit decays; if the qubit is excited, the cavity effectively locks into the bright state for a time exceeding the qubit lifetime. This latching means pulses much longer

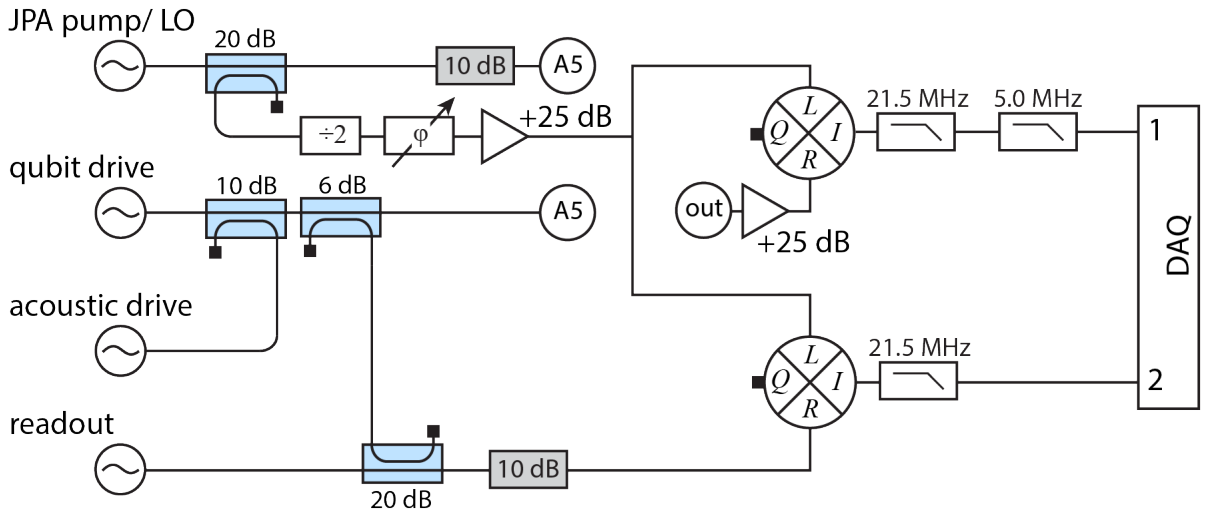

Figure 5.15: Four generator supply the tones used in the experiment. The JPA pump also supplies the LO for the experiment using a frequency divider. The relative phase between the readout tone and the LO is stabilized with a tone that bypasses the fridge and is digitized using the same DAQ.

than the qubit lifetime still give information about the initial qubit state. Still, very fast decay times are challenging to measure and lead to increased uncertainty for the shortest lifetimes measured.

In both of the homodyne measurements, two different microwave generators supplied the local oscillator and the readout tone. The generator supplying the local oscillator tone produced a tone at $2\omega_r$, which was split into a JPA pump and a frequency divider that then fed into the local oscillator of two mixers. While the two generators share a 10-MHz clock, the relative phase between them was prone to drift by about a degree a minute. The phase difference between these two generators was stabilized using a copy of the readout tone that bypasses the fridge [Fig. 5.15]. The resulting DC voltage between the LO and this bypassed tone was measured and stabilized using feedback every 15 s.

In both flux-dependent measurements, the qubit readout and drive parameters had to be calibrated over the flux region of interest in order to cleanly capture the qubit behavior. There were

three main effects to account for: the frequency-dependent filtering of the qubit drive by the readout cavity, the dependence of the readout cavity frequency on the qubit frequency, and a frequency-sensitive qubit lifetime. The filtering by the readout cavity was assumed to follow a Lorentzian, making correction simple. The qubit lifetime was modelled from preliminary measurements, and the readout cavity frequency was measured as function qubit frequency.

Chapter 6

Towards Multi-phonon Entanglement: Low-frequency, Focusing Acoustics

The previous two chapters demonstrated the unique ability of surface acoustic waves to leverage long on-chip delays to build multi-mode quantum systems with highly engineerable interactions. They also showed the challenges of coupling superconducting qubits to acoustic resonators using piezoelectricity, particularly the significant electrical losses from uncontrolled phonon generation and large participation of the surfaces, along with significant acoustic losses from phonon diffraction out of unstable, plane-parallel resonators. This chapter describes preliminary work into mitigating the dominant loss mechanisms by using lower frequency and focusing acoustic cavities as well as a flip-chip geometry to suppress unwanted phonon radiation. First, I introduce a potential experiment to create multi-phonon entanglement that draws upon the strengths of SAW systems demonstrated in this thesis and should be within reach once the described improvements are implemented.

6.1 Measurement Based Multi-mode Entanglement

Generating entanglement between the many modes of a SAW cavity would be a significant step towards using these systems for processing quantum information [131]. Here, I will describe an intuitive and straightforward way to generate entanglement between multiple cavity modes using number-resolved phonon measurements. The strategy is based on entangling two qubits which have no direct interaction; instead, a joint, projective measurement is designed that conditionally projects an initial separable state into an entangled one [132, 133, 134].

As demonstrated in the previous chapter, a single superconducting qubit coupled to a multi-

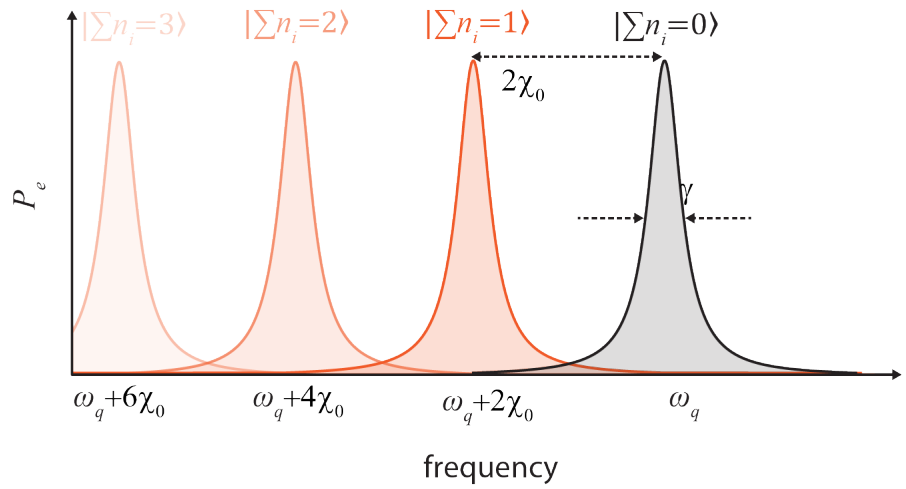

Figure 6.1: In a multi-mode system where $\chi_m = \chi_0$ for multiple modes, exciting the qubit with a number-selective π-pulse at $\omega_q - 2\chi_0$ means there is one phonon total between all of the modes. Crucially, no which-mode information is measurable, so that an initial separable state where multiple phonon modes are displaced is then projected into an entangled state.

mode SAW resonator can act as a phonon counter for several of the acoustic modes simultaneously. In the strong dispersive regime, this single phonon shift $2\chi_m$ exceeds the qubit linewidth γ, and the underlying phonon distribution can be measured using qubit spectroscopy. Similarly, if the qubit is driven with a π-pulse at frequency $\omega_q - 2n_m\chi_m$, with spectral width less than χ_m, then it will be excited if the cavity has $2n_m$ phonons in mode m. If the qubit is coupled to only a single mode, then being excited at $\omega - 2n_m\chi_m$ indicates that there must be n_m excitations in that mode.

However, in a multi-mode cavity, the qubit can have the same frequency for multiple different arrangements of phonons in the cavity. This degeneracy is particularly clear if multiple modes have the same dispersive shift, i.e. $\chi_m = \chi_0$. Then, if there are n_t phonons total, the qubit will have the same frequency $\omega_q - 2n_t\chi_0$ regardless of how the phonons are distributed in the cavity modes [Fig. 6.1]. If the qubit is excited with a π-pulse at $\omega_q - 2\chi_0$, then there must be one phonon present, but there is no which-mode information available. This mode-agnostic measurement is in many ways equivalent to measuring a photon but erasing the which-path information.

If the system is prepared in a mixed state where multiple modes have some probability of possessing one phonon, then this mode-agnostic number measurement projects the system into an entangled state. Consider a qubit coupled to two modes where $\chi_1 = \chi_2$ that is prepared in the separable state,

$$|\psi_i\rangle = |g\rangle|\alpha\alpha\rangle, \tag{6.1}$$

where $|\alpha\rangle$ is a coherent state with mean phonon number $|\alpha|^2 = \overline{n}$. If the qubit is driven with a π-pulse at $\omega_q - 2\chi_n$, then it is measured to be excited if there is one phonon total present. This one-phonon case occurs with probability $p = 2e^{-2|\alpha|^2}|\alpha|^2$ which peaks at $|\alpha|^2 = 1/2$ with $p = 1/e$. Conditioned on the qubit being successfully excited, the final state is an entangled state,

$$|\psi_f\rangle = |e\rangle\frac{\sqrt{2}}{2}(|10\rangle + |01\rangle). \tag{6.2}$$

Extending this to more modes and creating a W-state [135] requires only driving more cavity modes but the single-phonon case occurs with decreasing probability.

In contrast to other platforms, realizing a system where many cavity modes produce the same dispersive shift is natural for a qubit coupled to SAW modes. The ideal configuration to generate similar and large dispersive shifts is to have a dense region of cavity modes with coupling strength comparable to the mode spacing. This way, when the qubit is detuned from the forest of resonances by many times the coupling strength, all modes have approximately equal detuning. The dispersive shift can be adjusted to account for the small difference in detuning easily in a SAW system by modifying the IDT geometry to couple slightly more strongly to modes at the far end of the mirror bandwidth [Fig. 6.2]. The IDT would also have to be engineered to decouple the qubit from propagating phonons at its frequency of operation.

In contrast, if the resonant modes are spread out by many times their coupling strength, then a large variation in detuning would require a large variation in coupling strength, which is not only difficult to engineer, but results in reduced dispersive shifts. Thus, generating multi-phonon entanglement through mode-agnostic measurement brings together the two main virtues of SAW systems: a high density of acoustic modes with $g \sim \omega_s$ and excellent frequency domain control of

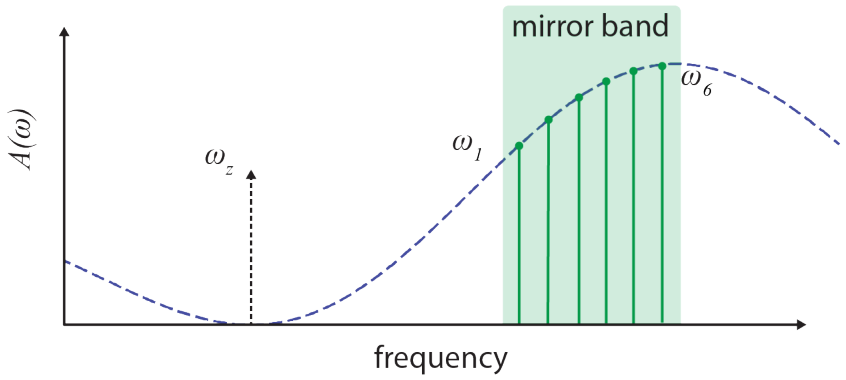

Figure 6.2: Generating entanglement between multiple modes through number-resolved but mode agnostic dispersive measurement requires engineering $\chi_m \approx \chi_0$ and no radiation to unconfined phonon modes. This configuration can be achieved with with a split-IDT qubit; the frequency-dependent coupling shuts off emission to propagating modes at ω_z while simultaneously varying the coupling to the dense forest of modes such that the more detuned resonances have appropriately stronger coupling.

the qubit-phonon interaction. Furthermore, it builds naturally on the device in the previous chapter [Ch. 5], which showed that entering the strong dispersive regime was possible, and even had two modes with dispersive shifts that were only 10% different. However, to generate and measure this multi-phonon entanglement with high fidelity requires significant improvements in both the qubit and acoustic coherence times, with a goal of $\kappa_m, \gamma < \chi_0/10$. Such improvements are the focus of the remainder of this chapter.

6.2 Possible Design Improvements

Two main changes drive the design of the next generation of devices. First, we aim to reduce the unwanted generation of unconfined phonons by removing the components other than the IDT from a piezoelectric material. This can be done either with a thin film of piezoelectric material deposited only where needed, or by using a flip-chip geometry with the IDT on a piezoelectric chip and the rest of the circuitry on a high-performance dielectric such as sapphire. Second, we move to lower frequencies ($\omega_c \approx 2\pi \times 500$ MHz). At these frequencies, electrical losses are reduced because the increased pitch of the capacitor results in a smaller participation ratio of lossy

interfaces [Sec. 4.1.2], and acoustic losses are reduced because scattering from defects and material losses should both be suppressed.

The move to lower frequencies has several other significant consequences. Fabrication of acoustic features can be done optically, as $\lambda_c \approx 6$ µm. Transmon qubits do not operate comfortably at these frequencies; their anharmonicity becomes prohibitively small, and readout becomes difficult as their dispersive shift to a readout cavity in the standard 4-8 GHz band also becomes small. Fluxonium qubits [136, 137], described shortly [Sec. 6.2.4], have $|g\rangle - |e\rangle$ transitions comfortably below 1 GHz, but have a large anharmonicity and rich energy level structure that permits high-frequency readout using higher high levels [138].

Fluxonium qubits, however, require much larger E_C and therefore much smaller shunting capacitances than transmon qubits. This reduction in capacitance requires an IDT with narrower width, which combined with the longer acoustic wavelength, results in stringent constraints on the aperture size of the IDT compared to its wavelength that would cause untenable diffraction losses in a plane-parallel cavity. Therefore, focusing cavities must be used that create a beam waist narrow enough to couple strongly to a narrow aperture IDT but that do not lose energy to diffraction. The following subsections will describe each of these improvements individually.

6.2.1 Aluminum Nitride on Sapphire

Aluminum nitride on sapphire is a promising material combination for quantum acoustics with surface acoustic waves. Sapphire is an ideal substrate for superconducting circuits, and aluminum nitride is a wide bandgap semiconductor and a strongly piezoelectric material that can be grown on sapphire using several techniques [139], with commercial applications focusing on ultraviolet LEDs and high-power electronics. Moreover, AlN can be etched away where it is not wanted [Fig. 6.3]. This attractive combination of properties has led to the successful use of AlN on sapphire to integrate transmon qubits with bulk acoustic wave resonators [67] as well as to create high-frequency surface acoustic wave cavities [140, 141], particularly for high temperature operation [142]. Additionally, the speed of sound is faster than on typical piezoelectric materials by

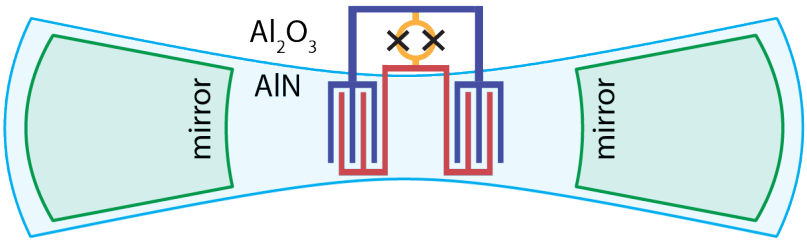

Figure 6.3: A thin film of AlN on sapphire under the IDT strongly couples the qubit and the SAW cavity but this film can be etched away under the junctions and any other circuitry to reduce unwanted phonon radiation.

approximately a factor of 2, which increases the wavelength at a given frequency, further reducing electrical and acoustic losses.

However, SAW devices fabricated and measured using C-axis AlN on C-axis sapphire from two different suppliers (500 nm film from Kyma and 350 nm from AIXaTECH) showed a weak piezoelectric response. From the external coupling rate of one port resonators, measured both warm and cold, the extracted K^2 was approximately 10^{-4}. This value is about 7 times weaker than GaAs and 30 times weaker than the expected value of 3×10^{-3}. The successful use of AlN to couple transmons to bulk acoustic waves [66] used material from Kyma, while the results using AlN for SAWs grew their own material [140, 141]. AIXaTECH claims to produce high quality, single-crystalline AlN. High quality films are necessary to reduce dielectric losses, which appear to be limiting the coherence times of state of the art devices [67]. I will note that AIXaTECH initially sent defective wafers and was slow to ship material and communicate with in general. We suspect that their AlN was in fact polycrystalline and formed multiple domains that, while uniformly oriented in the normal direction, had poorly defined in plane rotations. This type of material would couple strongly to bulk waves and out-of-plane electric fields, but not to in-plane fields and SAWs. Pursuing this strategy was halted until high performance material for SAW applications could be obtained.

6.2.2 Indium Bonded Flip Chip

Another strategy for reducing loss from uncontrolled phonon radiation is to use two separate substrates, one piezoelectric for the SAW structures and the other a high-performance dielectric for all other elements, in a flip-chip configuration. Inductive coupling between a g-mon style qubit on Si and a SAW acoustic resonator on $LiBNO_3$ was successfully used in an array of quantum acoustics experiments [70, 71, 72]. Such a strategy requires a strong piezoelectric material as the overall coupling strengths are greatly reduced by the small participation of the IDT capacitor in the qubit mode.

Reliable and low-loss galvanic connection between the two substrates that allows much stronger coupling can be achieved using In bumps [143, 144]. Using this galvanic connection, the junctions and readout resonator could be fabricated on a high-performance substrate such as sapphire and directly shunted by the IDT fabricated on piezoelectric material [Fig. 6.4]. Indium bumps on films of indium have been used to make extremely low loss microwave resonators [144], and aluminum films have been connected at DC using indium bumps with a TiN diffusion barrier, resulting in critical currents of tens of mA [143].

This process for connecting layers at DC using In bumps with a TiN diffusion barrier is currently under development in the Boulder micro-fabrication facility at NIST. Here, we are interested in using sapphire as the high-quality dielectric material and quartz for the piezoelectric top-chip. These two materials have similar coefficients of thermal expansion (a 5 mm quartz chip should contract 1.5 µm relative to a sapphire one [145]), and test resonators comprising a CPW cavity whose center conductor transfers several hundred times between a quartz and sapphire substrate using these indium bumps were cooled down and shown to have a Q of several hundred. Translating this into a two-bump loss rate for a resonator at 500 MHz with the impedance of the fluxonium qubit described shortly gives a loss rate of 5 kHz. This work is early in its development, and further refinements, particularly to the pre-bonding treatment of the indium, will likely significantly reduce this loss.

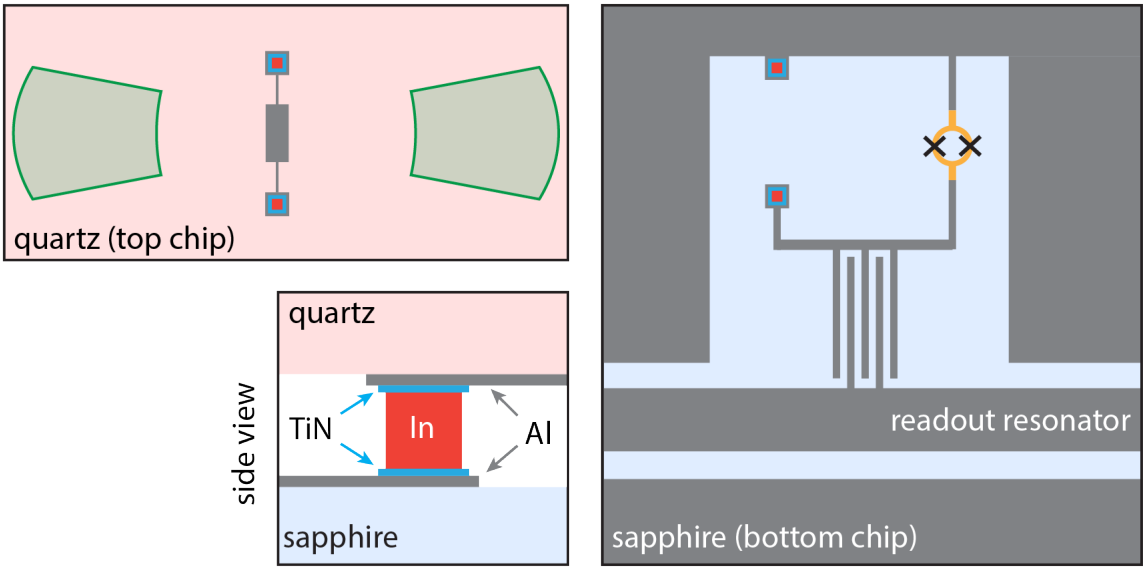

Figure 6.4: A flip chip design removes the junctions and readout resonator from the piezoelectric substrate using indium bumps to galvanically connect metal layers on separate quartz and sapphire chips. As In and Al make an undesirable intermetallic, TiN is used as a diffusion layer.

6.2.3 Lower Frequency: Improved Coherence

Increasing the wavelength of the acoustics should improve the quality factors of both the acoustic and electrical resonators. The electrical side of the argument is simple: a longer wavelength reduces the participation of the thin lossy dielectric layer at the surface of the substrate. A factor of 10 increase in the wavelength should decrease the surface participation ratio by a factor of 10. Assuming the dielectric parameters discussed earlier [Sec.4.1.2] leads to a Q limit of 6×10^4 or a linewidth of 8 kHz.

The improvement in the acoustic domain arises from reduced scattering from imperfections and reduced visco-elastic losses. If a model with constant Qf product is assumed to describe visco-elastic material loss, then lowering the frequency by a factor of 10 improves the material loss by the same amount. Loss from scattering from surface roughness and other defects with length scale below an acoustic wavelength should scale even more favorably, following the λ^{-4} dependence of

Rayleigh scattering [146]. These losses, although not believed to be limiting in current devices, will start to contribute once stable cavities are implemented that eliminate diffraction losses, as discussed in an upcoming section [Sec. 6.3].

Moving to lower frequency means that thermal occupation will be substantial. A transition frequency of 500 MHz corresponds to a temperature of 25 mK, near the achievable temperature in dilution refrigerators, meaning the thermal occupation will be significant. However, number-sensitive side-bands has been shown to be an effective cooling method for thermally occupied mechanical oscillators [74], and fluxonium, described next, can be efficiently cooled by using side-bands with the lossy and high-frequency readout resonator [138]

6.2.4 Fluxonium Qubit

The fluxonium qubit is well suited to couple to low frequency surface acoustic wave cavities. The fluxonium is formed by shunting a single, small Josephson junction by both a small capacitance and an array of large junctions that act as a high-impedance linear inductor [Fig. 6.5(a)]. The linear inductor connects the superconducting islands on either side of the small junction and thereby makes the circuit insensitive to low frequency charge noise. This circuit achieves the same charge noise insensitivity as the transmon, but does so without sacrificing anharmonicity.

Excitations of the fluxonium circuit behave like a flux particle that is trapped in a potential determined by both the linear inductor and the small junction. The Hamiltonian is given by,

$$H = 4E_c\hat{n}^2 + \frac{1}{2}E_L\hat{\phi}^2 - E_J\cos\left(\hat{\phi} - \phi_e\right) \tag{6.3}$$

where E_C is the charging energy, E_L is the linear inductor energy, E_J is the Josephson energy, $\hat{\phi}$ is the phase drop across the inductor, ϕ_e is the external flux biasing the loop, $2e\times\hat{n}$ is the displacement charge at the capacitor where $[\phi, n] = i$. Fluxonium is defined by the region where $E_L \ll E_J$ and $1 \lesssim E_J/E_C \lesssim 10$, which implies that the linear inductance must have an inductance per unit length of around $10^4\mu_0$. Such a high-impedance inductor, with minimal parasitic capacitance to ground, can also be realized using kinetic inductance [147]. Near $\phi_e = 0$, the low lying excitations

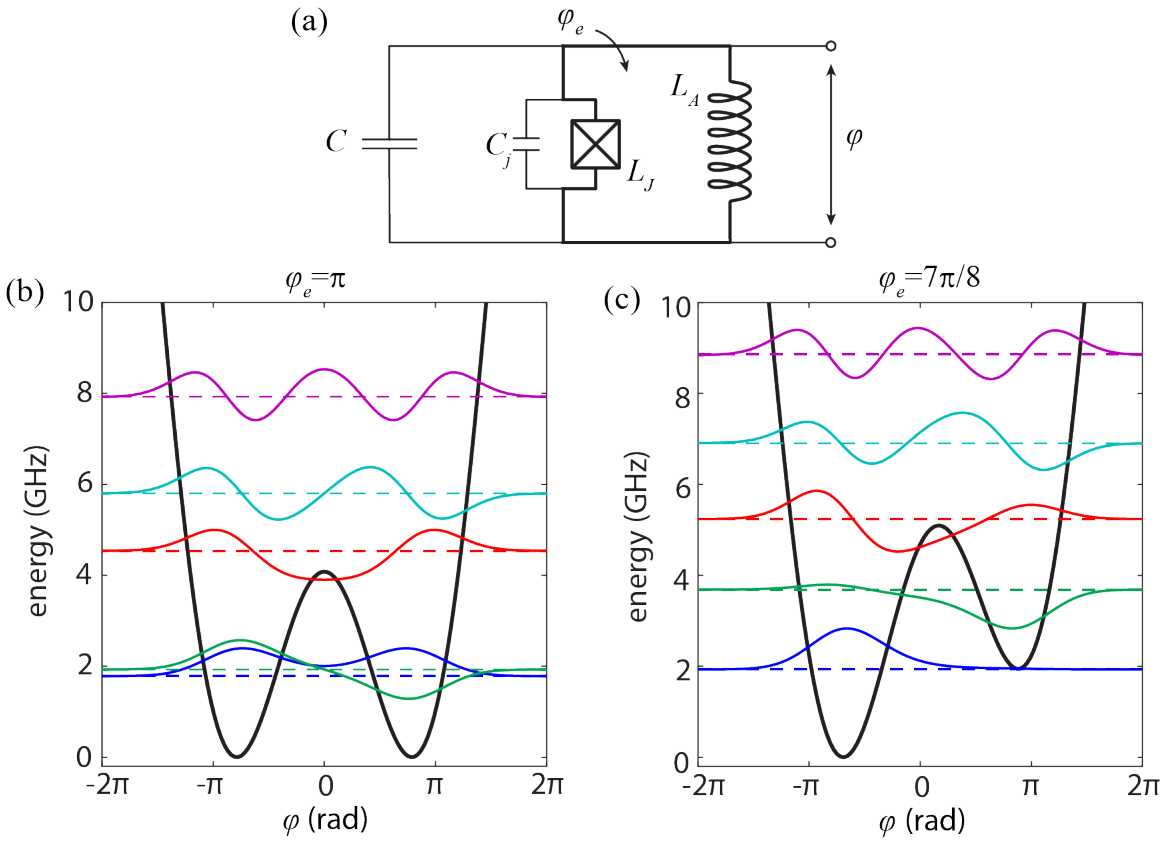

Figure 6.5: (a) The fluxonium qubit consists of a Josephson junction shorted by a large linear inductance and some small capacitance. The large array must have a high inductance per unit length and is typically made of an array of larger Josephson junctions. An external flux threaded through the junction-inductor loop (bold) biases the small junction. (b-c) The potential seen by the flux across the inductor ϕ and energy spectrum at two values of applied flux ϕ_e for $E_J/h = 4$ GHz, $E_L/h = 1$ GHz, and $E_C/h = 500$ MHz.

are plasma like, and the frequencies and transition dipoles are similar to those of a transmon.

Near flux frustration at $\phi_e = \pi$, the potential becomes a degenerate double well potential [Fig 6.5]. The lowest two energy levels are symmetric and anti-symmetric superpositions of excitations in the two wells. The splitting between these two energy levels is determined by the tunneling through the central barrier, and is typically well below 1 GHz. There are additional transition frequencies which correspond to plasma-like excitations within each well which retain a transmon-like nature and provide substantial anharmonicity. Additionally, their high frequencies and large matrix elements mean they can be coupled strongly to a resonator for readout.

The coupling strength between the low-lying fluxonium transition and a surface acoustic wave cavity depends on the $|0\rangle - |1\rangle$ charge matrix element, $\langle 0|\hat{n}|1\rangle$. This matrix element is highly sensitive to the circuit parameters and to the applied flux. In one regime, the matrix element can be heavily suppressed, resulting in protection from energy decay [148]. Here, we want to maximize this matrix element near flux frustration while maintaining a frequency at frustration of approximately 500 MHz [Fig 6.6]. For $E_C/h = 550$ MHz, $E_L/h = 1$ GHz, and $E_J/h = 3$ GHz, the matrix element near frustration is near 0.2 while the transition frequency is below 500 MHz. A fluxonium qubit on sapphire coupled to a waveguide resonator has been successfully fabricated and measured, but has not been successfully integrated yet with surface acosutic wave resonators.

Realizing these large values of E_C means the capacitance must be kept small, therefore requiring a narrow aperture IDT. This small aperture exacerbates the diffraction loss already limiting our devices, intensifying the motivation to implement focusing reflectors as discussed in the next section [Sec. 6.3]. The constraints on the IDT geometry can be relaxed by using a substrate with a weaker dielectric constant. To make larger aperture IDTs without pushing E_C down or losing coupling, we switch to quartz, which has $\epsilon_r = 3.8$ and $K^2 = 1.4 \times 10^{-3}$, compared to $\epsilon_r = 12.5$ and $K^2 = 7 \times 10^{-4}$ for GaAs.

6.3 Stable Cavities

Stable resonators are used pervasively in optical technologies. These cavities use curved reflectors to focus light and can be engineered to have negligible diffraction loss even for a tightly focusing beam. There are two differences that complicate making analogous resonators for SAWs. First, unlike free space, phonons have an anisotropic speed of sound that changes with their propagation direction [7]. This anisotropy can be strong, and has significant implication for diffraction [Eq. 2.33] and for the behavior of SAWs confined by curved mirrors. Second, unlike optical mirrors, reflectors for acoustic resonators are distributed, interacting with the acoustic wave over many wavelengths. I will first introduce the description for stable cavities in an isotropic medium before discussing these two complications.

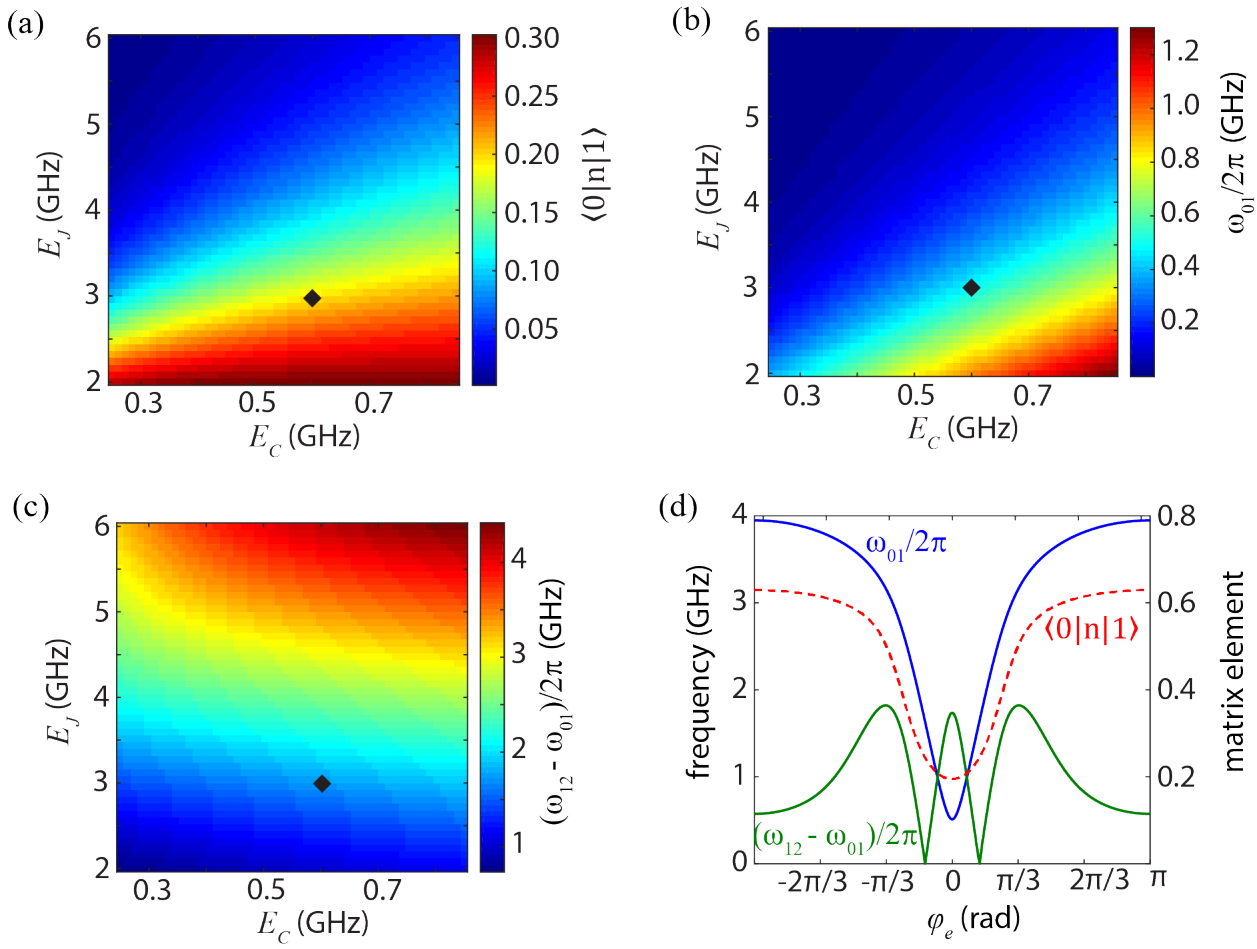

Figure 6.6: The calculated parameters of fluxonium depend strongly on (a-c) the energies and (d) external flux. At the design goal of $E_J/h = 3$ GHz, $E_C/h = 600$ MHz, and $E_L/h = 1$ GHz, the matrix element at frustration is 0.2, the ω_{01} frequency is 500 MHz, and the anharmonicity is 1.7 GHz.

6.3.1 Cavity in an Isotropic Medium

Describing the beam in a stable cavity first requires a brief description of Gaussian optics [149]. A generic stable cavity supports a Gaussian beam with wavefronts that have a position dependent curvature,

$$R(x,\theta) = \left(x + \frac{x_R^2}{x}\right), \tag{6.4}$$

where x_R is the Rayleigh length and $x = 0$ is the focus of the beam. A cavity is formed by two mirrors with curvatures R_1 and R_2 separated by length L but with unknown distance to the

focus, such that the mirrors are positioned at yet unknown positions x_1 and x_2 with $x_2 - x_1 = L$ [Fig. 6.7(a)]. The mirrors set boundary conditions, enforcing that waves incident on the mirror have wavefronts that match the mirror curvature. There are then three equations that determine the mirror positions relative to the focus as well as the Rayleigh range,

$$R(x_1) = \left(x_1 + \frac{x_R^2}{x_1}\right) = R_1 \tag{6.5}$$

$$R(x_2) = \left(x_2 + \frac{x_R^2}{x_2}\right) = R_2 \tag{6.6}$$

$$L = x_2 - x_1. \tag{6.7}$$

These equations can be inverted to find the beam parameters. These solutions are conveniently expressed in terms of the g-parameters,

$$g_1 = 1 - \frac{L}{R_1} \quad \text{and} \quad g_2 = 1 - \frac{L}{R_2}. \tag{6.8}$$

With these definitions,

$$x_R^2 = \frac{g_1 g_2 (1 - g_1 g_2)}{(g_1 + g_2 - 2 g_1 g_2)^2} L^2 \tag{6.9}$$

$$x_1 = \frac{g_2 (1 - g_1)}{g_1 + g_2 - 2 g_1 g_2} L \tag{6.10}$$

$$\tag{6.11}$$

and $x_2 = L + x_1$. The Rayleigh range is only well defined when $0 \leq g_1 g_2 \leq 1$. Indeed, this is the condition that the reflectors form a stable confined mode [Fig. 6.7(b)]. These beam parameters also determine the beam waist at the focus,

$$w_0^2 = \frac{L\lambda}{\pi} \sqrt{\frac{g_1 g_2 (1 - g_1 g_2)}{(g_1 + g_2 - 2 g_1 g_2)^2}}, \tag{6.12}$$

where w_0 is the length at which the beam amplitude falls to $1/e$ of its peak value. The beam-waist of the cavity increases moving away from the focus,

$$w(x) = w_0 \sqrt{1 + \left(\frac{x}{x_R}\right)^2}. \tag{6.13}$$

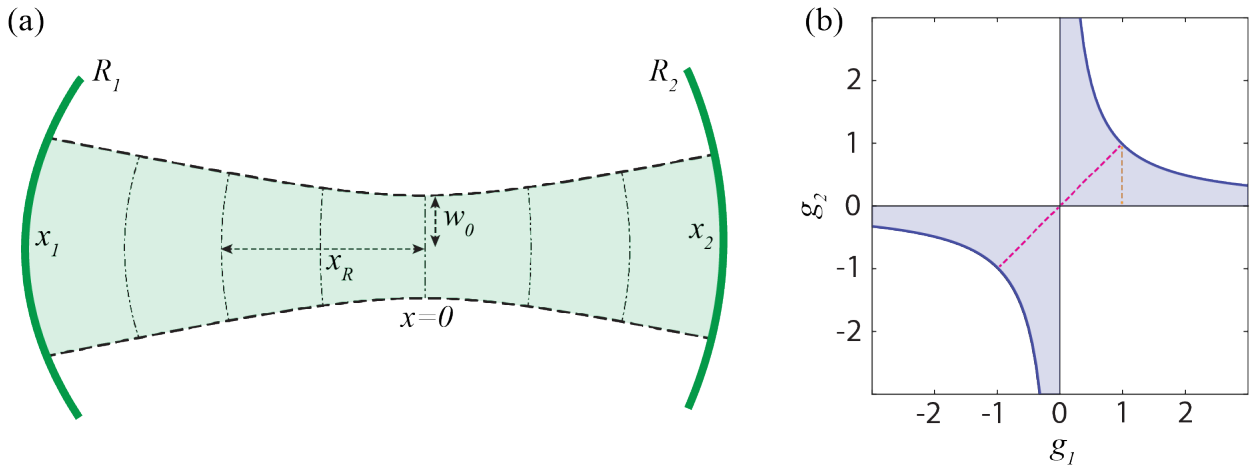

Figure 6.7: (a) A focusing cavity is defined by the curvature of two mirrors and their separation, which gives a focal position at $x = 0$, Rayleigh range x_R and beam-waist w_0. (b) The cavity is stable when $0 \leq g_1 g_2 \leq 1$ (shaded), with symmetric cavities along the diagonal (pink) and plano-convex along $g_1 = 1$, $0 \leq g_2 \leq 1$ (gold).

If the beam-waist at the mirrors, i.e. $w(x_1)$ and $w(x_2)$ is small compared to the aperture of the mirrors, then diffraction loss, which in a curved cavity is clipping of the Gaussian beam by the finite aperture of each mirror, will be negligible [149].

Even for multi-mode cavities hundreds of wavelengths long, a wide range in g-parameters results in beam-waists that are well below 5λ and sufficiently narrow for use in a fluxonium qubit. However, for the plane-parallel cavities used in the previous two chapters, $g_1 = g_2 = 1$, and the beam waist diverges, and results in the large observed loss rates.

The focusing of the beam creates a phase shift in the wavefronts called the Gouy phase [149], given by,

$$\psi(x) = \arctan\left(\frac{x}{x_R}\right). \tag{6.14}$$

Over a distance many times the Rayleigh range, the wave picks up an extra phase of π. Between the two mirrors, the wave acquires a Gouy phase given by,

$$\psi(x_1) - \psi(x_2) = \operatorname{acos}\left(\pm\sqrt{g_1 g_2}\right), \tag{6.15}$$

where the sign of arccos argument matches the sign of g-parameters. The Gouy phase acts as an

additional source of phase in the resonance condition, and therefore shifts the resonant frequency of the fundamental longitudinal modes. This overall shift is typically small and difficult to differentiate from a slightly different cavity length. However, the Gouy phase plays the dominant role in determining the relative spacing between purely longitudinal modes with index m and those with non-zero transverse mode number t. The transverse modes waves have transverse profile given by the same Gaussian waist $w(x)$ times $H_t(\sqrt{2}x/w(x))$ where H_t are the Hermite polynomials. These waves pick up an additional Gouy phase of $t\psi(x)$, so that the resonances are given by,

$$\omega_{m,t} = \left(m + (t+1)\frac{\operatorname{acos}\left(\pm\sqrt{g_1 g_2}\right)}{\pi} \right) \frac{\pi v}{L}. \tag{6.16}$$

The frequency difference between a purely longitudinal mode and its neighboring transverse modes then precisely measures the Guoy phase, and this spacing determines the product of the two g-parameters. This relationship gives a sensitive and experimentally accessible way to measure the cavity g-parameters.

6.3.2 Anisotropic Wave Velocity

The predominant difference between optical cavities and phononic ones is the anisotropy of the speed of sound. Piezoelectric materials are necessarily anisotropic, as piezoelectricity requires the crystal break inversion symmetry. There are two methods to account for this asymmetry: one applied to focusing SAWs on GaAs based on the angle dependence of the SAW group velocity [150, 151], and another implemented on high-Q focusing bulk acoustic wave resonators based on a paraxial approximation of the angle-dependent phase velocity [152, 122]. The group velocity method was demonstrated in the most relevant application, and claims to out-perform the paraxial approximation when attempting to make an IDT with a tight focus, and so this is the method used to design the focusing cavities discussed here. The paraxial approximation, on the other hand, can make a wider set of predictions, and preliminary analysis suggests that it can better account for the observed focusing behavior described further in the following section [Sec. 6.4.2].

6.3.2.1 Group Velocity Approach

The concept behind the group-velocity approach to focusing SAWs in an anisotropic medium can be understood intuitively by considering the strain field generated by a point source. A strain pulse generated from a point source will radiate away, carrying power outward at $v_g(\theta)$, the angle-dependent group velocity [151]. By time reversal, a source that excites a wave-front that matches the radiated pattern will focus back to a diffraction limited point. Thus, these sources, such as mirror elements, that attempt to focus SAWs at radius R_0 should have an angle-dependent curvature,

$$R(\theta) = R_0 v_g(\theta)/v_g(0). \tag{6.17}$$

To determine this angle-dependent group velocity, first the phase velocity $v_p(\theta)$ of ST quartz is determined using COMSOL simulations [Fig. 6.8(a-b)], and converted to group velocity by first determining the power flow angle,

$$\xi = \arctan\left(\frac{dv_p}{d\theta}\frac{1}{v_p(\theta)}\right), \tag{6.18}$$

which then determines $v_g = v_p/\cos(\xi)$. A difference in phase and group velocity, resulting from an angular dependence in v_p, therefore requires power flow that is not orthogonal to the wave fronts [Fig. 6.8(c)]. The diffraction parameter γ used earlier [Eq. 2.33] can be found as $\gamma = d\xi/d\theta$. Note that a well chosen crystal cut and propagation direction can result in both $\xi = 0$ and $\gamma = -1$, meaning waves do not diffract to first order [82, 7]. This method for reducing diffraction losses is also under investigation at this time, with promising initial measurements already taken.

The wavefronts in the cavity are then assumed to follow the angle-dependent curvature,

$$R(x,\theta) = \left(x + \frac{x_R^2}{x}\right) v_g(\theta)/v_g(0). \tag{6.19}$$

Scaling all of the elements to follow this angle-dependence results in a consistent cavity, where the g-parameters are defined using their R_0 values.

The written radius of curvature approximated at small angles R_w can differ greatly from R_0 because the second derivative of the group velocity effectively rescales the curvature. At small

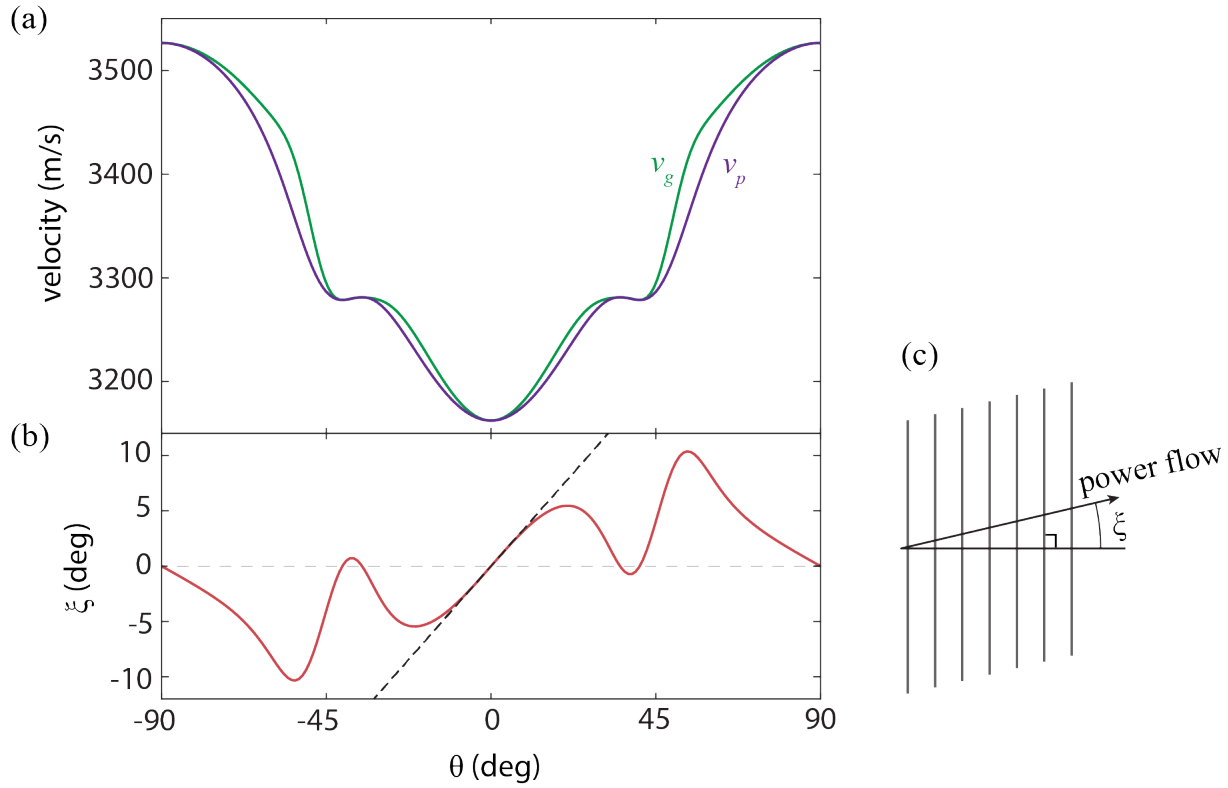

Figure 6.8: (a) The phase v_p and group v_g velocities on quartz based on Comsol simulations of v_p. (b) The power flow angle ξ, depicted in (c), as a function of angle. The paraxial approximation is based on the slope of ξ at $\theta = 0$ (dashed).

angle,

$$R_w = R_0 \left(1 - \frac{v_g''(0)}{v_g(0)}\right)^{-1} \tag{6.20}$$

where $v_g''(0)$ is the second derivative of v_g with respect to angle evaluated at $\theta = 0$. On quartz, $v_g''(0) = 0.51$, which means that the written designs have radii of curvature approximated at small angle that is nearly twice the effective curvature seen by the acoustic wave.

6.3.2.2 Paraxial Approximation

An alternative approach is to approximate the effect of the anisotropy by an rescaling factor μ by the quadratic term in the angular dependence of the phase velocity. This factor is given by $\mu = 1 - v_p''(0)/v_p(0)$, which on ST-X quartz gives $\mu = 0.63$ according to COMSOL simulations

[Fig. 6.8(b)]. This approximation leads to several more analytical expressions given below that capture how a Gaussian beam is modified by asymmetry, but there is evidence [151] that this approximation leads to degraded focusing behavior.

The curvature of the beam is scaled by μ [122], such that,

$$R(x) = \left(x + \frac{x_R^2}{x}\right)\frac{1}{\mu}. \tag{6.21}$$

This simple scaling can then be used to derive that the g-parameters,

$$g_1 = 1 - \frac{L}{\mu R_1} \quad \text{and} \quad g_2 = 1 - \frac{L}{\mu R_2}, \tag{6.22}$$

where R_1 and R_2 are the written curvatures, as well as the modified beam waist,

$$w_0^2 = \frac{L\lambda}{\mu\pi}\sqrt{\frac{g_1 g_2(1-g_1 g_2)}{(g_1+g_2-2g_1 g_2)^2}}. \tag{6.23}$$

The other cavity parameters, such as the Rayleigh range and the Gouy phase, depend the g-parameters in the same way as the isotropic case.

6.3.3 Distributed Mirrors and Curved IDTs

Stable cavities for SAWs do not have access to localized reflectors. The analysis derived for quasi-1D acoustic reflectors in Sec. 2.2.1 still applies to focusing cavities. In contrast to what is typically encountered with optical Bragg reflectors, in the case of SAWs the significant penetration into the mirrors compared to the Rayleigh length means that the elements must change curvature with position.

The cavities used here are constructed by first choosing the length and g-parameters of the cavity. This design then sets the radius of curvature for all points within the cavity, as well as those outside, to follow Eq. 6.19. The mirror elements are chosen to follow this curvature, with the first elements placed such that the distance between the mirrors is equal to the designed length minus twice the penetration length [Fig. 6.11]. This consistency means that regardless of the penetration length seen by a wave, the curvature of the element at that length will give the same beam parameters, only with a different cavity length.

The IDT fingers are curved based on their position to follow the same distribution. The width of both of the mirrors and the IDT is some scalar factor times the beam waist at their position, following Eq. 6.13. Finally, the spacing between the elements is adjusted to compensate for the Gouy phase.

6.4 Testing Stable Cavities on Quartz

The performance of stable SAW resonators on quartz was investigated by fabricating an array of cavities and probing their electrical response. Moving to lower frequency makes optical lithography sufficient to define the features. These techniques are convenient at wafer-scale, which combined with a microwave probe station enables many devices to be fabricated and measured quickly. The goal of these tests was to make resonators that focused SAWs to a beam waist of near 5λ to be compatible with the constraints on the capacitor size imposed by fluxonium while suppressing the diffraction losses that limited previous devices.

6.4.1 Cavity Design

The cavities investigated here are primarily two-port plano-convex cavities with one transducer near either reflector. This design is attractive partially because it is simple, as there is only one curvature that matters, and the achievable beam-waist is quite small. In most designs, the "flat" mirror does in fact have some curvature to move the focal point outside the Bragg stack.

The plano-convex design also offers a stronger coupling to more modes than a symmetric one. In both designs, the qubit IDT must be located at the focus of the cavity, which is in the center for a symmetric cavity and near the flat mirror in a plano-convex design. If the qubit is designed to couple to all of the modes of a symmetric resonator, then it must be shifted from the center by $\lambda/8$, which reduces its coupling by $\sqrt{2}$. Alternatively, to achieve the same mode density, the cavity could be made twice as long, but this has exactly the same effect on the coupling rate. In a plano-convex design, the qubit IDT is near the mirrors where the standing waves have nearly the same phase [Fig. 6.9(a)], particularly for modes near the center of the mirror bandwidth, leading

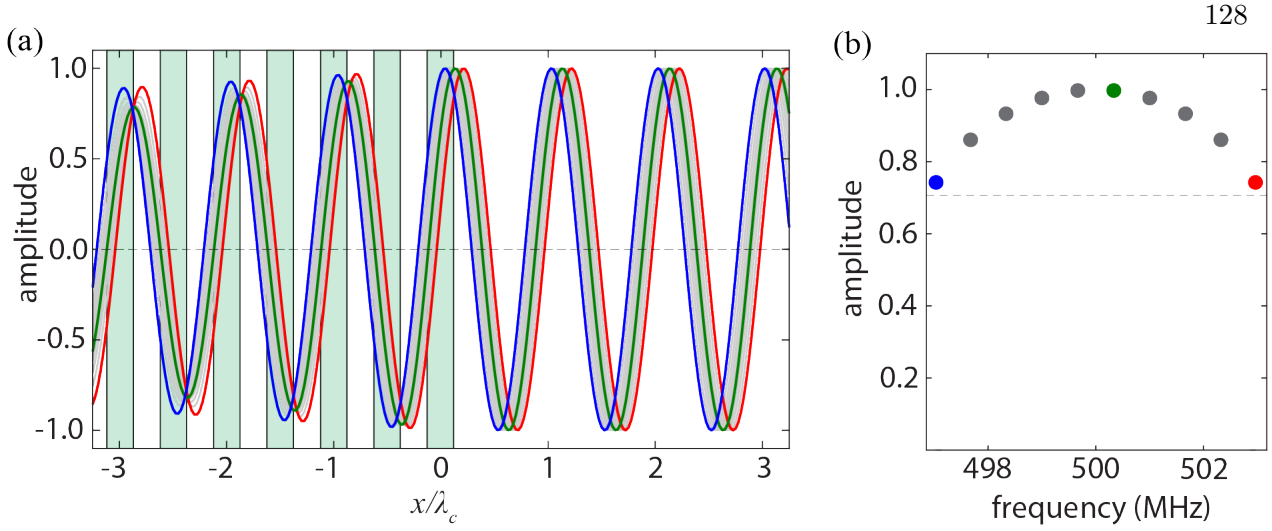

Figure 6.9: (a) The SAW standing wave [Eq. 2.32] near the mirror are shifted by the phase of the mirrors, but this shift is small so the anti-nodes are all close together. Modes at the edge of the mirror bandwidth (red/blue) have the largest deviation. (b) An IDT with center $(5+3/8)\lambda$ away from the mirror will couple to all modes strongly compared to the $\sqrt{2}$ penalty paid for coupling to all modes of a symmetric cavity by offsetting an IDT at the center of a symmetric cavity $\lambda/8$ (dashed).

to strong coupling to all of the modes of interest [Fig. 6.9(b)].

This same design with a flat IDT near one mirror could also be realized with a high curvature design with focusing parameters of equal magnitude but opposite sign as the quasi plano-convex case. While this design would achieve a slightly smaller beam-waist, designing both mirrors with negative g-parameters requires higher curvature reflectors and results in a cavity stability that is more sensitive to the crystal anisotropy.

6.4.2 Focusing Tests

We test the focusing behavior of an array of SAW cavities with widely varied curvature by measuring the spacing between purely longitudinal modes and their associated transverse resonances. The relative frequency spacing between longitudinal modes and those with non-zero mode number depends only on the g-parameters of the device [Eq. 6.16].

The fabrication was done using optical lithography. Aluminum was first sputtered onto the

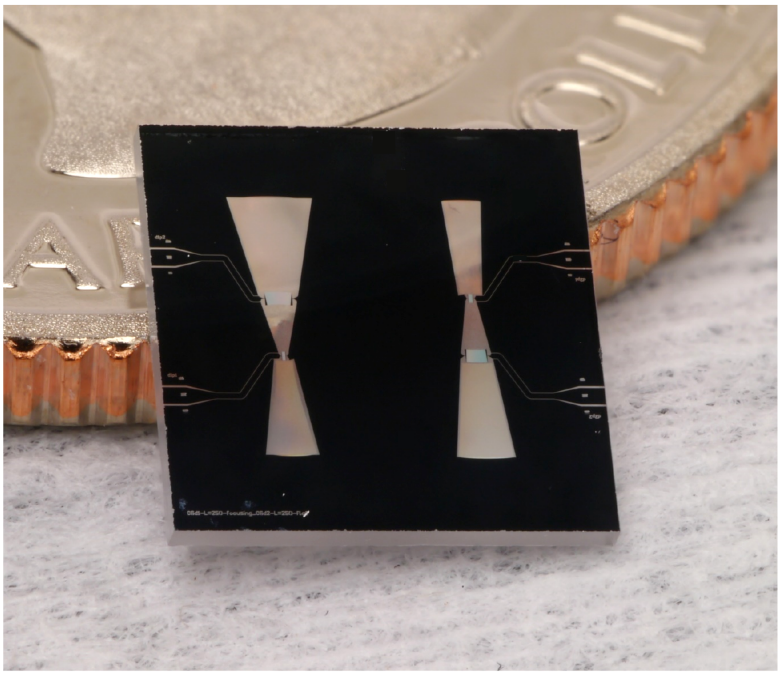

Figure 6.10: The focusing SAW cavities, shown here resting on a quarter, are fabricated of Al on quartz with etched mirrors. They are probed wafer scale, and the scratches from the probe station are visible on the bond pads after dicing.

wafer to create a 25 nm film. The aluminum was then etched using a wet-process to define the IDTs and the transmission lines before the mirror elements were etched into the quartz using a plasma etch. Representative devices are pictured in Fig. 6.10 and shown schematically in Fig. 6.11.

These devices all had the same length, and were designed to produce a somewhat uniform distribution of transverse mode spacing [Fig. 6.12(a)]. The width of the reflectors was chosen to be 3 times the beam-waist with an expected penetration length of 70 µm from $r_s = 2.1\%$. There are two IDTs in the cavity, both with finger overlap 1.5 times the waist. The narrow IDT width results in a weak coupling strength that is nonetheless sufficient to measure the acoustic spectra with a microwave probe station at room temperature.

The measurements show a uniform longitudinal mode spectra between the many devices with a clear migration upwards of the transverse mode as the curvature of the reflectors is increased [Fig. 6.12(b)]. The difference in the depths of the reflection dips on resonance arises primarily from

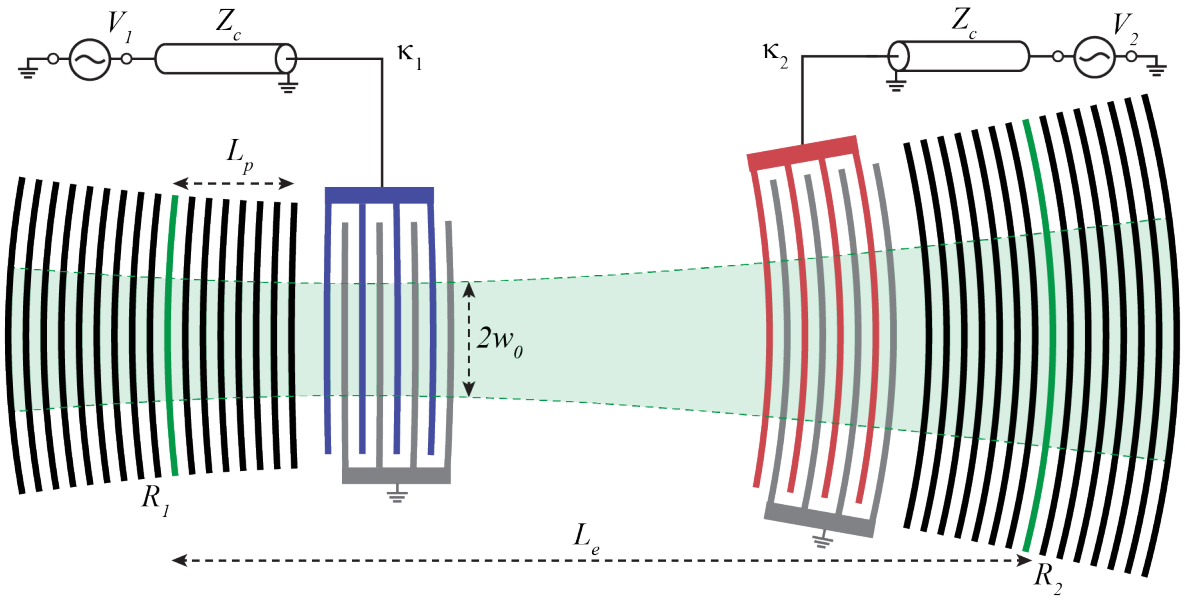

Figure 6.11: The SAW cavities are designed to be near plano-convex with two IDTs, one near the curved mirror and the other near the flat mirror. The width of the IDTs and mirrors are set to be proportional to the predicted beam waist. The curvature of the mirrors and length of the cavity is set by the element L_p into the array, and the "flat" mirror has some non-zero curvature so that the focus occurs just in front of its first element.

the differences in external coupling rate as the width of the measurement IDT follows the minimum expected beam-waist. The transverse modes are low-Q because they have a wider beam-waist than the purely longitudinal modes, and there is significant clipping at the finite-width reflectors.

The extracted transverse mode spacing relative to the free spectral range follows the prediction but only if the mirror radii of curvature are rescaled by a factor of 1.4 [Fig. 6.13]. Interestingly, preliminary calculations indicate that this rescaling is not required if we approximate the mirror elements as circles and then use the paraxial approximation to calculate the effective g-parameters and transverse mode spacings [Fig. 6.13]. Regardless, the transverse mode spacings strongly indicate that these SAW cavities are indeed focusing. However, this measurement is only an inference, and direct measurements of the acoustic standing wave would illuminate many details of the acoustic modes that are not apparent from cavity spectroscopy.

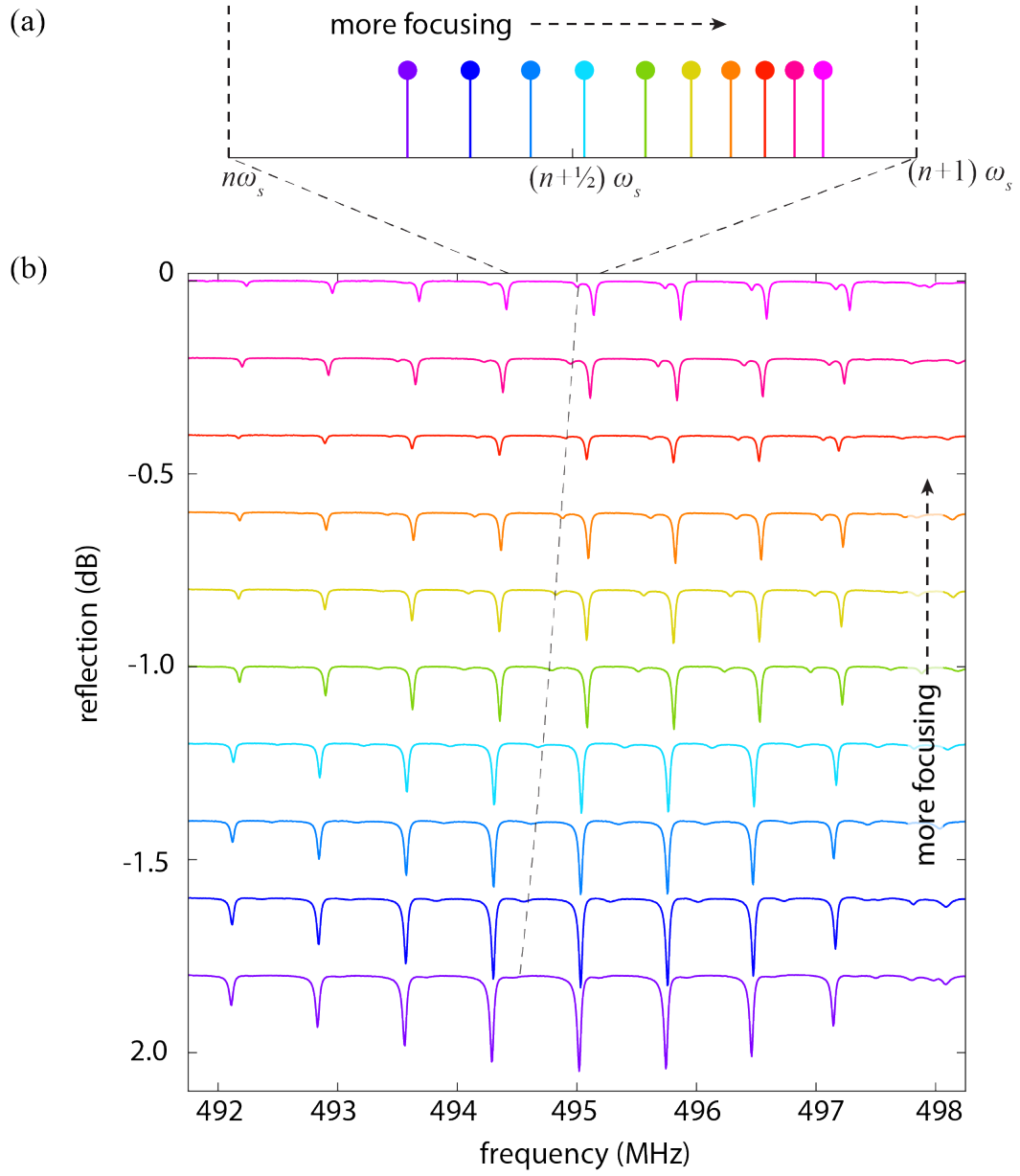

Figure 6.12: (a) An array of 10 devices were designed with varying curvatures such that the expected transverse mode frequency spanned a free spectral range. (b) The measured spectra show clear longitudinal modes that are nearly independent of the focusing parameters across a wide range in curvatures. The transverse modes migrate from the high frequency shoulder for weakly focusing cavities to the low frequency shoulder for strongly focusing ones (dashed).

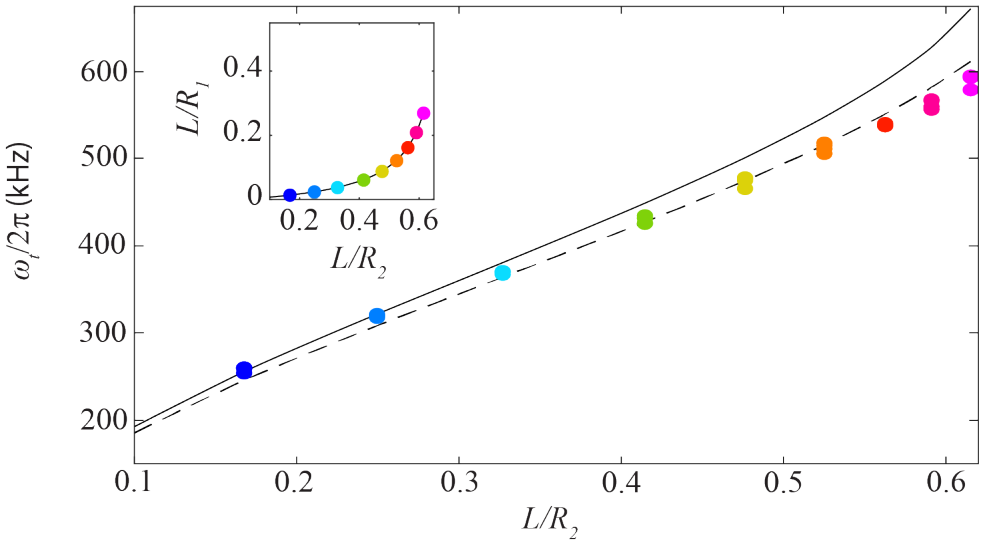

Figure 6.13: The extracted transverse mode frequency spacings from the previous device closely follow the designed values, including a phenomenological radius rescaling factor of 1.4 (dashed). A paraxial approximation with $\mu = 0.63$, where the mirrors are approximated as circular, agrees well at low curvature but deviates at higher values (solid). The flat mirror curvature R_1 changes between devices to keep the focus in front of the mirror (inset).

6.4.3 Resonator Vibrometry

Vibrometry provides a direct method of imaging the standing wave of the SAW cavities. These methods shine focused laser light on the sample, and acoustic oscillations modulate the reflected light [153]. Current commercial technology produced by Polytec can resolve pm displacements at hundreds of MHz with a micron spot size and in a near mm^2 field of view. This resolution is sufficient to directly image the SAW resonators we are interested in, although such multi-mode cavities have lengths that exceed the measurement field of view.

Polytec measured two acoustic cavities that we fabricated, one more strongly focusing, to provide a detailed picture of the standing waves in the cavity. The cavity was driven with a chirped tone during measurement which provides a broadband excitation of the acoustic cavity. The chirp was slow enough, however, that the acoustic cavity modes could ring up fully while the drive was swept across resonance. Measurements of several segments of each resonator were taken, each many

wavelengths in spatial extent.

Preliminary analysis of this large data set has provided direct confirmation that the cavities do indeed focus [Fig. 6.14(a)]. The wavefronts are well defined, and the transverse beam profile is well fit by a Gaussian with a waist that is approximately the predicted size. The resonance that we had inferred had non-zero transverse mode number from spectroscopy show the expected Hermite-Gaussian transverse profile with no free parameters for the $t = 2$ mode [Fig. 6.14(d)]. An IDT could be designed to decouple from this transverse mode if the SAW amplitude integrated over the IDT width was zero. Additionally, the curvature of the wave does match the mirror elements, suggesting no nefarious effects are present from a potentially angle-dependent reflectivity per element. For the more focusing device not shown here, the somewhat clean spectrum belies the reality that the transverse modes do not go away for strongly focusing devices, but simply become spectrally indistinct from the transverse modes.

Further analysis of this large data set faces several challenges. Neither device provides clear simultaneous measurements of both curvature and beamwaist; the wave-fronts in the less focusing device are too flat to precisely extract a curvature, while the transverse profile in the more focusing device is a mixture of purely longitudinal and various transverse modes without a well-defined waist.

6.4.4 High-Q Focusing Cavities

In addition to creating a narrow beam-waist, these focusing cavities were implemented to increase the quality factor of the acoustic resonators. At room temperature, the internal linewidth of SAW cavities is typically dominated by visco-elasticity. Additionally, the focusing itself will likely change as the elasticity tensor of quartz changes with temperature [154].

The cryogenic performance of these focusing resonators shows that diffraction loss is indeed suppressed. A characteristic plano-convex resonator with was cooled down to 20 mK, and its measured spectra shows many high-Q resonances over the mirror bandwidth [Fig. 6.15]. Interestingly, the Q improves towards the upper edge of the band, an effect likely related to how the strain is

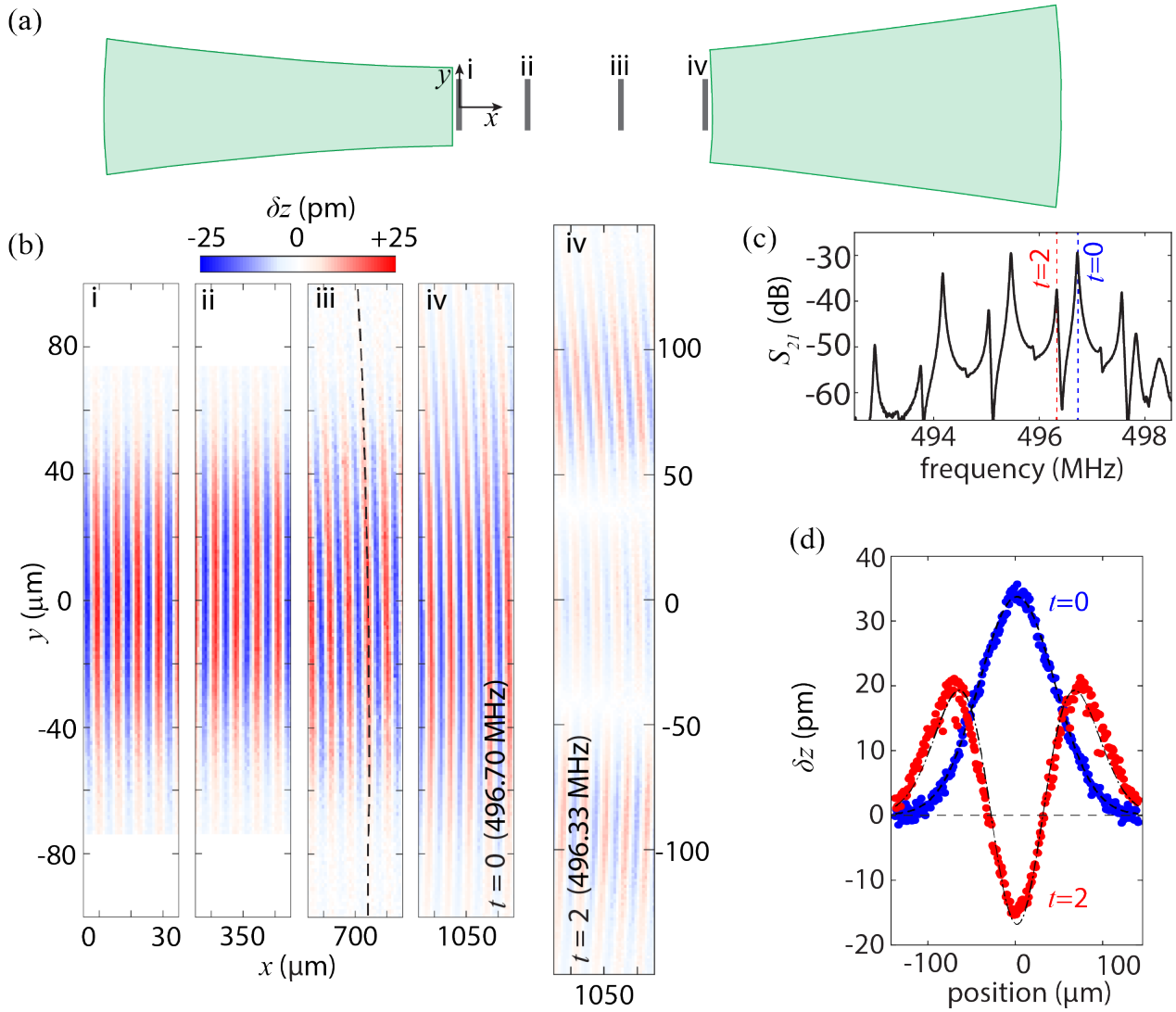

Figure 6.14: (a) The standing waves in the weakly focusing cavity ($g_1 = 0.83$, and $g_2 = 0.34$) are measured at several locations. (b) The measured displacement at 496.70 MHz show clear wave-fronts with increasing beam waist and curvature approaching the curved mirror. The measured displacement of the transverse mode at 496.33 MHz shows clear nodes in the transverse direction. (c) The measured transmission spectrum through the cavity, with peaks associated with both purely longitudinal ($t = 0$) as well as well-separated, 2nd order transverse modes ($t = 2$). (c) Cuts across the wave-fronts show a Gaussian fundamental mode, whose beam-waist can be used to predict the $t = 2$ transverse mode profile with good accuracy.

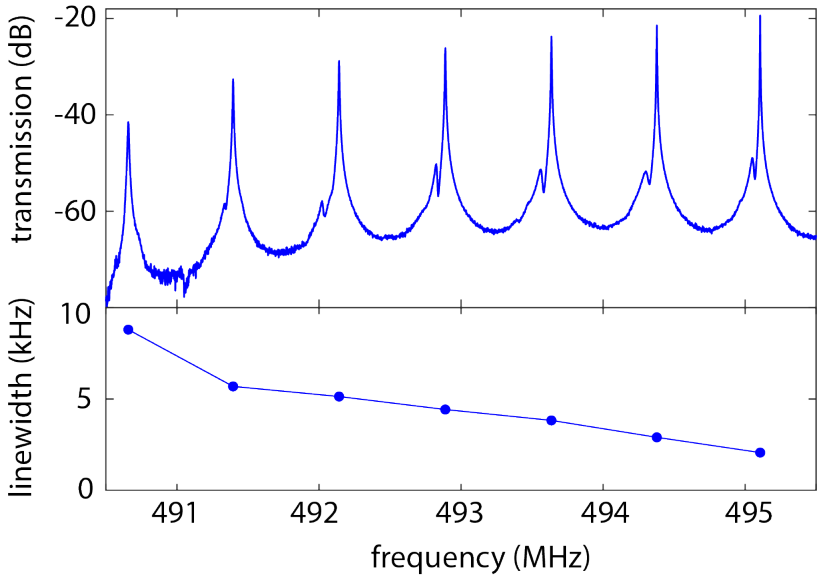

Figure 6.15: The transmission spectrum of a highly focusing cavity shows multiple high-Q resonances with linewidths decreasing across the mirror bandwidth to below 2 kHz. Transverse modes are visible on the low-frequency shoulder of the main, longitudinal resonances but with relatively small amplitude.

localized relative to the mirror elements [79] as depicted in Fig. 6.9(a). The promincence of this effect suggests that the new limit on device coherence is scattering from the mirror elements into the bulk, although this requires further investigation.

Crucially, the highest frequency resonance has a linewidth of below 2 kHz, which corresponds to a factor of 100 increase in lifetime and a factor of 10 increase in Q, and indicates that diffraction is no longer the limiting loss in the cavities. Such a multi-mode, high-Q resonator with a narrow beam-waist is well positioned to be useful immediately in hybrid quantum acoustics experiments with surface acoustic waves, potentially to generate multi-mode entanglement through joint, projective measurement.

Chapter 7

Conclusion and Outlook

In this thesis, I demonstrated that superconducting circuits can be coupled to multi-mode SAW cavities, reaching both the strong, multi-mode coupling regime where the qubit-cavity exchange rate exceeded the cavity mode spacing, and the strong dispersive regime, where the single-phonon dispersive shift exceeds the intrinsic decay rates of the system. These results not only confirm that quantum acoustics with surface acoustic waves is well described by Jaynes-Cummings physics, but they also highlight the unique strengths of surface acoustic waves: to create long delays in a compact space, both to realize high densities of resonant modes and also to precisely engineer the qubit-phonon interaction strength in the frequency domain. Together, these abilities make quantum acoustics with surface acoustic waves a promising platform for exploring a deeply multi-mode analogy of circuit quantum electrodynamics, but with sound.

Future experiments would greatly benefit from improved coherence times. I have shown that the dominant acoustic loss mechanism, phonon diffraction loss from an unstable, plane-parallel cavity, can be eliminated by implementing curved reflectors. On the electrical side, moving to lower frequencies and using a flip-chip geometry should improve the coherence of the superconducting qubit. Such improvements are likely sufficient to enable a range of exciting experiments, including observation of phonon jumps [105] and entangling multiple phonon modes together through either 4-wave mixing [26], side-bands [25], or joint-projective measurement [134]. Reconstructing the multi-mode density matrix will be crucial to verifying this entanglement, and could follow the demonstrations from cQED [27]. For building a quantum random access memory out of SAW

modes, the spacing between resonances must be substantially non-uniform [26], which could be achieved using Bragg stacks with a frequency-dependent delay, or by inserting third reflector centered in the cavity with a frequency-dependent reflectivity to create pairs of resonances with a frequency-dependent splitting.

The outlook for further improvements of the performance metrics is promising. The coupling strength could be improved by an order of magnitude using a stronger piezoelectric material. This increased coupling strength could also be traded for increased qubit coherence by reducing the participation of the piezoelectric material. However, coupling to surface acoustic waves will always entail a significant amount of electrical energy stored in the surface where dielectric losses are largest, and the long-term prospects for improving the device performance are significantly better for the acoustic cavities [121]. Identifying the next dominant loss mechanism is of high priority. If this loss comes from the mirror elements as is currently suspected, then this can be reduced by engineering the strain profile at the mirrors using a tapered geometry or modifying the density of states of bulk modes by fabricating the resonators on a Bragg stack into the substrate or suspending the whole resonator [155].

Bibliography

[1] A. G. J. MacFarlane, J. P. Dowling, and G. J. Milburn, "Quantum technology: the second quantum revolution," Philosophical Transactions of the Royal Society of London. Series A: Mathematical, Physical and Engineering Sciences, vol. 361, no. 1809, pp. 1655–1674, Aug. 2003, publisher: Royal Society. [Online]. Available: https://royalsocietypublishing.org/doi/10.1098/rsta.2003.1227

[2] W. J. H. Andrewes, "A Chronicle Of Timekeeping." [Online]. Available: https://www.scientificamerican.com/article/a-chronicle-of-timekeeping-2006-02/

[3] H. Cavendish, "XXI. Experiments to determine the density of the earth," Philosophical Transactions of the Royal Society of London, vol. 88, pp. 469–526, Jan. 1798, publisher: Royal Society. [Online]. Available: https://royalsocietypublishing.org/doi/10.1098/rstl.1798.0022

[4] C. Xue, J.-P. Liu, Q. Li, J.-F. Wu, S.-Q. Yang, Q. Liu, C.-G. Shao, L.-C. Tu, Z.-K. Hu, and J. Luo, "Precision measurement of the Newtonian gravitational constant," National Science Review, vol. 7, no. 12, pp. 1803–1817, Dec. 2020. [Online]. Available: https://doi.org/10.1093/nsr/nwaa165

[5] W. H. King, "Piezoelectric Sorption Detector." Analytical Chemistry, vol. 36, no. 9, pp. 1735–1739, Aug. 1964, publisher: American Chemical Society. [Online]. Available: https://doi.org/10.1021/ac60215a012

[6] L. Rayleigh, "On Waves Propagated along the Plane Surface of an Elastic Solid," Proceedings of the London Mathematical Society, vol. s1-17, no. 1, pp. 4–11, 1885, _eprint: https://londmathsoc.onlinelibrary.wiley.com/doi/pdf/10.1112/plms/s1-17.1.4. [Online]. Available: https://londmathsoc.onlinelibrary.wiley.com/doi/abs/10.1112/plms/s1-17.1.4

[7] D. P. Morgan, Surface Acoustic Wave Filters. Amsterdam: Elsevier, 2007.

[8] P. Debye, "Zur Theorie der spezifischen Wärmen," Annalen der Physik, vol. 344, no. 14, pp. 789–839, 1912, _eprint: https://onlinelibrary.wiley.com/doi/pdf/10.1002/andp.19123441404. [Online]. Available: https://onlinelibrary.wiley.com/doi/abs/10.1002/andp.19123441404

[9] L. S. C. a. V. Collaboration, "Observation of Gravitational Waves from a Binary Black Hole Merger," Physical Review Letters, vol. 116, no. 6, p. 061102, Feb. 2016, publisher: American Physical Society. [Online]. Available: https://link.aps.org/doi/10.1103/PhysRevLett.116.061102

[10] V. B. Braginsky, Y. I. Vorontsov, and K. S. Thorne, "Quantum Nondemolition Measurements," Science, vol. 209, no. 4456, pp. 547–557, Aug. 1980, publisher: American Association for the Advancement of Science Section: Articles. [Online]. Available: https://science.sciencemag.org/content/209/4456/547

[11] C. M. Caves, K. S. Thorne, R. W. P. Drever, V. D. Sandberg, and M. Zimmermann, "On the measurement of a weak classical force coupled to a quantum-mechanical oscillator. I. Issues of principle," Reviews of Modern Physics, vol. 52, no. 2, pp. 341–392, Apr. 1980, publisher: American Physical Society. [Online]. Available: https://link.aps.org/doi/10.1103/RevModPhys.52.341

[12] D. Martynov et al, "Sensitivity of the Advanced LIGO detectors at the beginning of gravitational wave astronomy," Physical Review D, vol. 93, no. 11, p. 112004, Jun. 2016, publisher: American Physical Society. [Online]. Available: https://link.aps.org/doi/10.1103/PhysRevD.93.112004

[13] M. Tse et al, "Quantum-Enhanced Advanced LIGO Detectors in the Era of Gravitational-Wave Astronomy," Physical Review Letters, vol. 123, no. 23, p. 231107, Dec. 2019, publisher: American Physical Society. [Online]. Available: https://link.aps.org/doi/10.1103/PhysRevLett.123.231107

[14] A. Bassi, K. Lochan, S. Satin, T. P. Singh, and H. Ulbricht, "Models of wave-function collapse, underlying theories, and experimental tests," Reviews of Modern Physics, vol. 85, no. 2, pp. 471–527, Apr. 2013, publisher: American Physical Society. [Online]. Available: https://link.aps.org/doi/10.1103/RevModPhys.85.471

[15] C. Degen, F. Reinhard, and P. Cappellaro, "Quantum sensing," Reviews of Modern Physics, vol. 89, no. 3, p. 035002, Jul. 2017, publisher: American Physical Society. [Online]. Available: https://link.aps.org/doi/10.1103/RevModPhys.89.035002

[16] A. P. Higginbotham, P. S. Burns, M. D. Urmey, R. W. Peterson, N. S. Kampel, B. M. Brubaker, G. Smith, K. W. Lehnert, and C. A. Regal, "Harnessing electro-optic correlations in an efficient mechanical converter," Nature Physics, vol. 14, no. 10, pp. 1038–1042, Oct. 2018, number: 10 Publisher: Nature Publishing Group. [Online]. Available: https://www.nature.com/articles/s41567-018-0210-0

[17] W. Jiang, C. J. Sarabalis, Y. D. Dahmani, R. N. Patel, F. M. Mayor, T. P. McKenna, R. Van Laer, and A. H. Safavi-Naeini, "Efficient bidirectional piezo-optomechanical transduction between microwave and optical frequency," Nature Communications, vol. 11, no. 1, p. 1166, Mar. 2020, number: 1 Publisher: Nature Publishing Group. [Online]. Available: https://www.nature.com/articles/s41467-020-14863-3

[18] G. Arnold, M. Wulf, S. Barzanjeh, E. S. Redchenko, A. Rueda, W. J. Hease, F. Hassani, and J. M. Fink, "Converting microwave and telecom photons with a silicon photonic nanomechanical interface," Nature Communications, vol. 11, no. 1, p. 4460, Sep. 2020, number: 1 Publisher: Nature Publishing Group. [Online]. Available: https://www.nature.com/articles/s41467-020-18269-z

[19] Y. Tsaturyan, A. Barg, E. S. Polzik, and A. Schliesser, "Ultracoherent nanomechanical resonators via soft clamping and dissipation dilution," Nature Nanotechnology, vol. 12, no. 8,

pp. 776–783, Aug. 2017, bandiera_abtest: a Cg_type: Nature Research Journals Number: 8 Primary_atype: Research Publisher: Nature Publishing Group Subject_term: Mechanical properties;Quantum mechanics;Sensors Subject_term_id: mechanical-properties;quantum-mechanics;sensors. [Online]. Available: https://www.nature.com/articles/nnano.2017.101

[20] H. Ren, M. H. Matheny, G. S. MacCabe, J. Luo, H. Pfeifer, M. Mirhosseini, and O. Painter, "Two-dimensional optomechanical crystal cavity with high quantum cooperativity," Nature Communications, vol. 11, no. 1, p. 3373, Jul. 2020, number: 1 Publisher: Nature Publishing Group. [Online]. Available: https://www.nature.com/articles/s41467-020-17182-9

[21] T. A. Palomaki, J. W. Harlow, J. D. Teufel, R. W. Simmonds, and K. W. Lehnert, "Coherent state transfer between itinerant microwave fields and a mechanical oscillator," Nature, vol. 495, no. 7440, pp. 210–214, Mar. 2013.

[22] A. P. Reed, K. H. Mayer, J. D. Teufel, L. D. Burkhart, W. Pfaff, M. Reagor, L. Sletten, X. Ma, R. J. Schoelkopf, E. Knill, and K. W. Lehnert, "Faithful conversion of propagating quantum information to mechanical motion," Nature Physics, vol. 13, no. 12, pp. 1163–1167, Dec. 2017, number: 12 Publisher: Nature Publishing Group. [Online]. Available: https://www.nature.com/articles/nphys4251

[23] R. Manenti, M. J. Peterer, A. Nersisyan, E. B. Magnusson, A. Patterson, and P. J. Leek, "Surface acoustic wave resonators in the quantum regime," Physical Review B, vol. 93, no. 4, p. 041411, Jan. 2016, publisher: American Physical Society. [Online]. Available: https://link.aps.org/doi/10.1103/PhysRevB.93.041411

[24] N. M. Sundaresan, Y. Liu, D. Sadri, L. J. Szőcs, D. L. Underwood, M. Malekakhlagh, H. E. Türeci, and A. A. Houck, "Beyond Strong Coupling in a Multimode Cavity," Physical Review X, vol. 5, no. 2, p. 021035, Jun. 2015, publisher: American Physical Society. [Online]. Available: https://link.aps.org/doi/10.1103/PhysRevX.5.021035

[25] R. K. Naik, N. Leung, S. Chakram, P. Groszkowski, Y. Lu, N. Earnest, D. C. McKay, J. Koch, and D. I. Schuster, "Random access quantum information processors using multimode circuit quantum electrodynamics," Nature Communications, vol. 8, no. 1, p. 1904, Dec. 2017, number: 1 Publisher: Nature Publishing Group. [Online]. Available: https://www.nature.com/articles/s41467-017-02046-6

[26] C. T. Hann, C.-L. Zou, Y. Zhang, Y. Chu, R. J. Schoelkopf, S. Girvin, and L. Jiang, "Hardware-Efficient Quantum Random Access Memory with Hybrid Quantum Acoustic Systems," Physical Review Letters, vol. 123, no. 25, p. 250501, Dec. 2019, publisher: American Physical Society. [Online]. Available: https://link.aps.org/doi/10.1103/PhysRevLett.123.250501

[27] S. Chakram, K. He, A. V. Dixit, A. E. Oriani, R. K. Naik, N. Leung, H. Kwon, W.-L. Ma, L. Jiang, and D. I. Schuster, "Multimode photon blockade," arXiv:2010.15292 [cond-mat, physics:quant-ph], Oct. 2020, arXiv: 2010.15292. [Online]. Available: http://arxiv.org/abs/2010.15292

[28] R. Peterson, T. Purdy, N. Kampel, R. Andrews, P.-L. Yu, K. Lehnert, and C. Regal, "Laser Cooling of a Micromechanical Membrane to the Quantum Backaction Limit," Physical Review Letters, vol. 116, no. 6, p. 063601, Feb. 2016, publisher: American Physical Society. [Online]. Available: https://link.aps.org/doi/10.1103/PhysRevLett.116.063601

[29] J. Chan, T. P. M. Alegre, A. H. Safavi-Naeini, J. T. Hill, A. Krause, S. Gröblacher, M. Aspelmeyer, and O. Painter, "Laser cooling of a nanomechanical oscillator into its quantum ground state," Nature, vol. 478, no. 7367, pp. 89–92, Oct. 2011, number: 7367 Publisher: Nature Publishing Group. [Online]. Available: https://www.nature.com/articles/nature10461

[30] J. D. Teufel, T. Donner, D. Li, J. W. Harlow, M. S. Allman, K. Cicak, A. J. Sirois, J. D. Whittaker, K. W. Lehnert, and R. W. Simmonds, "Sideband cooling of micromechanical motion to the quantum ground state," Nature, vol. 475, no. 7356, pp. 359–363, Jul. 2011, number: 7356 Publisher: Nature Publishing Group. [Online]. Available: https://www.nature.com/articles/nature10261

[31] J.-M. Pirkkalainen, E. Damskägg, M. Brandt, F. Massel, and M. Sillanpää, "Squeezing of Quantum Noise of Motion in a Micromechanical Resonator," Physical Review Letters, vol. 115, no. 24, p. 243601, Dec. 2015, publisher: American Physical Society. [Online]. Available: https://link.aps.org/doi/10.1103/PhysRevLett.115.243601

[32] F. Lecocq, J. Clark, R. Simmonds, J. Aumentado, and J. Teufel, "Quantum Nondemolition Measurement of a Nonclassical State of a Massive Object," Physical Review X, vol. 5, no. 4, p. 041037, Dec. 2015, publisher: American Physical Society. [Online]. Available: https://link.aps.org/doi/10.1103/PhysRevX.5.041037

[33] T. A. Palomaki, J. D. Teufel, R. W. Simmonds, and K. W. Lehnert, "Entangling mechanical motion with microwave fields," Science (New York, N.Y.), vol. 342, no. 6159, pp. 710–713, Nov. 2013.

[34] R. Riedinger, S. Hong, R. A. Norte, J. A. Slater, J. Shang, A. G. Krause, V. Anant, M. Aspelmeyer, and S. Gröblacher, "Non-classical correlations between single photons and phonons from a mechanical oscillator," Nature, vol. 530, no. 7590, pp. 313–316, Feb. 2016, number: 7590 Publisher: Nature Publishing Group. [Online]. Available: https://www.nature.com/articles/nature16536

[35] C. F. Ockeloen-Korppi, E. Damskägg, J.-M. Pirkkalainen, M. Asjad, A. A. Clerk, F. Massel, M. J. Woolley, and M. A. Sillanpää, "Stabilized entanglement of massive mechanical oscillators," Nature, vol. 556, no. 7702, pp. 478–482, Apr. 2018, number: 7702 Publisher: Nature Publishing Group. [Online]. Available: https://www.nature.com/articles/s41586-018-0038-x

[36] C. Whittle et al, "Approaching the motional ground state of a 10 kg object," arXiv:2102.12665 [quant-ph], Feb. 2021, arXiv: 2102.12665. [Online]. Available: http://arxiv.org/abs/2102.12665

[37] F. Lecocq, J. D. Teufel, J. Aumentado, and R. W. Simmonds, "Resolving the vacuum fluctuations of an optomechanical system using an artificial atom," Nature Physics, vol. 11, no. 8, pp. 635–639, Aug. 2015, number: 8 Publisher: Nature Publishing Group. [Online]. Available: https://www.nature.com/articles/nphys3365

[38] D. J. Wineland, C. Monroe, W. M. Itano, D. Leibfried, B. E. King, and D. M. Meekhof, "Experimental Issues in Coherent Quantum-State Manipulation of Trapped Atomic Ions," Journal of Research of the National Institute of Standards

and Technology, vol. 103, no. 3, pp. 259–328, 1998. [Online]. Available: https://www.ncbi.nlm.nih.gov/pmc/articles/PMC4898965/

[39] D. M. Meekhof, C. Monroe, B. E. King, W. M. Itano, and D. J. Wineland, "Generation of Nonclassical Motional States of a Trapped Atom," Physical Review Letters, vol. 76, no. 11, pp. 1796–1799, Mar. 1996, publisher: American Physical Society. [Online]. Available: https://link.aps.org/doi/10.1103/PhysRevLett.76.1796

[40] C. Monroe, D. M. Meekhof, B. E. King, and D. J. Wineland, "A "Schrödinger Cat" Superposition State of an Atom," Science, vol. 272, no. 5265, pp. 1131–1136, May 1996, publisher: American Association for the Advancement of Science Section: Research Articles. [Online]. Available: https://science.sciencemag.org/content/272/5265/1131

[41] K. C. McCormick, J. Keller, S. C. Burd, D. J. Wineland, A. C. Wilson, and D. Leibfried, "Quantum-enhanced sensing of a single-ion mechanical oscillator," Nature, vol. 572, no. 7767, pp. 86–90, Aug. 2019, number: 7767 Publisher: Nature Publishing Group. [Online]. Available: https://www.nature.com/articles/s41586-019-1421-y

[42] S. M. Girvin, M. H. Devoret, and R. J. Schoelkopf, "Circuit QED and engineering charge based superconducting qubits," Physica Scripta, vol. T137, p. 014012, Dec. 2009, arXiv: 0912.3902. [Online]. Available: http://arxiv.org/abs/0912.3902

[43] M. H. Devoret and R. J. Schoelkopf, "Superconducting Circuits for Quantum Information: An Outlook," Science, vol. 339, no. 6124, pp. 1169–1174, Mar. 2013, publisher: American Association for the Advancement of Science Section: Review. [Online]. Available: https://science.sciencemag.org/content/339/6124/1169

[44] S. Haroche, M. Brune, and J. M. Raimond, "From cavity to circuit quantum electrodynamics," Nature Physics, vol. 16, no. 3, pp. 243–246, Mar. 2020, number: 3 Publisher: Nature Publishing Group. [Online]. Available: https://www.nature.com/articles/s41567-020-0812-1

[45] A. Wallraff, D. I. Schuster, A. Blais, L. Frunzio, R.-S. Huang, J. Majer, S. Kumar, S. M. Girvin, and R. J. Schoelkopf, "Strong coupling of a single photon to a superconducting qubit using circuit quantum electrodynamics," Nature, vol. 431, no. 7005, pp. 162–167, Sep. 2004, number: 7005 Publisher: Nature Publishing Group. [Online]. Available: https://www.nature.com/articles/nature02851

[46] D. I. Schuster, A. A. Houck, J. A. Schreier, A. Wallraff, J. M. Gambetta, A. Blais, L. Frunzio, J. Majer, B. Johnson, M. H. Devoret, S. M. Girvin, and R. J. Schoelkopf, "Resolving photon number states in a superconducting circuit," Nature, vol. 445, no. 7127, pp. 515–518, Feb. 2007, number: 7127 Publisher: Nature Publishing Group. [Online]. Available: https://www.nature.com/articles/nature05461

[47] M. Hofheinz, H. Wang, M. Ansmann, R. C. Bialczak, E. Lucero, M. Neeley, A. D. O'Connell, D. Sank, J. Wenner, J. M. Martinis, and A. N. Cleland, "Synthesizing arbitrary quantum states in a superconducting resonator," Nature, vol. 459, no. 7246, pp. 546–549, May 2009, number: 7246 Publisher: Nature Publishing Group. [Online]. Available: https://www.nature.com/articles/nature08005

[48] S. Krastanov, V. V. Albert, C. Shen, C.-L. Zou, R. W. Heeres, B. Vlastakis, R. J. Schoelkopf, and L. Jiang, "Universal control of an oscillator with dispersive coupling to a qubit," Physical Review A, vol. 92, no. 4, p. 040303, Oct. 2015, publisher: American Physical Society. [Online]. Available: https://link.aps.org/doi/10.1103/PhysRevA.92.040303

[49] R. W. Heeres, P. Reinhold, N. Ofek, L. Frunzio, L. Jiang, M. H. Devoret, and R. J. Schoelkopf, "Implementing a universal gate set on a logical qubit encoded in an oscillator," Nature Communications, vol. 8, no. 1, p. 94, Jul. 2017, number: 1 Publisher: Nature Publishing Group. [Online]. Available: https://www.nature.com/articles/s41467-017-00045-1

[50] D. Gottesman, A. Kitaev, and J. Preskill, "Encoding a qubit in an oscillator," Physical Review A, vol. 64, no. 1, p. 012310, Jun. 2001, publisher: American Physical Society. [Online]. Available: https://link.aps.org/doi/10.1103/PhysRevA.64.012310

[51] M. Reagor, W. Pfaff, C. Axline, R. W. Heeres, N. Ofek, K. Sliwa, E. Holland, C. Wang, J. Blumoff, K. Chou, M. J. Hatridge, L. Frunzio, M. H. Devoret, L. Jiang, and R. J. Schoelkopf, "Quantum memory with millisecond coherence in circuit QED," Physical Review B, vol. 94, no. 1, p. 014506, Jul. 2016, publisher: American Physical Society. [Online]. Available: https://link.aps.org/doi/10.1103/PhysRevB.94.014506

[52] N. Ofek, A. Petrenko, R. Heeres, P. Reinhold, Z. Leghtas, B. Vlastakis, Y. Liu, L. Frunzio, S. M. Girvin, L. Jiang, M. Mirrahimi, M. H. Devoret, and R. J. Schoelkopf, "Extending the lifetime of a quantum bit with error correction in superconducting circuits," Nature, vol. 536, no. 7617, pp. 441–445, Aug. 2016, number: 7617 Publisher: Nature Publishing Group. [Online]. Available: https://www.nature.com/articles/nature18949

[53] A. Grimm, N. E. Frattini, S. Puri, S. O. Mundhada, S. Touzard, M. Mirrahimi, S. M. Girvin, S. Shankar, and M. H. Devoret, "Stabilization and operation of a Kerr-cat qubit," Nature, vol. 584, no. 7820, pp. 205–209, Aug. 2020, number: 7820 Publisher: Nature Publishing Group. [Online]. Available: https://www.nature.com/articles/s41586-020-2587-z

[54] A. D. O'Connell, M. Hofheinz, M. Ansmann, R. C. Bialczak, M. Lenander, E. Lucero, M. Neeley, D. Sank, H. Wang, M. Weides, J. Wenner, J. M. Martinis, and A. N. Cleland, "Quantum ground state and single-phonon control of a mechanical resonator," Nature, vol. 464, no. 7289, pp. 697–703, Apr. 2010, number: 7289 Publisher: Nature Publishing Group. [Online]. Available: https://www.nature.com/articles/nature08967

[55] M. Schuetz, E. Kessler, G. Giedke, L. Vandersypen, M. Lukin, and J. Cirac, "Universal Quantum Transducers Based on Surface Acoustic Waves," Physical Review X, vol. 5, no. 3, p. 031031, Sep. 2015, publisher: American Physical Society. [Online]. Available: https://link.aps.org/doi/10.1103/PhysRevX.5.031031

[56] M. Forsch, R. Stockill, A. Wallucks, I. Marinković, C. Gärtner, R. A. Norte, F. van Otten, A. Fiore, K. Srinivasan, and S. Gröblacher, "Microwave-to-optics conversion using a mechanical oscillator in its quantum ground state," Nature Physics, vol. 16, no. 1, pp. 69–74, Jan. 2020, number: 1 Publisher: Nature Publishing Group. [Online]. Available: https://www.nature.com/articles/s41567-019-0673-7

[57] M. Mirhosseini, A. Sipahigil, M. Kalaee, and O. Painter, "Superconducting qubit to optical photon transduction," Nature, vol. 588, no. 7839, pp. 599–603, Dec.

2020, number: 7839 Publisher: Nature Publishing Group. [Online]. Available: https://www.nature.com/articles/s41586-020-3038-6

[58] G. Peairs, M.-H. Chou, A. Bienfait, H.-S. Chang, C. Conner, E. Dumur, J. Grebel, R. Povey, E. Şahin, K. Satzinger, Y. Zhong, and A. Cleland, "Continuous and Time-Domain Coherent Signal Conversion between Optical and Microwave Frequencies," Physical Review Applied, vol. 14, no. 6, p. 061001, Dec. 2020, publisher: American Physical Society. [Online]. Available: https://link.aps.org/doi/10.1103/PhysRevApplied.14.061001

[59] A. Frisk Kockum, P. Delsing, and G. Johansson, "Designing frequency-dependent relaxation rates and Lamb shifts for a giant artificial atom," Physical Review A, vol. 90, no. 1, p. 013837, Jul. 2014, publisher: American Physical Society. [Online]. Available: https://link.aps.org/doi/10.1103/PhysRevA.90.013837

[60] D. Roy, C. Wilson, and O. Firstenberg, "Colloquium: Strongly interacting photons in one-dimensional continuum," Reviews of Modern Physics, vol. 89, no. 2, p. 021001, May 2017, publisher: American Physical Society. [Online]. Available: https://link.aps.org/doi/10.1103/RevModPhys.89.021001

[61] X. Gu, A. F. Kockum, A. Miranowicz, Y.-x. Liu, and F. Nori, "Microwave photonics with superconducting quantum circuits," Physics Reports, vol. 718-719, pp. 1–102, Nov. 2017. [Online]. Available: https://www.sciencedirect.com/science/article/pii/S0370157317303290

[62] J. D. Hood, A. Goban, A. Asenjo-Garcia, M. Lu, S.-P. Yu, D. E. Chang, and H. J. Kimble, "Atom–atom interactions around the band edge of a photonic crystal waveguide," Proceedings of the National Academy of Sciences, vol. 113, no. 38, pp. 10 507–10 512, Sep. 2016, publisher: National Academy of Sciences Section: Physical Sciences. [Online]. Available: https://www.pnas.org/content/113/38/10507

[63] M. V. Gustafsson, T. Aref, A. F. Kockum, M. K. Ekström, G. Johansson, and P. Delsing, "Propagating phonons coupled to an artificial atom," Science, vol. 346, no. 6206, pp. 207–211, Oct. 2014, publisher: American Association for the Advancement of Science Section: Research Article. [Online]. Available: https://science.sciencemag.org/content/346/6206/207

[64] B. A. Moores, L. R. Sletten, J. J. Viennot, and K. Lehnert, "Cavity Quantum Acoustic Device in the Multimode Strong Coupling Regime," Physical Review Letters, vol. 120, no. 22, p. 227701, May 2018, publisher: American Physical Society. [Online]. Available: https://link.aps.org/doi/10.1103/PhysRevLett.120.227701

[65] L. Sletten, B. Moores, J. Viennot, and K. Lehnert, "Resolving Phonon Fock States in a Multimode Cavity with a Double-Slit Qubit," Physical Review X, vol. 9, no. 2, p. 021056, Jun. 2019, publisher: American Physical Society. [Online]. Available: https://link.aps.org/doi/10.1103/PhysRevX.9.021056

[66] Y. Chu, P. Kharel, W. H. Renninger, L. D. Burkhart, L. Frunzio, P. T. Rakich, and R. J. Schoelkopf, "Quantum acoustics with superconducting qubits," Science, vol. 358, no. 6360, pp. 199–202, Oct. 2017, publisher: American Association for the Advancement of Science Section: Report. [Online]. Available: https://science.sciencemag.org/content/358/6360/199

[67] Y. Chu, P. Kharel, T. Yoon, L. Frunzio, P. T. Rakich, and R. J. Schoelkopf, "Creation and control of multi-phonon Fock states in a bulk acoustic-wave resonator," Nature, vol. 563, no.

7733, pp. 666–670, Nov. 2018, number: 7733 Publisher: Nature Publishing Group. [Online]. Available: https://www.nature.com/articles/s41586-018-0717-7

[68] W. H. Renninger, P. Kharel, R. O. Behunin, and P. T. Rakich, "Bulk crystalline optomechanics," Nature Physics, vol. 14, no. 6, pp. 601–607, Jun. 2018, number: 6 Publisher: Nature Publishing Group. [Online]. Available: https://www.nature.com/articles/s41567-018-0090-3

[69] R. Manenti, A. F. Kockum, A. Patterson, T. Behrle, J. Rahamim, G. Tancredi, F. Nori, and P. J. Leek, "Circuit quantum acoustodynamics with surface acoustic waves," Nature Communications, vol. 8, no. 1, p. 975, Oct. 2017, number: 1 Publisher: Nature Publishing Group. [Online]. Available: https://www.nature.com/articles/s41467-017-01063-9

[70] K. J. Satzinger, Y. P. Zhong, H.-S. Chang, G. A. Peairs, A. Bienfait, M.-H. Chou, A. Y. Cleland, C. R. Conner, E. Dumur, J. Grebel, I. Gutierrez, B. H. November, R. G. Povey, S. J. Whiteley, D. D. Awschalom, D. I. Schuster, and A. N. Cleland, "Quantum control of surface acoustic-wave phonons," Nature, vol. 563, no. 7733, pp. 661–665, Nov. 2018, number: 7733 Publisher: Nature Publishing Group. [Online]. Available: https://www.nature.com/articles/s41586-018-0719-5

[71] A. Bienfait, K. J. Satzinger, Y. P. Zhong, H.-S. Chang, M.-H. Chou, C. R. Conner, E. Dumur, J. Grebel, G. A. Peairs, R. G. Povey, and A. N. Cleland, "Phonon-mediated quantum state transfer and remote qubit entanglement," Science, vol. 364, no. 6438, pp. 368–371, Apr. 2019, publisher: American Association for the Advancement of Science Section: Report. [Online]. Available: https://science.sciencemag.org/content/364/6438/368

[72] A. Bienfait, Y. Zhong, H.-S. Chang, M.-H. Chou, C. Conner, E. Dumur, J. Grebel, G. Peairs, R. Povey, K. Satzinger, and A. Cleland, "Quantum Erasure Using Entangled Surface Acoustic Phonons," Physical Review X, vol. 10, no. 2, p. 021055, Jun. 2020, publisher: American Physical Society. [Online]. Available: https://link.aps.org/doi/10.1103/PhysRevX.10.021055

[73] P. Arrangoiz-Arriola, E. A. Wollack, Z. Wang, M. Pechal, W. Jiang, T. P. McKenna, J. D. Witmer, R. Van Laer, and A. H. Safavi-Naeini, "Resolving the energy levels of a nanomechanical oscillator," Nature, vol. 571, no. 7766, pp. 537–540, Jul. 2019, number: 7766 Publisher: Nature Publishing Group. [Online]. Available: https://www.nature.com/articles/s41586-019-1386-x

[74] J. Viennot, X. Ma, and K. Lehnert, "Phonon-Number-Sensitive Electromechanics," Physical Review Letters, vol. 121, no. 18, p. 183601, Oct. 2018, publisher: American Physical Society. [Online]. Available: https://link.aps.org/doi/10.1103/PhysRevLett.121.183601

[75] X. Ma, J. J. Viennot, S. Kotler, J. D. Teufel, and K. W. Lehnert, "Non-classical energy squeezing of a macroscopic mechanical oscillator," Nature Physics, vol. 17, no. 3, pp. 322–326, Mar. 2021, number: 3 Publisher: Nature Publishing Group. [Online]. Available: https://www.nature.com/articles/s41567-020-01102-1

[76] R. M. White and F. W. Voltmer, "Direct piezoelectric coupling to surface elastic waves," Applied Physics Letters, vol. 7, no. 12, pp. 314–316, Dec. 1965, publisher: American Institute of Physics. [Online]. Available: https://aip.scitation.org/doi/10.1063/1.1754276

[77] Datta, Supriyo, Surface Acosutic Wave Devices. Englewood Cliffs, N.J.: Prentice-Hall, 1986.

[78] Y. Ebata, "Suppression of bulk-scattering loss in SAW resonator with quasi-constant acoustic reflection periodicity," in IEEE 1988 Ultrasonics Symposium Proceedings., Oct. 1988, pp. 91–96 vol.1.

[79] L. Shao, S. Maity, L. Zheng, L. Wu, A. Shams-Ansari, Y.-I. Sohn, E. Puma, M. Gadalla, M. Zhang, C. Wang, E. Hu, K. Lai, and M. Lončar, "Phononic Band Structure Engineering for High-Q Gigahertz Surface Acoustic Wave Resonators on Lithium Niobate," Physical Review Applied, vol. 12, no. 1, p. 014022, Jul. 2019, publisher: American Physical Society. [Online]. Available: https://link.aps.org/doi/10.1103/PhysRevApplied.12.014022

[80] D. M. Pozar, Microwave Engineering, 4th ed. Hamilton Printing, 2012.

[81] T. Aref, M. K. Ekström, P. Delsing, A. F. Kockum, M. V. Gustafsson, G. Johansson, P. J. Leek, E. Magnusson, and R. Manenti, "Quantum Acoustics with Surface Acoustic Waves," in Superconducting Devices in Quantum Optics, ser. Quantum Science and Technology. Springer, 2016.

[82] B. P. Abbott and L. Solie, "A minimal diffraction cut of quartz for high performance SAW filters," in 2000 IEEE Ultrasonics Symposium. Proceedings. An International Symposium (Cat. No.00CH37121), vol. 1, Oct. 2000, pp. 235–240 vol.1, iSSN: 1051-0117.

[83] C. K. Campbell, "Modelling the transverse-mode response of a two-port SAW resonator," IEEE Transactions on Ultrasonics, Ferroelectrics, and Frequency Control, vol. 38, no. 3, pp. 237–242, May 1991, conference Name: IEEE Transactions on Ultrasonics, Ferroelectrics, and Frequency Control.

[84] W. Tanski, "Surface Acoustic Wave Resonators on Quartz," IEEE Transactions on Sonics and Ultrasonics, vol. 26, no. 2, pp. 93–104, Mar. 1979, conference Name: IEEE Transactions on Sonics and Ultrasonics.

[85] S. Wilkus, C. Hartmann, and R. Kansy, "Transverse Mode Compensation of Surface Acoustic Wave Filters," in IEEE 1985 Ultrasonics Symposium, Oct. 1985, pp. 43–47.

[86] M. Mayer, A. Bergmann, G. Kovacs, and K. Wagner, "Low loss recursive filters for basestation applications without spurious modes," in IEEE Ultrasonics Symposium, 2005., vol. 2, Sep. 2005, pp. 1061–1064, iSSN: 1051-0117.

[87] M. Solal, O. Holmgren, and K. Kokkonen, "Design, simulation, and visualization of R-SPUDT devices with transverse mode suppression," IEEE Transactions on Ultrasonics, Ferroelectrics, and Frequency Control, vol. 57, no. 2, pp. 412–420, Feb. 2010, conference Name: IEEE Transactions on Ultrasonics, Ferroelectrics, and Frequency Control.

[88] M. Solal, J. Gratier, R. Aigner, K. Gamble, B. Abbott, T. Kook, A. Chen, and K. Steiner, "Transverse modes suppression and loss reduction for buried electrodes SAW devices," in 2010 IEEE International Ultrasonics Symposium, Oct. 2010, pp. 624–628, iSSN: 1948-5727.

[89] J. S. Toll, "Causality and the Dispersion Relation: Logical Foundations," Physical Review, vol. 104, no. 6, pp. 1760–1770, Dec. 1956, publisher: American Physical Society. [Online]. Available: https://link.aps.org/doi/10.1103/PhysRev.104.1760

[90] B. D. Josephson, "Possible new effects in superconductive tunnelling," Physics Letters, vol. 1, no. 7, pp. 251–253, Jul. 1962. [Online]. Available: https://www.sciencedirect.com/science/article/pii/0031916362913690

[91] Y. Makhlin, G. Schön, and A. Shnirman, "Quantum-state engineering with Josephson-junction devices," Reviews of Modern Physics, vol. 73, no. 2, pp. 357–400, May 2001, publisher: American Physical Society. [Online]. Available: https://link.aps.org/doi/10.1103/RevModPhys.73.357

[92] J. Koch, T. M. Yu, J. Gambetta, A. A. Houck, D. I. Schuster, J. Majer, A. Blais, M. H. Devoret, S. M. Girvin, and R. J. Schoelkopf, "Charge-insensitive qubit design derived from the Cooper pair box," Physical Review A, vol. 76, no. 4, p. 042319, Oct. 2007, publisher: American Physical Society. [Online]. Available: https://link.aps.org/doi/10.1103/PhysRevA.76.042319

[93] M. A. Castellanos-Beltran, K. D. Irwin, G. C. Hilton, L. R. Vale, and K. W. Lehnert, "Amplification and squeezing of quantum noise with a tunable Josephson metamaterial," Nature Physics, vol. 4, no. 12, pp. 929–931, Dec. 2008, number: 12 Publisher: Nature Publishing Group. [Online]. Available: https://www.nature.com/articles/nphys1090

[94] T. Yamamoto, K. Inomata, M. Watanabe, K. Matsuba, T. Miyazaki, W. D. Oliver, Y. Nakamura, and J. S. Tsai, "Flux-driven Josephson parametric amplifier," Applied Physics Letters, vol. 93, no. 4, p. 042510, Jul. 2008, publisher: American Institute of Physics. [Online]. Available: https://aip.scitation.org/doi/10.1063/1.2964182

[95] N. Bergeal, R. Vijay, V. E. Manucharyan, I. Siddiqi, R. J. Schoelkopf, S. M. Girvin, and M. H. Devoret, "Analog information processing at the quantum limit with a Josephson ring modulator," Nature Physics, vol. 6, no. 4, pp. 296–302, Apr. 2010, number: 4 Publisher: Nature Publishing Group. [Online]. Available: https://www.nature.com/articles/nphys1516

[96] C. Macklin, K. O'Brien, D. Hover, M. E. Schwartz, V. Bolkhovsky, X. Zhang, W. D. Oliver, and I. Siddiqi, "A near–quantum-limited Josephson traveling-wave parametric amplifier," Science, vol. 350, no. 6258, pp. 307–310, Oct. 2015, publisher: American Association for the Advancement of Science Section: Report. [Online]. Available: https://science.sciencemag.org/content/350/6258/307

[97] G. Liu, T.-C. Chien, X. Cao, O. Lanes, E. Alpern, D. Pekker, and M. Hatridge, "Josephson parametric converter saturation and higher order effects," Applied Physics Letters, vol. 111, no. 20, p. 202603, Nov. 2017, publisher: American Institute of Physics. [Online]. Available: https://aip.scitation.org/doi/10.1063/1.5003032

[98] F. Arute, K. Arya, R. Babbush, D. Bacon, J. C. Bardin, R. Barends, R. Biswas, S. Boixo, F. G. S. L. Brandao, D. A. Buell, B. Burkett, Y. Chen, Z. Chen, B. Chiaro, R. Collins, W. Courtney, A. Dunsworth, E. Farhi, B. Foxen, A. Fowler, C. Gidney, M. Giustina, R. Graff, K. Guerin, S. Habegger, M. P. Harrigan, M. J. Hartmann, A. Ho, M. Hoffmann, T. Huang, T. S. Humble, S. V. Isakov, E. Jeffrey, Z. Jiang, D. Kafri, K. Kechedzhi, J. Kelly, P. V. Klimov, S. Knysh, A. Korotkov, F. Kostritsa, D. Landhuis, M. Lindmark, E. Lucero, D. Lyakh, S. Mandrà, J. R. McClean, M. McEwen, A. Megrant, X. Mi, K. Michielsen, M. Mohseni, J. Mutus, O. Naaman, M. Neeley, C. Neill, M. Y. Niu, E. Ostby, A. Petukhov, J. C. Platt, C. Quintana, E. G. Rieffel, P. Roushan, N. C. Rubin, D. Sank, K. J.

Satzinger, V. Smelyanskiy, K. J. Sung, M. D. Trevithick, A. Vainsencher, B. Villalonga, T. White, Z. J. Yao, P. Yeh, A. Zalcman, H. Neven, and J. M. Martinis, "Quantum supremacy using a programmable superconducting processor," Nature, vol. 574, no. 7779, pp. 505–510, Oct. 2019, number: 7779 Publisher: Nature Publishing Group. [Online]. Available: https://www.nature.com/articles/s41586-019-1666-5

[99] A. D. Corcoles, M. Takita, K. Inoue, S. Lekuch, Z. K. Minev, J. M. Chow, and J. M. Gambetta, "Exploiting dynamic quantum circuits in a quantum algorithm with superconducting qubits," arXiv:2102.01682 [quant-ph], Feb. 2021, arXiv: 2102.01682. [Online]. Available: http://arxiv.org/abs/2102.01682

[100] A. Gold, J. P. Paquette, A. Stockklauser, M. J. Reagor, M. S. Alam, A. Bestwick, N. Didier, A. Nersisyan, F. Oruc, A. Razavi, B. Scharmann, E. A. Sete, B. Sur, D. Venturelli, C. J. Winkleblack, F. Wudarski, M. Harburn, and C. Rigetti, "Entanglement Across Separate Silicon Dies in a Modular Superconducting Qubit Device," arXiv:2102.13293 [quant-ph], Mar. 2021, arXiv: 2102.13293. [Online]. Available: http://arxiv.org/abs/2102.13293

[101] E. T. Jaynes and F. W. Cummings, "Comparison of quantum and semiclassical radiation theories with application to the beam maser," Proceedings of the IEEE, vol. 51, no. 1, pp. 89–109, Jan. 1963, conference Name: Proceedings of the IEEE.

[102] D. Zueco, G. M. Reuther, S. Kohler, and P. Hänggi, "Qubit-oscillator dynamics in the dispersive regime: Analytical theory beyond the rotating-wave approximation," Physical Review A, vol. 80, no. 3, p. 033846, Sep. 2009, publisher: American Physical Society. [Online]. Available: https://link.aps.org/doi/10.1103/PhysRevA.80.033846

[103] J. M. Fink, M. Göppl, M. Baur, R. Bianchetti, P. J. Leek, A. Blais, and A. Wallraff, "Climbing the Jaynes–Cummings ladder and observing its nonlinearity in a cavity QED system," Nature, vol. 454, no. 7202, pp. 315–318, Jul. 2008, number: 7202 Publisher: Nature Publishing Group. [Online]. Available: https://www.nature.com/articles/nature07112

[104] M. Boissonneault, J. M. Gambetta, and A. Blais, "Dispersive regime of circuit QED: Photon-dependent qubit dephasing and relaxation rates," Physical Review A, vol. 79, no. 1, p. 013819, Jan. 2009, publisher: American Physical Society. [Online]. Available: https://link.aps.org/doi/10.1103/PhysRevA.79.013819

[105] L. Sun, A. Petrenko, Z. Leghtas, B. Vlastakis, G. Kirchmair, K. M. Sliwa, A. Narla, M. Hatridge, S. Shankar, J. Blumoff, L. Frunzio, M. Mirrahimi, M. H. Devoret, and R. J. Schoelkopf, "Tracking photon jumps with repeated quantum non-demolition parity measurements," Nature, vol. 511, no. 7510, pp. 444–448, Jul. 2014, number: 7510 Publisher: Nature Publishing Group. [Online]. Available: https://www.nature.com/articles/nature13436

[106] S. Haroche, M. Brune, and J.-M. Raimond, "Measuring the photon number parity in a cavity: from light quantum jumps to the tomography of non-classical field states," Journal of Modern Optics, vol. 54, no. 13-15, pp. 2101–2114, Sep. 2007, publisher: Taylor & Francis _eprint: https://doi.org/10.1080/09500340701391118. [Online]. Available: https://doi.org/10.1080/09500340701391118

[107] A. A. Houck, J. A. Schreier, B. R. Johnson, J. M. Chow, J. Koch, J. M. Gambetta, D. I. Schuster, L. Frunzio, M. H. Devoret, S. M. Girvin, and R. J. Schoelkopf, "Controlling the Spontaneous Emission of a Superconducting Transmon Qubit," Physical Review Letters, vol. 101, no. 8, p. 080502, Aug. 2008, publisher: American Physical Society. [Online]. Available: https://link.aps.org/doi/10.1103/PhysRevLett.101.080502

[108] E. Jeffrey, D. Sank, J. Mutus, T. White, J. Kelly, R. Barends, Y. Chen, Z. Chen, B. Chiaro, A. Dunsworth, A. Megrant, P. O'Malley, C. Neill, P. Roushan, A. Vainsencher, J. Wenner, A. Cleland, and J. M. Martinis, "Fast Accurate State Measurement with Superconducting Qubits," Physical Review Letters, vol. 112, no. 19, p. 190504, May 2014, publisher: American Physical Society. [Online]. Available: https://link.aps.org/doi/10.1103/PhysRevLett.112.190504

[109] G. Andersson, B. Suri, L. Guo, T. Aref, and P. Delsing, "Non-exponential decay of a giant artificial atom," Nature Physics, vol. 15, no. 11, pp. 1123–1127, Nov. 2019, number: 11 Publisher: Nature Publishing Group. [Online]. Available: https://www.nature.com/articles/s41567-019-0605-6

[110] A. F. Kockum, G. Johansson, and F. Nori, "Decoherence-Free Interaction between Giant Atoms in Waveguide Quantum Electrodynamics," Physical Review Letters, vol. 120, no. 14, p. 140404, Apr. 2018, publisher: American Physical Society. [Online]. Available: https://link.aps.org/doi/10.1103/PhysRevLett.120.140404

[111] M. K. Ekström, T. Aref, A. Ask, G. Andersson, B. Suri, H. Sanada, G. Johansson, and P. Delsing, "Towards phonon routing: controlling propagating acoustic waves in the quantum regime," New Journal of Physics, vol. 21, no. 12, p. 123013, Dec. 2019, publisher: IOP Publishing. [Online]. Available: https://iopscience.iop.org/article/10.1088/1367-2630/ab5ca5/meta

[112] H. Pichler, S. Choi, P. Zoller, and M. D. Lukin, "Universal photonic quantum computation via time-delayed feedback," Proceedings of the National Academy of Sciences, vol. 114, no. 43, pp. 11 362–11 367, Oct. 2017, publisher: National Academy of Sciences Section: Physical Sciences. [Online]. Available: https://www.pnas.org/content/114/43/11362

[113] Y. Liu and A. A. Houck, "Quantum electrodynamics near a photonic bandgap," Nature Physics, vol. 13, no. 1, pp. 48–52, Jan. 2017, number: 1 Publisher: Nature Publishing Group. [Online]. Available: https://www.nature.com/articles/nphys3834

[114] M. Mirhosseini, E. Kim, V. S. Ferreira, M. Kalaee, A. Sipahigil, A. J. Keller, and O. Painter, "Superconducting metamaterials for waveguide quantum electrodynamics," Nature Communications, vol. 9, no. 1, p. 3706, Sep. 2018, number: 1 Publisher: Nature Publishing Group. [Online]. Available: https://www.nature.com/articles/s41467-018-06142-z

[115] W. Zhang, K. Kalashnikov, W.-S. Lu, P. Kamenov, T. DiNapoli, and M. Gershenson, "Microresonators Fabricated from High-Kinetic-Inductance Aluminum Films," Physical Review Applied, vol. 11, no. 1, p. 011003, Jan. 2019, publisher: American Physical Society. [Online]. Available: https://link.aps.org/doi/10.1103/PhysRevApplied.11.011003

[116] M. Scigliuzzo, L. E. Bruhat, A. Bengtsson, J. J. Burnett, A. F. Roudsari, and P. Delsing, "Phononic loss in superconducting resonators on piezoelectric substrates,"

New Journal of Physics, vol. 22, no. 5, p. 053027, May 2020, publisher: IOP Publishing. [Online]. Available: https://doi.org/10.1088/1367-2630/ab8044

[117] C. Wang, C. Axline, Y. Y. Gao, T. Brecht, Y. Chu, L. Frunzio, M. H. Devoret, and R. J. Schoelkopf, "Surface participation and dielectric loss in superconducting qubits," Applied Physics Letters, vol. 107, no. 16, p. 162601, Oct. 2015, publisher: American Institute of Physics. [Online]. Available: https://aip.scitation.org/doi/full/10.1063/1.4934486

[118] V. Ambegaokar and A. Baratoff, "Tunneling Between Superconductors," Physical Review Letters, vol. 10, no. 11, pp. 486–489, Jun. 1963, publisher: American Physical Society. [Online]. Available: https://link.aps.org/doi/10.1103/PhysRevLett.10.486

[119] E. A. Sete, J. M. Martinis, and A. N. Korotkov, "Quantum theory of a bandpass Purcell filter for qubit readout," Physical Review A, vol. 92, no. 1, p. 012325, Jul. 2015, publisher: American Physical Society. [Online]. Available: https://link.aps.org/doi/10.1103/PhysRevA.92.012325

[120] C. Wang, Y. Y. Gao, P. Reinhold, R. W. Heeres, N. Ofek, K. Chou, C. Axline, M. Reagor, J. Blumoff, K. M. Sliwa, L. Frunzio, S. M. Girvin, L. Jiang, M. Mirrahimi, M. H. Devoret, and R. J. Schoelkopf, "A Schrödinger cat living in two boxes," Science, vol. 352, no. 6289, pp. 1087–1091, May 2016, publisher: American Association for the Advancement of Science Section: Reports. [Online]. Available: https://science.sciencemag.org/content/352/6289/1087

[121] M. Pechal, P. Arrangoiz-Arriola, and A. H. Safavi-Naeini, "Superconducting circuit quantum computing with nanomechanical resonators as storage," Quantum Science and Technology, vol. 4, no. 1, p. 015006, Sep. 2018, publisher: IOP Publishing. [Online]. Available: https://doi.org/10.1088/2058-9565/aadc6c

[122] P. Kharel, Y. Chu, M. Power, W. H. Renninger, R. J. Schoelkopf, and P. T. Rakich, "Ultra-high-Q phononic resonators on-chip at cryogenic temperatures," APL Photonics, vol. 3, no. 6, p. 066101, May 2018, publisher: American Institute of Physics. [Online]. Available: https://aip.scitation.org/doi/abs/10.1063/1.5026798

[123] A. H. Ghadimi, S. A. Fedorov, N. J. Engelsen, M. J. Bereyhi, R. Schilling, D. J. Wilson, and T. J. Kippenberg, "Elastic strain engineering for ultralow mechanical dissipation," Science, vol. 360, no. 6390, pp. 764–768, May 2018, publisher: American Association for the Advancement of Science Section: Report. [Online]. Available: https://science.sciencemag.org/content/360/6390/764

[124] G. S. MacCabe, H. Ren, J. Luo, J. D. Cohen, H. Zhou, A. Sipahigil, M. Mirhosseini, and O. Painter, "Nano-acoustic resonator with ultralong phonon lifetime," Science, vol. 370, no. 6518, pp. 840–843, Nov. 2020, publisher: American Association for the Advancement of Science Section: Report. [Online]. Available: https://science.sciencemag.org/content/370/6518/840

[125] L. Guo, A. Grimsmo, A. F. Kockum, M. Pletyukhov, and G. Johansson, "Giant acoustic atom: A single quantum system with a deterministic time delay," Physical Review A, vol. 95, no. 5, p. 053821, May 2017, publisher: American Physical Society. [Online]. Available: https://link.aps.org/doi/10.1103/PhysRevA.95.053821

[126] A. Fragner, M. Göppl, J. M. Fink, M. Baur, R. Bianchetti, P. J. Leek, A. Blais, and A. Wallraff, "Resolving Vacuum Fluctuations in an Electrical Circuit by Measuring the Lamb Shift," Science, vol. 322, no. 5906, pp. 1357–1360, Nov. 2008, publisher: American Association for the Advancement of Science Section: Report. [Online]. Available: https://science.sciencemag.org/content/322/5906/1357

[127] J. Eschner, C. Raab, F. Schmidt-Kaler, and R. Blatt, "Light interference from single atoms and their mirror images," Nature, vol. 413, no. 6855, pp. 495–498, Oct. 2001, number: 6855 Publisher: Nature Publishing Group. [Online]. Available: https://www.nature.com/articles/35097017

[128] I.-C. Hoi, A. F. Kockum, L. Tornberg, A. Pourkabirian, G. Johansson, P. Delsing, and C. M. Wilson, "Probing the quantum vacuum with an artificial atom in front of a mirror," Nature Physics, vol. 11, no. 12, pp. 1045–1049, Dec. 2015, number: 12 Publisher: Nature Publishing Group. [Online]. Available: https://www.nature.com/articles/nphys3484

[129] D. Lachance-Quirion, Y. Tabuchi, S. Ishino, A. Noguchi, T. Ishikawa, R. Yamazaki, and Y. Nakamura, "Resolving quanta of collective spin excitations in a millimeter-sized ferromagnet," Science Advances, vol. 3, no. 7, p. e1603150, Jul. 2017, publisher: American Association for the Advancement of Science Section: Research Article. [Online]. Available: https://advances.sciencemag.org/content/3/7/e1603150

[130] M. D. Reed, L. DiCarlo, B. R. Johnson, L. Sun, D. I. Schuster, L. Frunzio, and R. J. Schoelkopf, "High-Fidelity Readout in Circuit Quantum Electrodynamics Using the Jaynes-Cummings Nonlinearity," Physical Review Letters, vol. 105, no. 17, p. 173601, Oct. 2010, publisher: American Physical Society. [Online]. Available: https://link.aps.org/doi/10.1103/PhysRevLett.105.173601

[131] G. Andersson, S. W. Jolin, M. Scigliuzzo, R. Borgani, M. O. Tholén, D. B. Haviland, and P. Delsing, "Squeezing and correlations of multiple modes in a parametric acoustic cavity," arXiv:2007.05826 [quant-ph], Jul. 2020, arXiv: 2007.05826. [Online]. Available: http://arxiv.org/abs/2007.05826

[132] J. Beugnon, M. P. A. Jones, J. Dingjan, B. Darquié, G. Messin, A. Browaeys, and P. Grangier, "Quantum interference between two single photons emitted by independently trapped atoms," Nature, vol. 440, no. 7085, pp. 779–782, Apr. 2006, number: 7085 Publisher: Nature Publishing Group. [Online]. Available: https://www.nature.com/articles/nature04628

[133] D. L. Moehring, P. Maunz, S. Olmschenk, K. C. Younge, D. N. Matsukevich, L.-M. Duan, and C. Monroe, "Entanglement of single-atom quantum bits at a distance," Nature, vol. 449, no. 7158, pp. 68–71, Sep. 2007, number: 7158 Publisher: Nature Publishing Group. [Online]. Available: https://www.nature.com/articles/nature06118

[134] N. Roch, M. Schwartz, F. Motzoi, C. Macklin, R. Vijay, A. Eddins, A. Korotkov, K. Whaley, M. Sarovar, and I. Siddiqi, "Observation of Measurement-Induced Entanglement and Quantum Trajectories of Remote Superconducting Qubits," Physical Review Letters, vol. 112, no. 17, p. 170501, Apr. 2014, publisher: American Physical Society. [Online]. Available: https://link.aps.org/doi/10.1103/PhysRevLett.112.170501

[135] W. Dür, G. Vidal, and J. I. Cirac, "Three qubits can be entangled in two inequivalent ways," Physical Review A, vol. 62, no. 6, p. 062314, Nov. 2000, publisher: American Physical Society. [Online]. Available: https://link.aps.org/doi/10.1103/PhysRevA.62.062314

[136] V. E. Manucharyan, J. Koch, L. I. Glazman, and M. H. Devoret, "Fluxonium: Single Cooper-Pair Circuit Free of Charge Offsets," Science, vol. 326, no. 5949, pp. 113–116, Oct. 2009, publisher: American Association for the Advancement of Science Section: Report. [Online]. Available: https://science.sciencemag.org/content/326/5949/113

[137] L. B. Nguyen, Y.-H. Lin, A. Somoroff, R. Mencia, N. Grabon, and V. E. Manucharyan, "High-Coherence Fluxonium Qubit," Physical Review X, vol. 9, no. 4, p. 041041, Nov. 2019, publisher: American Physical Society. [Online]. Available: https://link.aps.org/doi/10.1103/PhysRevX.9.041041

[138] H. Zhang, S. Chakram, T. Roy, N. Earnest, Y. Lu, Z. Huang, D. Weiss, J. Koch, and D. I. Schuster, "Universal Fast-Flux Control of a Coherent, Low-Frequency Qubit," Physical Review X, vol. 11, no. 1, p. 011010, Jan. 2021, publisher: American Physical Society. [Online]. Available: https://link.aps.org/doi/10.1103/PhysRevX.11.011010

[139] E. Yarar, V. Hrkac, C. Zamponi, A. Piorra, L. Kienle, and E. Quandt, "Low temperature aluminum nitride thin films for sensory applications," AIP Advances, vol. 6, no. 7, p. 075115, Jul. 2016, publisher: American Institute of Physics. [Online]. Available: https://aip.scitation.org/doi/10.1063/1.4959895

[140] K. Uehara, C.-M. Yang, T. Shibata, S.-K. Kim, S. Kameda, H. Nakase, and K. Tsubouchi, "Fabrication of 5-GHz-band SAW filter with atomically-flat-surface AlN on sapphire," in IEEE Ultrasonics Symposium, 2004, vol. 1, Aug. 2004, pp. 203–206 Vol.1, iSSN: 1051-0117.

[141] R. Salut, G. Martin, W. Daniau, A. Claudel, D. Pique, and S. Ballandras, "Fabrication of a 4.4 GHz oscillator using SAW excited on epitaxial AlN grown on a Sapphire substrate," in 2013 IEEE International Ultrasonics Symposium (IUS), Jul. 2013, pp. 267–270, iSSN: 1051-0117.

[142] T. Aubert, O. Elmazria, B. Assouar, L. Bouvot, and M. Oudich, "Surface acoustic wave devices based on AlN/sapphire structure for high temperature applications," Applied Physics Letters, vol. 96, no. 20, p. 203503, May 2010, publisher: American Institute of Physics. [Online]. Available: https://aip.scitation.org/doi/10.1063/1.3430042

[143] B. Foxen, J. Y. Mutus, E. Lucero, R. Graff, A. Megrant, Y. Chen, C. Quintana, B. Burkett, J. Kelly, E. Jeffrey, Y. Yang, A. Yu, K. Arya, R. Barends, Z. Chen, B. Chiaro, A. Dunsworth, A. Fowler, C. Gidney, M. Giustina, T. Huang, P. Klimov, M. Neeley, C. Neill, P. Roushan, D. Sank, A. Vainsencher, J. Wenner, T. C. White, and J. M. Martinis, "Qubit compatible superconducting interconnects," Quantum Science and Technology, vol. 3, no. 1, p. 014005, Nov. 2017, publisher: IOP Publishing. [Online]. Available: https://doi.org/10.1088/2058-9565/aa94fc

[144] C. U. Lei, L. Krayzman, S. Ganjam, L. Frunzio, and R. J. Schoelkopf, "High coherence superconducting microwave cavities with indium bump bonding," Applied Physics Letters, vol. 116, no. 15, p. 154002, Apr. 2020, publisher: American Institute of Physics. [Online]. Available: https://aip.scitation.org/doi/10.1063/5.0003907

[145] R. J. Corruccini and J. Gniewek, "Thermal Expansion of Technical Solids at Low Temperatures: A Compilation From the Literature," 1961.

[146] A. T. Young, "Rayleigh scattering," Applied Optics, vol. 20, no. 4, pp. 533–535, Feb. 1981, publisher: Optical Society of America. [Online]. Available: https://www.osapublishing.org/ao/abstract.cfm?uri=ao-20-4-533

[147] T. Hazard, A. Gyenis, A. Di Paolo, A. Asfaw, S. Lyon, A. Blais, and A. Houck, "Nanowire Superinductance Fluxonium Qubit," Physical Review Letters, vol. 122, no. 1, p. 010504, Jan. 2019, publisher: American Physical Society. [Online]. Available: https://link.aps.org/doi/10.1103/PhysRevLett.122.010504

[148] Y.-H. Lin, L. B. Nguyen, N. Grabon, J. San Miguel, N. Pankratova, and V. E. Manucharyan, "Demonstration of Protection of a Superconducting Qubit from Energy Decay," Physical Review Letters, vol. 120, no. 15, p. 150503, Apr. 2018, publisher: American Physical Society. [Online]. Available: https://link.aps.org/doi/10.1103/PhysRevLett.120.150503

[149] A. Siegman, Lasers. Mill Valley, CA 94941: University Science Books, 1986.

[150] M. M. de Lima, F. Alsina, W. Seidel, and P. V. Santos, "Focusing of surface-acoustic-wave fields on (100) GaAs surfaces," Journal of Applied Physics, vol. 94, no. 12, pp. 7848–7855, Dec. 2003, publisher: American Institute of Physics. [Online]. Available: https://aip.scitation.org/doi/abs/10.1063/1.1625419

[151] M. E. Msall and P. V. Santos, "Focusing Surface-Acoustic-Wave Microcavities on GaAs," Physical Review Applied, vol. 13, no. 1, p. 014037, Jan. 2020, publisher: American Physical Society. [Online]. Available: https://link.aps.org/doi/10.1103/PhysRevApplied.13.014037

[152] B. P. Newberry and R. B. Thompson, "A paraxial theory for the propagation of ultrasonic beams in anisotropic solids," The Journal of the Acoustical Society of America, vol. 85, no. 6, pp. 2290–2300, Jun. 1989, publisher: Acoustical Society of America. [Online]. Available: https://asa.scitation.org/doi/10.1121/1.397775

[153] W. Fu, Z. Shen, Y. Xu, C.-L. Zou, R. Cheng, X. Han, and H. X. Tang, "Phononic integrated circuitry and spin–orbit interaction of phonons," Nature Communications, vol. 10, no. 1, p. 2743, Jun. 2019, number: 1 Publisher: Nature Publishing Group. [Online]. Available: https://www.nature.com/articles/s41467-019-10852-3

[154] N. Nakamura, H. Ogi, and M. Hirao, "Resonance ultrasound spectroscopy with laser-Doppler interferometry for studying elastic properties of thin films," Ultrasonics, vol. 42, no. 1-9, pp. 491–494, Apr. 2004.

[155] M.-H. Chou, E. Dumur, Y. P. Zhong, G. A. Peairs, A. Bienfait, H.-S. Chang, C. R. Conner, J. Grebel, R. G. Povey, K. J. Satzinger, and A. N. Cleland, "Measurements of a quantum bulk acoustic resonator using a superconducting qubit," Applied Physics Letters, vol. 117, no. 25, p. 254001, Dec. 2020, publisher: American Institute of Physics. [Online]. Available: https://aip.scitation.org/doi/full/10.1063/5.0023827